Non-structural applications of Ioncell® carbon fibers

Isaac Yair Miranda Valdez

School of Chemical Engineering

Master's Programme in Chemical, Biochemical and Materials Engineering
Major in Fiber and Polymer Engineering

Master's thesis submitted for examination for the degree of
Master of Science in Technology
Espoo, 25 April 2022

Supervisor Prof. Michael Hummel

Advisor Dr. Chamseddine Guizani

Aalto University
School of Chemical
Engineering

Aalto University
School of Chemical
Engineering

Aalto University, P.O. BOX 11000, 00076 AALTO
www.aalto.fi

Abstract of master's thesis

Author	Isaac Yair Miranda Valdez
Title of thesis	Non-structural applications of Ioncell® carbon fibers
Degree Programme	Chemical, Biochemical and Materials Engineering
Major	Fiber and Polymer Engineering
Code of major	CHEM 3024
Thesis supervisor	Prof. Michael Hummel
Thesis advisor(s)	Dr. Chamseddine Guizani
Date	25.03.2022
Number of pages	ix + 56 + XXII
Language	English

Abstract

Engineering cellulose-based materials has received much attention to relieve the burden of CO_2 emissions and dependence on non-renewable resources. In particular, as this thesis demonstrates, cellulose pyrolysis represents a potential route to fabricate carbon fibers (CF), which can alleviate the global demand for natural graphite and synthetic carbons. Nevertheless, understanding cellulose thermal decomposition presents many knowledge gaps; filling them is necessary to tailor CF that display specific nanostructures, functionalities, and textures. The work hereafter examined the carbonization yield ($\hat{y}_1$) of Ioncell® cellulose fibers. $\hat{y}_1$ is a constraint hindering the scalability of cellulose as a CF precursor. This thesis displays how experimental design can assist in modeling the influence of diammonium hydrogen phosphate (DAP), CO_2 activation time, and lignin (BL) on cellulose $\hat{y}_1$. DAP and BL are factors known for increasing $\hat{y}_1$ as they inhibit forming small volatile carbon compounds during cellulose pyrolysis. However, this study showed that, when combined, the effect of DAP and BL on $\hat{y}_1$ are non-additive. Assessing the performance of Ioncell CF in non-structural applications consisted of enhancing their texture and surface chemistry. This thesis bridged gaps in carbon materials science during the CF characterization. For example, the manuscript adapts and verifies tools and methods developed by third-parties to ease the mathematical treatment of adsorption isotherms and Raman spectra. All in all, Ioncell CF had relatively high CO_2 adsorptions (~2 mmol/g) at unsaturated pressure conditions. These biobased CF were microporous materials, and they may be crucial in gas separation membranes and storage systems.

Keywords activated carbon fiber, cellulose, lignin, carbon dioxide adsorption

Preface

This thesis presents an original research work carried out from September 2021 to March 2022 in the Aalto University's Department of Bioproducts and Biosystems. I acknowledge my supervisor, Prof. Michael Hummel, and advisor, Dr. Chamseddine Guizani, for their valuable guidance, trust, and support. I want to thank the School of Chemical Engineering and Aalto University for awarding me a tuition-fee scholarship, allowing me to continue my graduate studies in the middle of a worldwide sanitary contingency.

I express my gratitude to the Government of Mexico and Nuevo Leon for funding my graduate studies through its scientific institutions: Consejo Nacional de Ciencia y Tecnología (CONACYT) and Instituto de Innovación y Transferencia de Tecnlogía. I am thankful to all the people who supported me during my studies. Special thanks to my family and partner, as well as my former academic fellows. They all contributed to my personal and professional formation.

Espoo, Finland, April 25, 2022
Isaac Yair Miranda Valdez

Contents

Symbols and abbreviations

Symbols

a_s	BET specific surface area
b_i	linear coefficient in the response regression equation
b_{ii}	quadratic coefficient in the response regression equation
b_{ij}	interaction coefficient in the response regression equation
b_0	intercept of the response regression equation
C	adsorption constant in the Freundlich's model
E	elastic modulus
E_L	laser energy
I	Raman intensity
k	factors in experimental design
k_c	pathway 2 of cellulose pyrolysis (carbon)
k_v	pathway 1 of cellulose pyrolysis (volatiles)
L_a	average crystallite diameter in the basal plane
M_w	molecular weight
N	sampling points in experimental design
n	center point in experimental design
p	pressure
p/p_0	relative pressure
q	coupling factor in the Breit-Wigner-Fano function
r	exponential constant in Freundlich's model
R^2	coefficient of determination
V_μ	volume of microporosity
$wt.\%$	weight percentage
x_1	factor assigned to DAP impregnation
x_2	factor assigned to CO_2 activation

x_3	factor assigned to lignin content in the Ioncell fiber
$\hat{y}$	response in experimental design
$\hat{y}_1$	carbon fiber yield
a	exponential factor in the Ferrari's and Robertson's law
Γ_{D1}	width of D1 sub-band
Γ_{D2}	width of D2 sub-band
Γ_G	width of G sub-band
ΔH	enthalpy of change
ε	experimental error of the response surface regression
λ	wavelength of light
σ_u	tensile strength
X	adsorbed load in the Freundlich's model
ω	spectral wavenumber
ω_D	D band phonon
ω_G	G band phonon

Abbreviations

AC	activated carbons
ACF	activated carbon fibers
AS	adaptive sampling
BET	Brunauer-Emmett-Teller
BL	beech lignin
BWF	Breit-Wigner-Fano
CCD	Central Composite Design
CF	carbon fiber
CO	carbon monoxide
CO_2	carbon dioxide
DAP	Diammonium hydrogen phosphate

[DBNH][OAc]	1,5-diazabicyclo[4.3.0]non-5-enium acetate
DoE	Design of Experiments
E100	Ioncell fiber made of cellulose
E70	Ioncell fiber made of 70% cellulose and 30% lignin
E50	Ioncell fiber made of 50% cellulose and 50% lignin
EDS	Energy-dispersive spectroscopy
ESS	Energy Storage Systems
FCCD	Face-centered Central Composite Design
FE-SEM	Field Emission Scanning Electron Microscopy
FWHM	Full width at half maximum
GHG	greenhouse gases
H_2O	water
He	helium
ICP-MS	Inductive Coupled Plasma Mass Spectroscopy
IL	ionic liquid
MCF	man-made cellulose fibers
N_2	Nitrogen
NMMO	*N*-methylmorpholine *N*-oxide monohydrate
PAN	polyacrylonitrile
RSM	Response Sruface Methodology
SEC	Size Exclusion Chromatography
SEM	Scanning Electron Microscopy
SFD	Sample Filling Design
SO_2	sulfur dioxide
TFD	Two-level Factorial Design
XPS	X-ray Photoelectron Spectroscopy

1 Introduction

Over the last few years, adopting a bioeconomy has revolutionized the attitude toward forest management and shifted cellulose into a vital resource [1-5]. As evidence of this trend in Europe, between 2016 and 2018, Ceccherini *et al.* [4] recounted a 69% growth in the consumption of lignocellulosic biomass compared to preceding years. Favored by the current European single-use plastic policy [6], nowadays, cellulose represents a potential precursor to fabricate foams [7-9], textiles [10-12], packaging [13-15], and electronics [16-18]. More importantly for this thesis, cellulose provides an alternative to satisfy the demand for natural graphite, a critical raw material declared by the European Commission [19]. In this context, and due to the non-renewable origin of fossil fuels and graphite, numerous investigations have revisited cellulose as a precursor to manufacture carbon materials [20-22]. Remarkably, much effort has been made to exploit the thermal decomposition of man-made cellulose fibers (MCF), such as viscose, Lyocell, and Ioncell®, to fabricate carbon fibers (CF) for non-structural applications, such as carbon dioxide (CO_2) capture [21, 23-25].

Typically, CF production follows the carbonization of polyacrylonitrile (PAN), a synthetic copolymer accounting for 90% of the precursors used in CF manufacture [26]. However, several authors have highlighted the necessity for replacing PAN with a sustainable and economical alternative [22, 27, 28]. Therefore, MCF have attracted the attention of many researchers since these organic precursors denote an option to assemble continuous CF production lines (i.e., from dope spinning to carbonization) [23, 24, 27, 29, 30]. Figure 1 illustrates a cellulose-based CF produced from Ioncell fibers as an example of this possibility. Unfortunately, the scalability of cellulose as a precursor of CF is hindered by its low carbonization yield [31]. Theoretically, water should be the only gaseous product during cellulose pyrolysis, resulting in a carbonization yield of 44.4% (i.e., the carbon content in a repeating unit) [28, 32]. Nonetheless, the pyrolysis leads to other volatile side gases (e.g., CO_2 and CO), which prevents reaching the ideal carbonization yield in practice [28, 32-35]. For example, typical yields from cellulose are closer to 10% [35], a number drastically lower than the one derived from PAN (ca. 59%) [36, 37].

Two promising methods to increase the carbonization yield of cellulose involve using dehydration catalysts and lignin. Chapter 2 discusses these two approaches in detail, but in brief, the methods are known for acting against the CF mechanical performance. In the first instance, dehydration catalysts, such as diammonium hydrogen phosphate (DAP), form microporosity in the

CF [22]. Alternatively, lignin decreases the long-range order of the cellulose crystals and increases the number of non-graphitizable segments in the precursor fibers [38]. Within this framework, a standard procedure to capitalize on the improved carbonization yield and CF structural defects entail activating the carbon material. Through developing microporosity, ultramicroporosity, and functional sites, biobased activated carbon fibers (ACF) have shown attractive properties in energy storage systems (ESS) and gas adsorption [21, 22, 39]. For example, Breitenbach *et al.* [22] have recently prepared an electrode based on ACF (CO_2 activation) made from impregnated viscose fibers. The electric component displayed a specific capacitance of 139 F g^{-1}.

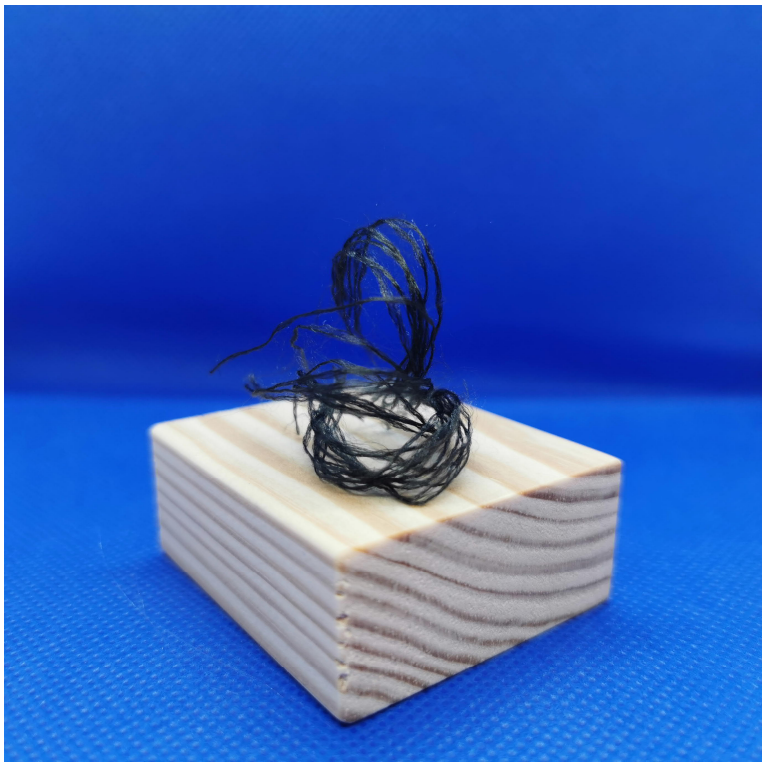

Figure 1 Ioncell® carbon fibers produced after the pyrolysis of cellulose-based fibers. Carbonization occurred by heating from room temperature to 800°C inside a tube furnace Nabertherm RHTH 80-300/16 purged with N_2 gas.

Overall, it is challenging to produce CF from MCF. Cellulose precursors present low yields and structural heterogeneities when assessing their production, applications, and scalability. Nevertheless, in the words of Mitrano and Wohlleben [40], "*Policymakers … stimulate innovation of new, more competitive and environmentally conscious materials*". Thus, day after day, disclosing limitations on the plastic industry encourages taking advantage of biobased resources. For this thesis, the former statement translates into improv-

ing the carbonization yield of cellulose in such a manner that the biopolymer turns into a feasible option as a CF precursor. In fact, concerning Mitrano's and Wohlleben's [40] statement, projects such as Ioncell cellulose fibers have emerged, owning as a common focus area to reduce the consumption of fossil-based products [41]. Ioncell fibers, which this work uses as CF precursors, are MCF, and their green fabrication technology portrays themselves as a sustainable and proven option to fabricate CF [29], as Figure 1 has exemplified.

This thesis aims to increase and model the carbonization yield of Ioncell fibers under the effects of DAP, CO_2 activation, and lignin. Simultaneously, the goal of this study is to assess the properties of Ioncell CF for their use in CO_2 adsorption. Carbon dioxide is one of the most abundant heat-trapping greenhouse gases (GHG) [42]. In recent years, the CO_2 level in the atmosphere has harshly risen due to the global demand for energy and massive production practices [43, 44]. This concentration of CO_2 symbolizes a threat to the equilibria of biogeochemical cycles in the biosphere. Therefore, carbon materials have been suggested as a keen solution to mitigate the emissions of CO_2 as they can act as membranes to capture and store the gas [23, 43, 45]. Furthermore, since cellulose is the most abundant and renewable high polymer in nature, synthesizing CF using cellulose is a common direction for multiple researchers [23, 27, 31]. Accordingly, this thesis identifies crucial to investigate the methods to increase the carbonization yield of cellulose and their impact on the CF properties and performance in CO_2 adsorption.

In brief, this thesis evaluates CO_2 adsorption as a non-structural application of Ioncell CF. This research plans to take advantage of the disordered carbon structures formed in the CF [46]. In synergy with CO_2 activation processes, this study hypothesizes that the CF disordered and activated structure can effectively adsorb CO_2, as reported for other carbon materials [47]. Additionally, this work uses a Design of Experiment (DoE) approach to evaluate and model the influence of lignin and a dehydration catalyst on the carbonization yield obtained from Ioncell fibers. The reported investigation enriched the discussion and understanding of the CF properties by employing textural characterization, Raman spectroscopy, Scanning Electron Microscopy (SEM), and other methods. This manuscript outlines four more chapters. First, Chapter 2 reviews contemporary research in cellulose pyrolysis. Chapter 3 describes the materials and methods, and Chapter 4 presents and discusses the experimental and computational results. Finally, Chapter 5 concludes by pointing to suggestions and the foreseen relevance of this thesis.

2 Literature review

In order to model the effects of diammonium hydrogen phosphate, CO_2 activation, and lignin on the CF yield, the following chapter reviews the advances in four topics related to the work herein reported. First, Section 2.1 describes the Ioncell technology and explains its potential as a carbon fiber precursor. Second, Section 2.2 details the pyrolytic mechanism of cellulose, typical carbonization procedures, and challenges to overcome during and after carbonization. Next, Section 2.3 features the physical activation of carbons as a strategy for tailoring carbon fiber nanostructure and surface chemistry. Finally, Section 2.4 presents the theory behind the optimization model employed to assess the property-performance interactions.

2.1 Ioncell® fibers

Ioncell is a research project developed at Aalto University (Finland), focusing on sustainably transforming lignocellulosic materials into high-quality MCF for textiles [48]. Ioncell products range from cellulose to cellulose-lignin blends fabricated from primary and secondary resources [41, 49]. Figure 2 unveils some of the Ioncell fibers, which their color stems from mixing different quantities of cellulose and lignin [50]. Manufacturing these fibers employs a novel technology involving the direct dissolution of raw materials in 1,5-diazabicyclo[4.3.0]non-5-enium acetate ([DBNH][OAc]). Polymer dissolution in this ionic liquid (IL) allows spinning round and highly oriented MCF, as illustrated in Figure 3 [51]. Thus, Ioncell fibers, compared with other MCF, exhibit higher E and tensile strength (σ_u), as presented in Table 1.

Figure 2 Ioncell® fibers are made of cellulose and cellulose-lignin blends. At a glance, fibers dyed with a darker color contain lignin in different amounts. In this illustration, each Ioncell product is laid in an aluminum tray.

In numerous publications, Sixta *et al.* [50-52] have assessed the Ioncell fibers features against the most common MCF, viscose and Tencel. Regarding the fabrication process, Ioncell technology excludes derivatizing cellulose into an intermediate substance, as it occurs with cellulose xanthate during viscose manufacturing [52]. The former derivatization step yields several toxic compounds as by-products, owning, thus, environmental drawbacks [53]. Contrary to the viscose process, the Ioncell pathway follows the same dry-jet wet-spinning methodology utilized in Lyocell fibers production [54]. Nevertheless, the distinction between other Lyocell products, such as Tencel, banks on the solvent. Tencel solvent, *N*-methylmorpholine *N*-oxide monohydrate (NMMO), demands stabilizers since it may undergo exothermic reactions at the spinning temperature [41]. Alternatively, Ioncell solvent, [DBNH][OAc], omits extra chemical reagents and allows dissolving low-purity raw materials, including lignin [41]. Lignin dissolution via Ioncell technology is vital for this thesis because it permits MCF to increase their carbonization yield [36]. The undermentioned sections discuss the reasons.

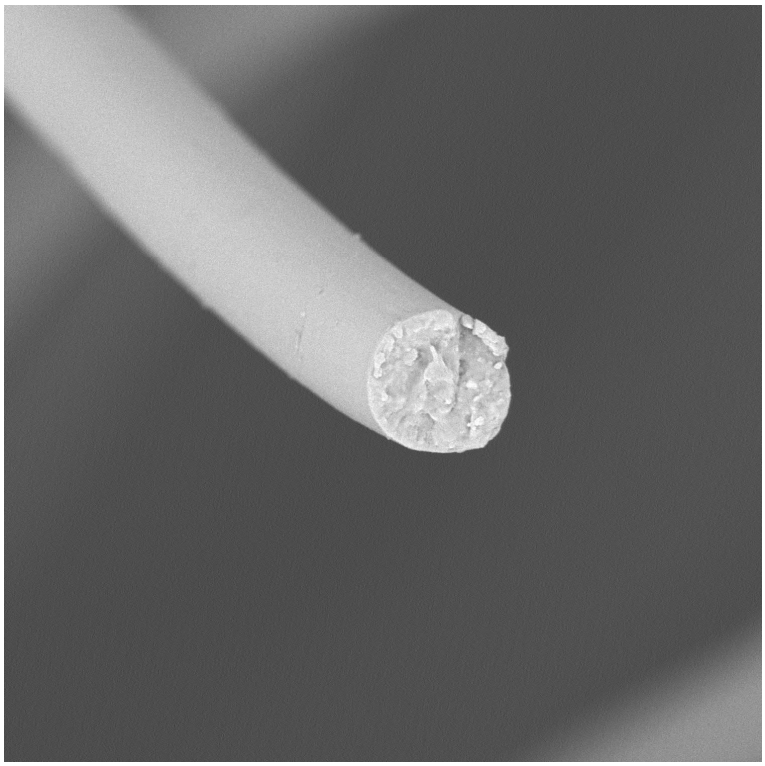

Figure 3 Scanning electron microphotograph of Ioncell® fiber (cellulose/lignin blend) showing its round cross-section (~15 µm). The picture was taken using a Phenom Pure Tabletop SEM at 2500x and 5 keV.

The use of Ioncell as a carbon fiber precursor comes as a trial to resolving the global necessity of lowering GHG emissions and energy consumption. Despite the fact that the main application of Ioncell fibers aims to fabricate sustainable fabrics, Byrne *et al.* [29] sustained for the first time their plausible employment to produce CF. Since then, works, including the ones of Trogen *et al.* [31] and Le *et al.* [38], have also permitted the production of CF from Ioncell fibers made up of cellulose/lignin blends. The attractiveness of Ioncell technology to manufacture CF counts on creating a continuous production line, encompassing the carbonization or pyrolysis of cellulose, a phenomenon described in depth in Section 2.2.

Table 1 Mechanical properties of manufactured cellulose fibers. The numerical figures presented for tensile strength and elastic modulus are approximations to the results reported by Ma *et al.* [41]

Manufactured cellulose fiber	Tensile strength (σ_u) in MPa	Elastic modulus (E) in GPa
Viscose	350	11
Tencel	550	23
Ioncell®	700	26

2.2 Carbonization of manufactured cellulose fibers

MCF encircles the regenerated and coagulated celluloses turned into raw materials for the textile industry, including viscose, Tencel, and Ioncell. The principal constituent of these fibers is cellulose, the most abundant naturally occurring polymer on Earth. Cellulose is a homopolymer primarily found in the cell walls of trees. Explicitly, the polymer chain of cellulose constitutes an "n" number of D-glucopyranoses held together by ß-(1→4) glycosidic bonds [16]. Due to the renewable nature of MCF and their continuous production capacity, several researchers suggest them as the most suitable candidates to replace synthetic fibers in CF manufacturing at an industrial level [29, 31]. In the aforesaid case, the production of CF from MCF proceeds according to the pyrolysis of cellulose, which is thought to occur through the two-step global reaction mechanism shown in Figure 4 [33].

In 1964, Tang and Bacon [34, 55] postulated that the pyrolysis reaction of cellulose (Figure 4) starts through the physical desorption of water molecules (from 25 to 150°C). Subsequently, after increasing the temperature to 240°C, cellulose moieties undergo an intramolecular dehydration process, generating the so-called "active cellulose" [56, 57]. From 240 to 400°C, according to Figure 4, Bradbury *et al.* [56] explained that cellulose pyrolysis proceeds throughout two competitive first-order reactions. Both reaction pathways adhere to the depolymerization of cellulose, which commences by the chain scission of the intermolecular glycosidic bonds. Pathway 1 (k_v) comprises the cleavage of intramolecular ether (C–O) and alkane (C–C) bonds [34]. Above 400°C, pathway 1 finalizes, producing more tar (levoglucosan) and permanent gases [33]. However, some authors suggest that pathway 1 produces a secondary char [57]. Therefore, pathway 1 in its entirety is undesirable for the production of CF because it deviates the reaction from obtaining the desired char product.

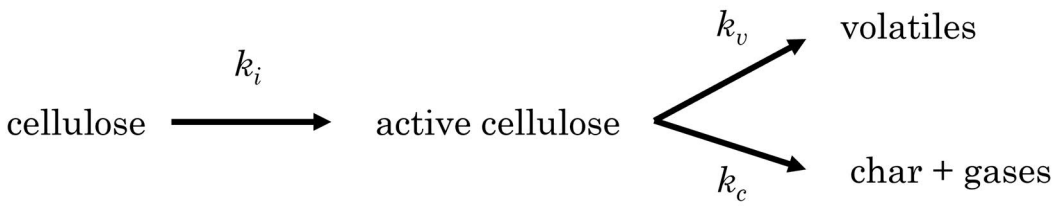

Figure 4 Pyrolysis pathways of cellulose proposed by Bradbury *et al.* [56]

On the other hand, pathway 2 (k_c) involves rearranging cellulose chains after dehydration [33]. As an outcome, carbonyl and alkene group bonds form inside the moieties, resulting in a carbon intermediate [33, 34, 57]. In addition, the development of the residual char produces CO, CO_2, and H_2O gases [33, 34]. Then, above 400°C, this pathway continues with the aromatization of the carbon intermediate, which results, depending on the maximum carbonization temperature, in combinations of the carbon structures depicted in Figure 5 [58]. Thus, according to pathway 2, a cellulose CF precursor should produce a theoretical char yield of 44.4%; though, pathway 1 illustrates the reason for a smaller yield obtained in practice, representing a challenge to escalate the use of MCF in CF manufacture [33].

Theoretically, during the pyrolysis of cellulose, water should be the only gaseous product while the carbon structure is developing [59]. However, as mentioned above, this process deviates from the theory since it leads to other volatile side gases in practice. Scholz *et al.* [59] summarized three key points to achieve the ideal reaction yield from MCF pyrolytic process, all of them em-

phasizing the dehydration reactions. The first point recalls the investigation of Brunner and Roberts [32]. Their work showed that cellulose dehydration governs the pyrolytic decomposition of the polysaccharide at low temperatures [32]. Nowadays, it is well-known that promoting cellulose dehydration via thermal stabilization (i.e., slow heating rate) avoids side reactions, including depolymerization. Works such as the one published by Zolkin *et al.* [60] exemplify that thermal stabilization of MCF (dehydration at 0.5°C/min) derives in carbon yields up to 38%. This number is very close to the theoretical yield of 44.4%, and it doubles the char yield reported by other authors, for instance, Breitenbach *et al.* [22] (dehydration at 1°C/min).

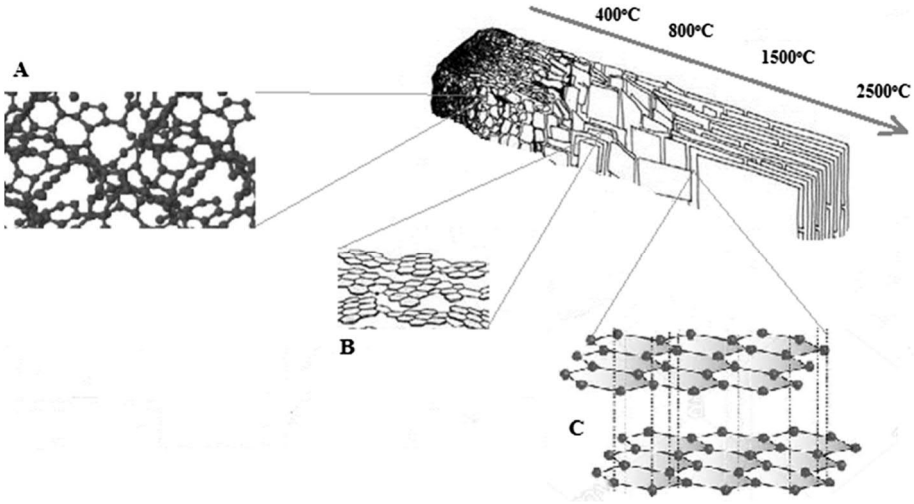

Figure 5 Illustration of the effect of the pyrolysis temperature on the structure of biochars such as cellulose-based CF. a) At temperatures close to 400°C, the carbon shows a disordered structure. The order of the carbon structure increases as a function of the pyrolysis temperature. For instance, at 800°C, (b) illustrates a defective stacking of aromatic layers (turbostratic carbon, while (c) at 1500°C, the material has a long-range arrangement. [58]

The second aspect pointing Scholz *et al.* [59] features dehydration catalysts to maximize the carbonization yield of MCF. Dehydration catalysts enclose a group of Brønsted and Lewis acids composed of heteroatoms (i.e., nitrogen, phosphorus, sulfur, oxygen, or chlorine) [59]. A catalyst of such nature drops the dehydration temperature of cellulose and prevents its spontaneous ignition [35, 61]. In other words, the catalyst prioritizes the demerging of water molecules over removing small volatile carbon-containing compounds (CO_2, CO, tar, and methane) [35, 59]. In addition to the catalytic effect at low temperatures, heteroatoms contained in a catalyst create covalent bonds with the intermediate pyrolysis carbohydrates [59]. This covalent bonding hinders the

cleavage of the carbon chains. Multiple authors have explored the effect of dehydration catalysts on MCF, and they have reported increasing their carbonization yield by around 15% [22, 35, 39, 62, 63]. Adding a catalyst to MCF involves immersing the fibers into an impregnating solution for times reported from 15 minutes [22] to 5 hours [39] prior to the carbonization process.

A third method to enhance the carbonization yield from MCF considers the addition of carbon black [59]. Nonetheless, thanks to Ioncell technology, blending MCF with lignin has instead become an attention-grabbing mechanism [31, 38]. The idea of using lignin-polymer blends as CF precursors is not new; Oroumei *et al.* [36] described for the first time the potential of lignin to increase the yield of PAN-based CF. According to Oroumei *et al.* [36], organosolv lignin (sulfur-free) increases the carbonization yield thanks to the high cleavage temperature (> 300°C) of its α-ether linkages. On the other hand, in Ioncell fibers based on cellulose and lignin, the pyrolysis behavior of the latter could represent a shift of the major degradation in the fibers toward higher temperatures while also reducing the dehydration temperature [27]. Concerning the former case, Trogen *et al.* [31] stated that adding lignin to Ioncell fibers increases their carbonization yield due to the melt-phase radical pyrolysis and devolatilization processes of lignin, which include a sort of initiation, propagation, and termination reactions competing against each other [31]. The condensation and recombination reactions lead to an increased yield after lignin pyrolysis. The present work evaluates the carbonization process and the effects of a catalyst and lignin on Ioncell fibers.

2.3 Physical activation of cellulose-based carbon fibers

Physical activation describes a method to tailor CF surface attributes, such as nanostructure, functionality, and texture [46]. In this context, activation requires applying an activating agent (e.g., CO_2) to the residual char and exposing it to a high temperature (e.g., from 700 to 1000°C) for a specific time; the result is a material named adequately as activated carbon (AC). The activation protocol usually starts right after MCF carbonization. For example, in Figure 6, Karacan and Soy [33] categorized the activation as the immediate step after the carbonization of viscose fibers. Several authors prefer the activation sequence in Figure 6, as it is suitable for continuous processing at an industrial level [22, 30, 33, 63-65].

Okolie *et al.* [66] remarked biobased-AC as a promising functional materials to mitigate water pollution and energy consumption [22, 67]. This presumption considers AC as materials displaying different surface properties

depending on the oxidizing agent, activation time, and temperature. During the activation reaction, the volatile matter contained in the carbon leaves the matrix, affecting the carbon morphology and surface chemistry. For example, the number of pores and pore size increases, creating a microporosity (< 2 nm), mesoporosity (from 2 to 50 nm), and macroporosity (> 50 nm) distribution [46, 66]. Likewise, the activated carbon may present different fractions of aromatic and aliphatic carbons, carbonyl groups, carbonate, and oxygen [68]. In principle, the physical activation reaction is a heterogeneous diffusion reaction phenomenon materialized at the solid/gas interface between the carbon-accessible surface and the oxidizing agent [64]. When the reaction occurs in a carbon dioxide atmosphere like herein reported, the activation reaction is best described by the Boudouard reaction Eq. 1 [69].

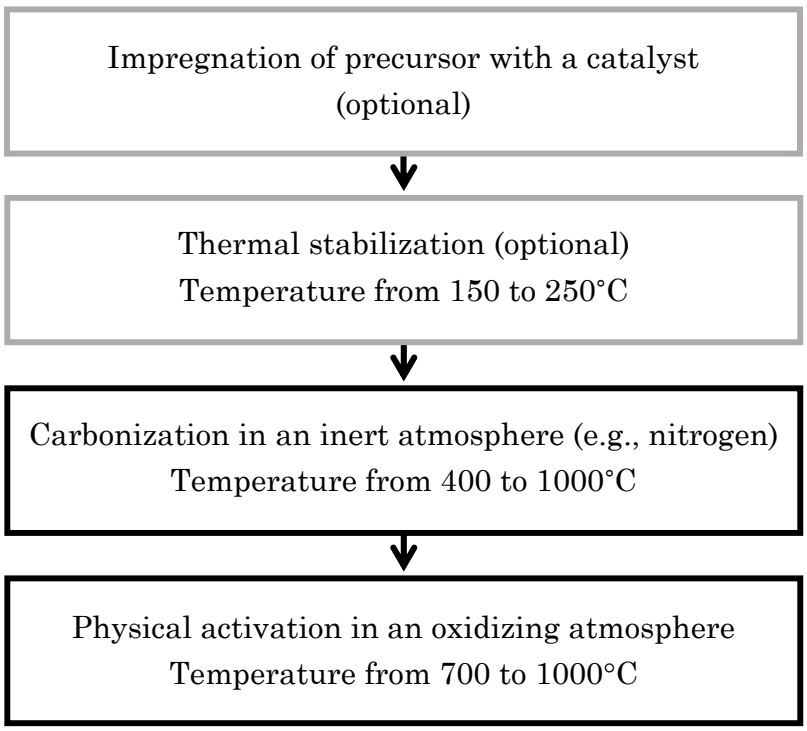

Figure 6 Flowchart of a typical process to manufacture viscose-based CF proposed by Karacan and Soy [33]. This diagram considers the impregnation of a dehydration catalyst. Additionally, the authors apply a stabilization step, following a slow heating rate in the temperature interval from 150 to 250°C.

$$C(s) + CO_2(g) \rightleftharpoons 2CO(g) \qquad \Delta H = 172\ kJ/mol \qquad \text{Eq. 1}$$

On the left side of Eq. 1, the activation of carbon implies a reaction of the solid carbon with CO_2 to form CO [70]. However, this direction of the Boudouard reaction is only favored at temperatures above 700°C [69-71]. Whilst on the other reaction side, the phenomenon describes the auto-oxidation of CO to CO_2. The Boudouard reaction represents a proven method to add functional groups in AC and modify their structure; still, the reaction stability only at high temperatures denotes its main drawback since it represents a high energetic cost [71]. Figure 7 shows a simple way to visualize the activation effects on a carbon material when the activation agent is CO_2. This illustration considers that the thermodynamic conditions favor the Boudouard reaction toward producing carbon monoxide.

A number of publications have reported using the Boudouard reaction to activate cellulose-based CF [22, 30, 64, 72-75]. Activated carbon fibers are preferred over the typical granulated AC, as ACF hold a regular diameter. In particular, this characteristic grabs the attention of scientists evaluating materials for electric applications; ACF have a low electrical resistance along the longitudinal axis and a high specific capacitance (higher than 100 F g^{-1} in many cases) [20, 22, 72, 76-78]. The last characteristic stems from the activation process, thereby increasing the porosity in the solid carbon and allowing more electric charge carriers in the electric double layer [79]. Cellulose-based ACF have also performed successfully in adsorbing molecules such as CO_2 [25, 47, 80-83], SO_2 [39, 84], toluene [21], and benzene [21]. Similar to the reasoning behind ACF electric properties, the ability to gather volatile molecules on the carbon surface appears after enhancing the porosity and surface chemistry of the material [21].

Evaluating the properties-performance relationship of ACF in such cases mentioned above represents a challenge. In order to overcome this situation, many research articles commonly correlate the surface area of AC with their porous structure and stimuli responses [21, 47, 76, 85]. For instance, Ismail *et al.* [47] reported from their study that ACF owning the highest surface area had the best efficacy in CO_2 adsorption. Correspondingly, Choi *et al.* [21] demonstrated a direct proportionality between the capacity to adsorb toluene and the surface area of ACF. Nonetheless, using this textural property to characterize porous carbons is a controversial topic since its calculation assumes that an atomic surface mirrors the macroscale; in the opinion of Marsh and Rodríguez-Reinoso [46], "*this assumption has led to much non-productive debate*". Similarly, Shi [79] remarked that in AC, the surface area concept conflicts, for example, with the Brunauer-Emmett-Teller (BET) theory [86], due to the different capacities of micropores and macropores to adsorb molecules. This thesis considers the former drawbacks of estimating the surface area and

evaluates its impact on the performance assessment of ACF. For this thesis, the BET surface area (a_s) is a quantity that can be extracted from nitrogen adsorption isotherms. However, due to its controversial meaning of the actual surface area of microporous carbons, this study relies on evaluating other properties, such as pore volumes.

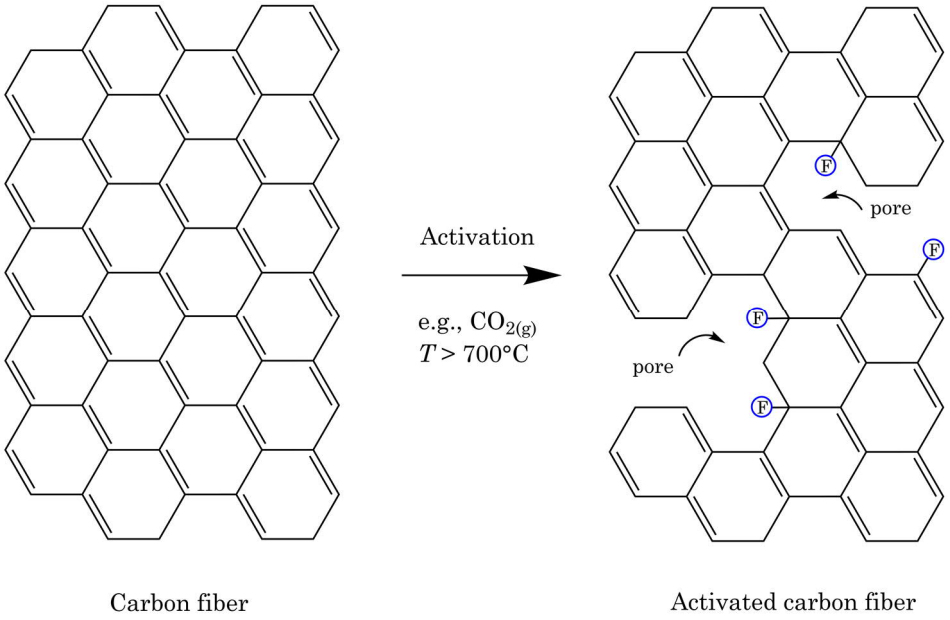

Figure 7 Simplified representation of the activation phenomenon. The picture depicts a graphitic structure developing porosity after reacting with CO_2 at high temperatures. Furthermore, the encircled letters F's indicate possible functional groups grafted to the matrix after the activation protocol (e.g., carbonyl groups). This illustration is an adaptation of the activation mechanism proposed by Choi *et al.* [21]

2.4 Design of experiments applied to carbon fibers

Statistical experimental design, often known as the design of experiments, is an integral chemometric tool used to study cause-effect and phenomena-response relationships in a process while varying all the analyzed factors [87]. The concept of DoE was first popularized by Fisher [88], who proposed it as a strategy to build interpretations that could refute critics made by statisticians and "heavyweight authorities". In experimental sciences, any system can have multiple factors influencing its responses. For example, recalling the factors discussed in Section 2.2 about cellulose pyrolysis, the carbonization yield (response) depends on inputs (factors), such as carbonization temperature, catalyst, lignin content, heating rate, and the activating agent [28, 30, 31, 38, 59,

74]. Therefore, in order to accomplish the thesis aim, DoE represents a statistical approach to sample, analyze, and represent a series of carbonization experiments.

An essential step in DoE is choosing the sampling points. Greenhill *et al.* [89] reviewed four of the most used sampling methods in experimental design: (a) Two-level Factorial Design (TFD), (b) Central Composite Design (CCD), (c) Space Filling Design (SFD), and (d) Adaptive Sampling or Active Learning (AS). The first one, TFD, implicates an experimental design varying the factors at their minima and maxima, interpreting their effect on the chosen response through a linear model [89, 90]. CCD describes a system by evaluating the factors at low, medium, and high levels, allowing quadratic terms in the interpretation model [89, 90]. Like CCD, SFD evaluates the factors at different levels but distributes them evenly with equal probability [89]. In contrast with the former three designs, AS is a sequential and probabilistic process requiring the input of sampling points to predict the next one. AS utilizes Machine Learning tools (e.g., Bayesian Optimization with a Gaussian regressor) to formulate non-parametric models [89, 91, 92]. Figure 8 aims to highlight the difference between each of the aforementioned sampling methods.

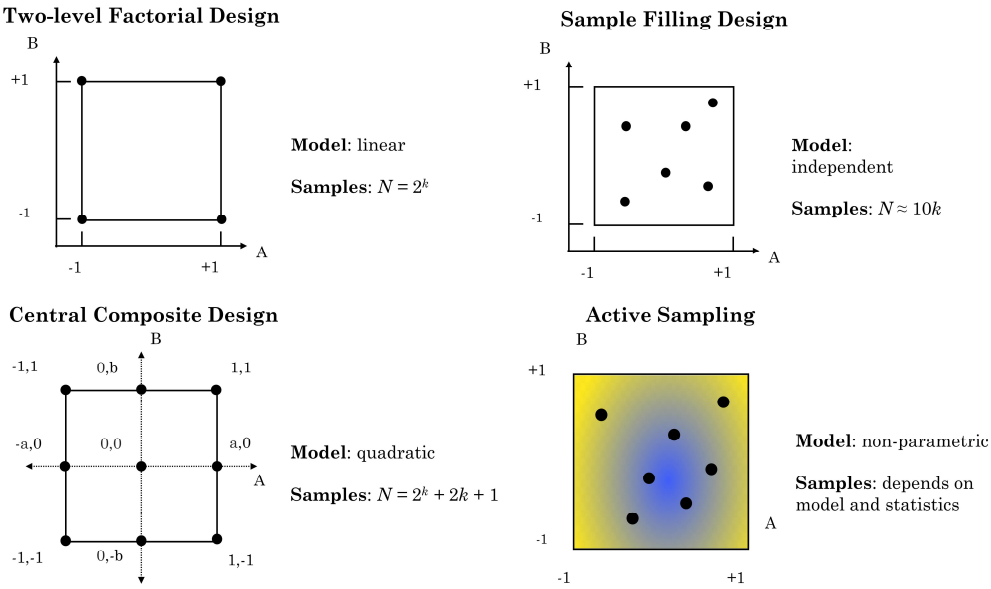

Figure 8 Sampling methods used in experimental design. The representation of each sampling method depicts an experimental matrix for evaluating a systems response as a function of two factors. This figure is an adaptation based on Greenhill *et al.* [89], and k represents the number of factors.

Concerning this thesis, CCD represents a versatile approach for analyzing the effect of carbonization factors on the system responses. This experimental method optimizes a specific response by following the Response Surface Methodology (RSM) [90, 93-97]. For example, recently, Breitenbach *et al.* [96] utilized the CCD method to maximize the carbonization yield and surface area of viscose-based CF. Although their article described an experimental sequence based on a square matrix (i.e., two factors), extending the matrix size to a third factor is also possible. The CCD matrix depicts a three-dimensional array in a three-factor design, as Figure 9 shows [93].

CCD has different modifications, including the Face-centered Central Composite Design (FCCD), to reduce the number of experiments while exploring the response surface [98]. Figure 9 illustrates the FCCD method, composed of eight factorial sampling points, six points at the center of the cube faces, and a central point. Eslami-Farsani [95] proved the suitability of using FCCD to optimize the mechanical performance of CF after varying the carbonization time and temperature. However, to the knowledge of the author, no work has attempted to build knowledge of the ACF responses by employing a three-factor FCCD. A model including three factors may enhance a better understanding of the synergistic effect of the factors on, for instance, the CF performance and carbonization yield.

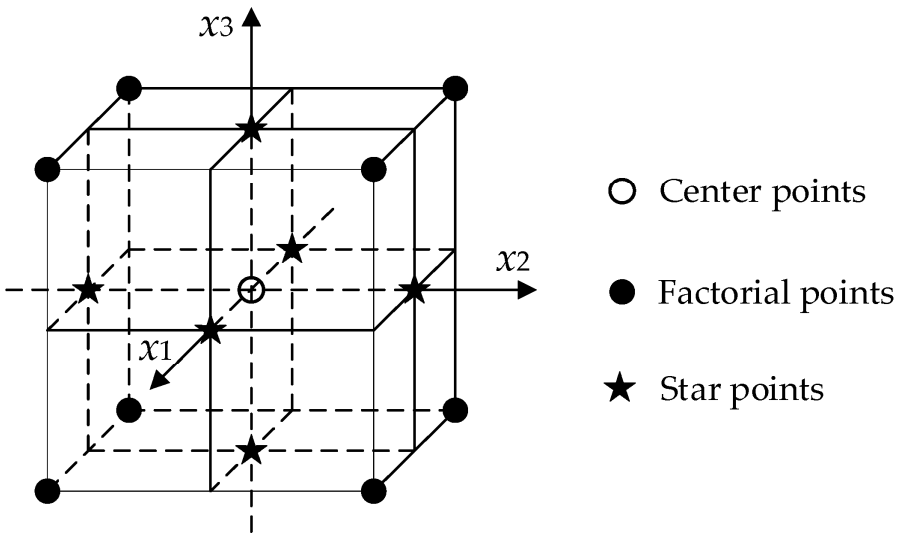

Figure 9 Three-dimensional matrix of the Face-centered Central Composite Design. The array highlights the sampling points required to follow the Response Surface Methodology. [93]

3 Research materials and methods

This chapter presents a detailed description of the materials and methods employed in this thesis. First, Section 3.1 covers the information related to the raw materials, while Section 3.2 outlines the experimental design. Then, Section 3.3 describes the carbonization and activation process of Ioncell fibers. From Section 3.5 and onward, this chapter presents the technicalities of each characterization method.

3.1 Materials

Ioncell fibers (draw ratio: 6, length ≈ 9 cm, and diameter ≈ 15 µm) were used as CF precursors for this study. Ioncell fibers contain primarily cellulose; nevertheless, the present work employed fibers based on polymer blends with different cellulose/lignin ratios. As Section 2.2 reviewed, adding lignin to a cellulose matrix should enhance the carbonization yield obtained from the organic precursor. Therefore, CF manufacturing proceeded with three types of Ioncell fibers: (a) E100, (b) E70, and (c) E50. The former names speak for the cellulose weight content (wt.%). For example, sample E70 stands for a fiber constituted by 70 wt.% cellulose, in which the remaining 30 wt.% implies the lignin content. Cellulose in the fibers is pre-hydrolyzed kraft birch pulp, and lignin is organosolv beech lignin (BL) [31]. For a detailed description of the Ioncell process, the reader is directed to articles published by Sixta *et al.* [49, 51, 52]. The regenerated cellulose composing the Ioncell fibers was analyzed via Size Exclusion Chromatography (SEC), see Appendix A. This study estimated a molecular weight (M_w) of 130 kDa and a polydispersity index of 2.7. Measuring the M_w of cellulose followed the same protocol described recently by Pitkänen and Sixta [99] but used 9.0% LiCl in DMAc instead of 0.9%. The dehydration catalyst, DAP (reagent grade ≥ 98%), was purchased from Sigma-Aldrich (India). Preparing the aqueous solution for the catalyst impregnation into the fibers used deionized water.

3.2 Experimental design

As part of the aim of this thesis, the response ($\hat{y}$), CF yield ($\hat{y}_1$), was modeled. With that intention, the experimental design considered three independent factors (k): the molar concentration of DAP in the impregnating solution (x_1), CO_2 activation time (x_2), and lignin content in the Ioncell fiber (x_3). The experimental design adhered to the space limitations fixed by a three-dimensional FCCD, which calculates the number of sampling points (N) according to Eq. 2.

The FCCD allowed analyzing the interaction between the factors and their effects on the responses at three levels (low, medium, and high). In addition, for assessing the statistical dispersion of the results, a triplicate was chosen at the center point (n). Creating and analyzing the FCCD was assisted by OriginPro® 2021b using the built-in app Design of Experiments. Table 2 collects the sampling points of the design matrix.

$$N = 2^k + 2k + n \qquad N = 17 \qquad \text{Eq. 2}$$

Table 2 Sampling points of the Face-centered Central Composite Design. Running the experiments followed the order denoted by the column "Experiment." The minimum and maximum levels of each factor and the medium level of the lignin content were manual inputs. Experiments N1 to N8 are factorial points in the design matrix, and N9 to N14 are star points. The last three experiments represent the replicates at the center point.

Experiment	Catalyst (mmol/L)	CO_2 activation (min)	Lignin (wt.%)
N1	0	0	0
N2	40	0	0
N3	0	40	0
N4	40	40	0
N5	0	0	50
N6	40	0	50
N7	0	40	50
N8	40	40	50
N9	0	20	30
N10	40	20	30
N11	20	0	30
N12	20	40	30
N13	20	20	0
N14	20	20	50
N15	20	20	30
N16	20	20	30
N17	20	20	30

Eq. 2 gives a total of 17 experiments, translating to eight factorial points, six star points, and three center points in the experimental array. Modeling a response assumed that the quadratic polynomial in Eq. 3 describes the influence of the factors on a single response [90]. In Eq. 3, b_0 is a constant value called intercept or average, b_i is the regression coefficient depending on the linear effect of the factor, b_{ii} is the factor quadratic effect, b_{ij} is the interaction coefficient between the factors, and ε is the observed experimental error. This thesis uses a matrix-based notation for the discussion. Thus, indices 1, 2, and 3 were assigned to DAP, CO_2 activation time, and lignin, respectively. For example, the coefficient b_{13} represents the interaction between DAP impregnation and lignin. Similarly, the coefficient b_{11} is the quadratic effect of DAP impregnation, and b_1 is the linear effect of the CO_2 activation time.

$$\hat{y} = b_0 + \sum_{i=1}^{k} b_i x_i + \sum_{i=1}^{k} b_{ii} x_i^2 + \sum_{i=1}^{k-1} \sum_{j=i+1}^{k} b_{ij} x_i x_j + \varepsilon \qquad \text{Eq. 3}$$

3.3 Preparation of the activated carbon fibers

First, all the precursor fibers were immersed in aqueous solutions containing the respective molar concentrations of the catalyst (Table 2). More specifically, the impregnation proceeded through dissolving DAP in water for 10 minutes under magnetic stirring at room temperature. Thereafter, in 1:200 weight ratios, 1.2 g of fibers were immersed for 2 hours in the freshly prepared DAP solutions. Then, the soaked fibers were dried overnight in a drying oven with forced convection, VENTI-Line® (VWR, Germany), to remove the excess liquid. The impregnation protocol adapted the procedures described in the literature [22, 35, 39, 62, 63, 75, 100]. Once dried, carbonization and CO_2 activation of the fibers took place in a tube furnace Nabertherm RHTH 80-300/16 (Germany). The furnace heated two samples simultaneously to 800°C (5°C/min) in an N_2 gas (flow rate: 120 L/h) atmosphere. It is worth mentioning that before every heating procedure, N_2 gas purged the furnace for 15 minutes. When having reached 800°C, the furnace was maintained at that temperature for 30 minutes, and then CO_2 gas (flow rate: 120 L/h) was injected to match the N_2 gas flow rate. CO_2 gas flow lasted for the respective activation time of each sample, and then it was reduced to zero. Subsequently, the fibers were cooled to 100°C in the same N_2 gas atmosphere. The flowchart in Figure 10 best describes the employed methodology to prepare the ACF. Finally, measuring the CF yield took into account the initial fiber mass put in the furnace and the mass recovered after heat treating them.

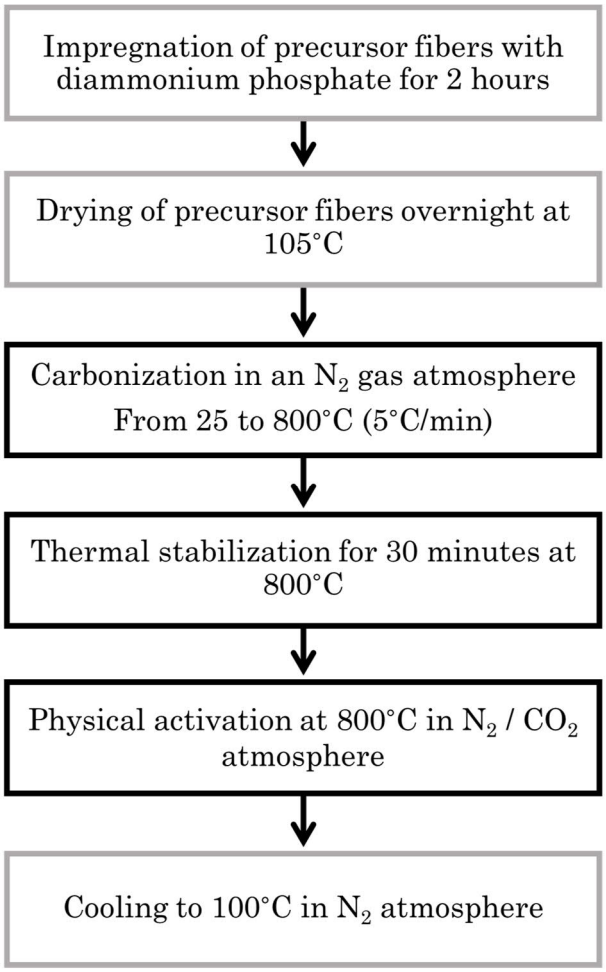

Figure 10 Flowchart of the carbonization and CO_2 activation of Ioncell fibers.

3.4 Thermogravimetry

A thermogravimetric analyzer (TGA) Netzsch STA 449 F3 Jupiter (Germany) was used to study the thermal decomposition of Ioncell fibers containing DAP and lignin. The analyses simulated the carbonization conditions in the tube furnace to assess the effect of temperature and CO_2 activation on CF yield. Therefore, the samples were heated from 40 to 800°C (5°C/min) under constant N_2 gas flow (60 ml/min). After reaching 800°C, the samples were maintained at that temperature for 30 minutes; then, CO_2 gas flow (60 ml/min) was injected to match the conditions of the protective atmosphere. The oxidizing atmosphere lasted two hours, and the TGA device recorded the mass loss during all the described thermal steps.

3.5 Textural characterization

This thesis studied the CF textural properties by measuring their N_2 physisorption capacity at -196°C. Before this characterization, around 60 mg of each sample were degassed with N_2 gas at 150°C for 12 hours. Then, creating the adsorption isotherms proceeded using a Mircomeritics TriStar II 3020 (United States) analyzer, which gradually increased the relative pressure (p/p_0) and registered the loaded adsorbate. Finally, the BET surface area (a_s) and microporosity volume of each sample were estimated using the Python™-based framework "pyGAPS" [101]. Recently, Osterrieth *et al.* [102] have pointed out the wide statistical dispersion in treating N_2 adsorption data. This dispersion results from different procedures to calculate textural properties, such as the BET surface area. For this thesis, pyGAPS offered a standardized procedure to calculate a_s and microporosity volume (V_μ) using the Rouquerol [103] and t-plot methods (non-porous carbon surface as reference), respectively.

3.6 Raman spectroscopy

Raman spectroscopy is a fast and potential method to elucidate the nanostructure of turbostratic carbon materials (combination of long- and short-range order) [104, 105]. In the case of the CF herein studied, they are expected to be highly disordered as cellulose and lignin are non-graphitizable materials [38, 106]. Furthermore, compared to X-ray diffraction, Raman spectroscopy does not require grinding up the material, a procedure that can distort the crystallinity and modify the turbostratic structure of carbons [107]. Accordingly, the CF samples were analyzed using an inVia™ Raman microscope Renishaw® Qontor (United Kingdom). The samples analysis occurred using a green laser beam (λ = 532 nm and 10% intensity) and a 20× objective within a wavenumber (ω) range from 850 to 1930 cm^{-1} (30 scans resolution). The resulting spectrum of each sample was the average of the recorded signal of three measurements at different sampling points. The background was subtracted from all the spectra using the intelligent baseline subtraction tool of WiRE™ 5.1 (first-degree function as baseline).

As proposed in the literature [106, 108, 109], this thesis analyzed the CF spectra by applying a three-peak deconvolution of the D and G bands. Two Gaussian functions at the same spectral position fitted the D band, and a Breit-Wigner-Fano (BWF) fitted the G band. The deconvolution process used the Levenberg-Marquardt algorithm in OriginPro 2021b. Fitting the Raman spectra of disordered carbons using three peaks has been reported as one of

the most accepted procedures [106, 108, 109]. The former stems from the meaningful parameters, which compose the cumulative fitting function presented in Eq. 4 [106, 108, 109]. In Eq. 4, I is the Raman intensity as a function of the wavenumber, in which ω_D and ω_G are the D and G band phonons, respectively. Γ_{D1} and Γ_{D2} are the widths of the two D sub-bands, while Γ_G represents the width of the G band. The parameter q is a coupling factor in the BWF function. Calculating the CF average crystallite diameter in the basal plane (L_a) used the I_D/I_G ratios according to Ferrari's and Robertson's law (Eq. 5) [110]. Since the D band is decomposed into two sub-bands with the same phonon, the sum $I_{D1} + I_{D2}$ provides the parameter I_D. In Eq. 5, E_L is the laser energy in eV (~2.33 eV), and α is the exponent to be calculated. For graphene, α is 4 [111].

$$I(\omega) = I_{D1}e^{\frac{(\omega-\omega_D)^2}{2\Gamma_{D1}^2}} + I_{D2}e^{\frac{(\omega-\omega_D)^2}{2\Gamma_{D2}^2}} + I_G\frac{\left(1+\frac{\omega-\omega_G}{q\Gamma_G}\right)^2}{1+\left(\frac{\omega-\omega_G}{\Gamma_G}\right)^2} \qquad \text{Eq. 4}$$

$$L_a = \sqrt{\frac{\frac{I_D}{I_G}}{0.55\times\left(\frac{2.41}{E_L}\right)^{\alpha}}} \qquad \text{Eq. 5}$$

3.7 Scanning electron microscopy

The CF surface was inspected using a Field Emission Scanning Electron Microscope (FE-SEM) Zeiss Sigma VP (Germany). Before imaging the CF, the samples were cut into small segments and sputter-coated with a gold-palladium 80/20 alloy. Then, the coated CF were mounted on carbon adhesive tape and analyzed under a high vacuum. Chapter 4 presents selected SEM images to enrich the discussion; the reader is directed to Appendix B to visualize all the SEM images. The fibers were laid horizontally on the sample holder to observe their longitudinal sections. Imaging the CF required an electric potential from 5 to 9 keV. Energy-Dispersive Spectroscopy or EDS (Ultim Max, Oxford Instruments) accompanied the analyses in a selected case.

3.8 Application of carbon fibers in CO_2 adsorption

As a non-structural application for CF, this thesis assessed their performance in CO_2 adsorption. Designing these experiments considered the methodology described by Ojwang *et al.* [112]. Thus, thermogravimetric CO_2 gas adsorption tests were chosen, and they required mounting from 13 to 15 mg of CF in a thermogravimetric analyzer STA 449 F3 Jupiter, Netzsch (Germany). The experimental sequence in the analyzer followed this order. First, the CF were degassed at 150°C for 1 hour under He gas flow (200 ml/min). Afterward, the temperature was reduced to 40°C, and the samples were maintained under the same gas flow for two hours to stabilize the temperature. Then, the adsorption and desorption consisted of switching the atmosphere from He to CO_2 stepwise. Figure 11 depicts the gas switching process. Finally, CO_2 adsorption and desorption isotherms were plotted from the experimental data after weight-averaging the loaded adsorbate at each step depicted in Figure 11.

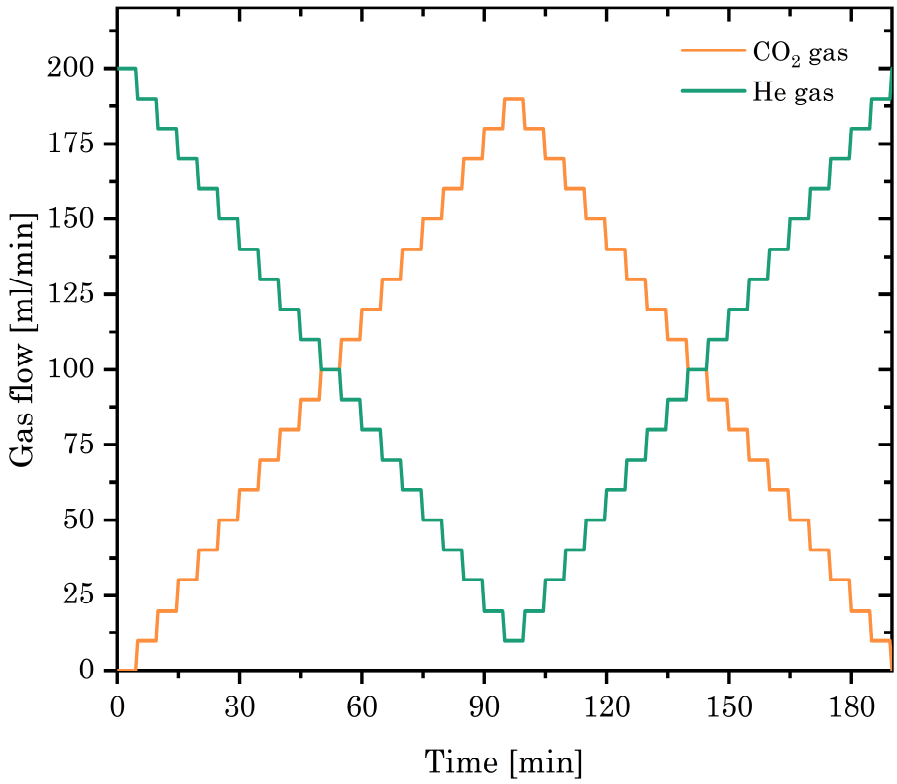

Figure 11 Isothermal CO_2 thermogravimetric adsorption and desorption sequence. The adsorption and desorption experiment consists of increasing the flow rate of CO_2 in the same proportion as the protective He gas is being reduced and vice versa

3.9 Quantitative surface chemistry

Five CF samples were selected to analyze the influence of oxygen-containing functional groups on the CO_2 uptake. With that intention in mind, X-ray photoelectron spectroscopy (XPS) was performed on samples N4, N7, N8, N11, and N16. The XPS analyses used a Kratos AXIS Ultra DLD X-ray photoelectron spectrometer using a monochromated $Al_{k\alpha}$ X-ray source (1486.7 eV) at 100 W. The XPS spectra were obtained using a pass energy of 80 eV and a step size of 1.0 eV. Alternatively, acquiring high-resolution spectra required pass energy of 20 eV and a step size of 0.1 eV. Photoelectron signals were acquired at a 90° take-off angle (ultra-high vacuum conditions). The X-ray beam had a diameter of 1 mm, and the analysis area was 300×700 μm. The XPS spectra were surveyed at three different spots in the samples. All the spectra were charge-corrected according to the position of the graphitic bonding of carbon at 284.2 eV. Appendix E shows the XPS spectra and their signals deconvolution.

4 Results and discussion

Chapter 4 presents and discusses the experimental and numerical results after characterizing the CF samples enlisted in the design matrix. The thesis attempted to model the CF yield, and to enrich the discussion, the specific surface area and microporosity volume were fitted to Eq. 3 as well. Table 3 summarizes all the CF experimental responses for the reader's convenience.

Table 3 Sampling points of the Face-centered Central Composite Design. The table compiles their CF yield ($\hat{y}_1$), BET surface area (a_s), microporosity volume (V_μ), average crystal size diameter in the basal plane (L_a), and adsorbed CO_2 for each sample.

Sample	DAP (mmol/L)	CO_2 activation (min)	BL (wt. %)	$\hat{y}_1$ (%)	a_s (m^2/g)	V_μ (cm^3/g)	L_a (nm)	CO_2 (mmol/g)*
N1	0	0	0	13.51	-	-	1.20	1.65
N2	40	0	0	24.73	-	-	1.19	1.67
N3	0	40	0	10.91	671	0.258	1.25	1.83
N4	40	40	0	22.56	576	0.219	1.29	1.80
N5	0	0	50	25.71	-	-	1.20	1.53
N6	40	0	50	27.30	-	-	1.19	1.63
N7	0	40	50	21.83	613	0.230	1.26	1.90
N8	40	40	50	24.84	524	0.199	1.26	1.72
N9	0	20	30	17.73	515	0.195	1.25	1.59
N10	40	20	30	22.72	434	0.164	1.22	1.68
N11	20	0	30	20.80	-	-	1.08	1.45
N12	20	40	30	18.86	526	0.199	1.24	1.75
N13	20	20	0	17.33	472	0.178	1.22	1.70
N14	20	20	50	23.91	484	0.184	1.24	1.66
N15	20	20	30	18.90	503	0.190	1.22	1.69
N16	20	20	30	18.54	483	0.184	1.25	1.79
N17	20	20	30	19.12	474	0.181	1.27	1.69

* Load at $p/p_0 = 0.75$

4.1 Carbon fiber yield

As Section 3.2 mentioned, OriginPro 2021b assisted in the statistical analysis of the CF yield ($\hat{y}_1$). These results were fitted to the model described in Eq. 3 using the built-in MLR tool of OriginPro. In a first trial, the factor CO_2 activation time showed a negligible effect on $\hat{y}_1$. However, knowing that the activation process should contribute to increasing the sample burn-off [67], the effect of the oxidizing atmosphere on $\hat{y}_1$ was reviewed before continuing with further experimentation and analyses. Therefore, it was found that during CO_2 activation, the elongated morphology and packed fiber clusters, such as the ones depicted in Figure 2, hindered CO_2 diffusion from the oxidizing atmosphere to the solid material. The described phenomenon led to an ineffective activation via the Boudouard reaction (Eq. 1); in other words, the mass transfer kinetics did not contribute to producing CO. For handling this experimental impediment, CF were cut into small fragments (< 5 mm), and samples having activation times different than zero were reactivated by following the same heat treatment procedure described in Section 3.3.

After reactivation, the MLR of Eq. 3 successfully modeled the observed $\hat{y}_1$ and delivered the coefficients listed in Table 4. In addition, Figure 12 depicts a comparison of the observed and predicted $\hat{y}_1$; the regression model fitting the experimental results has ~0.993 as coefficient of determination (R^2). From the model coefficients, only the quadratic term (b_{22}) for the CO_2 activation time was removed since it was indistinguishable from noise. Analyzing the effects of each factor on $\hat{y}_1$ revealed a positive influence of both DAP and lignin on increasing $\hat{y}_1$. However, this increment was more noticeable when the precursor fibers contained only one of them. The negative coefficient b_{13} implies that combining DAP and lignin had a minor synergistic effect on increasing $\hat{y}_1$; this would answer the expectation of Trogen *et al.* [31], who suggested that lignin and dehydration catalysts may further enhance $\hat{y}_1$ when used together. Regarding the independent effect of DAP and lignin, they were anticipated. For the first one, Breitenbach *et al.* [22] have recently achieved a carbonization yield of 34.6% by impregnating viscose fibers with a 56 mmol/L DAP solution. Similarly, Bai *et al.* [62] reported having increased from 19% to 23% the carbonization yield of DAP impregnated Lyocell fibers. Respecting the lignin effect on $\hat{y}_1$, Trogen *et al.* [31] have lately observed in E50 fibers a carbonization yield of ~23%, which is almost three times the yield they reported for E100 fibers.

Table 4 Coefficient list of the Multiple Linear Regression applied to the observed carbonization yields. The coefficients represent the interactions and effects of the factors on the yield.

Model	Coeff. SC	Standard error	P	Conf. int (±)
b_0	18.50	0.23	5.57×10^{-13}	0.52
b_1	3.34	0.17	4.19×10^{-8}	0.39
b_2	-1.30	0.17	5.51×10^{-5}	0.39
b_3	3.46	0.17	3.18×10^{-8}	0.39
b_{11}	0.89	0.30	1.96×10^{-2}	0.70
b_{33}	2.06	0.32	1.98×10^{-4}	0.73
b_{12}	0.23	0.19	2.53×10^{-1}	0.43
b_{13}	-2.30	0.19	1.71×10^{-6}	0.43
b_{23}	-0.18	0.19	3.63×10^{-1}	0.43

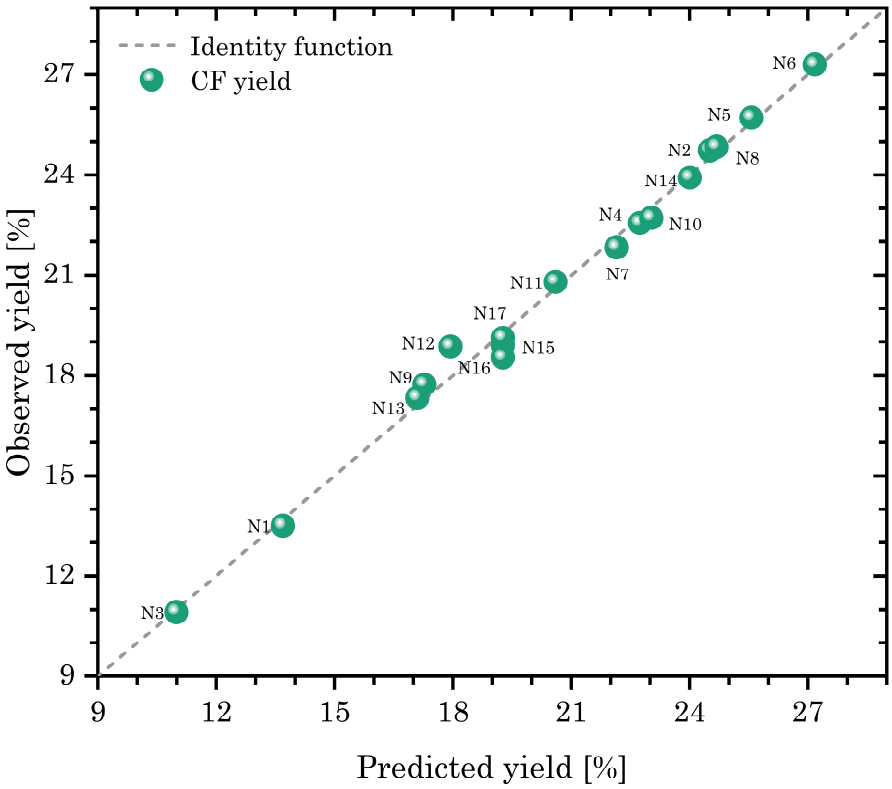

Figure 12 Observed carbonization yield compared to the predicted yield. Estimating the predicted yield occurred in OriginPro by following a Multiple Linear Regression of the design matrix inputs. The dashed line depicts an identity function.

The enhanced yield promoted by adding DAP to Ioncell fibers may stem from two phenomena. The first one could be a reduction in the dehydration temperature of cellulose [35]. The second would come from a condensation reaction between cellulose and nitrogen [35]. The observations made by Zeng and Pan [35] suggest that the C–OH group of cellulose reacts with the ammonium salt (NH_4^+) in DAP. This reaction starts producing –C=N– at ~100°C and continues up to temperatures above 800°C. This condensation process inhibits the CF ignition during pyrolysis [35]. Another alternative proposed by Zeng and Pan [35] mentions that the remaining DAP in the CF induces an apparent increment in the carbonization yield. To assess this effect, Figure 13 shows the EDS analysis on sample N10. The mapping of the CF surface confirms the observation by Zeng and Pan [35]; there is residual content of DAP in a few segments of the CF. However, Inductive Coupled Plasma Mass Spectroscopy (ICP-MS) showed that the initial content of DAP in the Ioncell fibers was ~0.04-0.2 wt.%. These percentages are in the same range as the model standard error, which turns the residual DAP into a negligible effect on $\hat{y}_1$. Concerning the effect of lignin on $\hat{y}_1$, Ioncell fiber blends (E70 and E50) have a slow decomposition over an extended temperature range [31]. Above 200°C, lignin pyrolysis promotes a melt-phase radical process, consisting initiation, propagation, and termination reactions [31]. These reactions have a similar effect to those reported on DAP; both lignin and DAP cross-link the precursor fiber [31, 35], reducing the probability of forming volatile compounds during a heat treatment [46].

On the other hand, CO_2 activation time showed a negative impact on $\hat{y}_1$. The negative sign of b_2 agrees with the literature; the samples burn-off (gasified carbon) increases by extending the CO_2 activation time [22, 67]. Nevertheless, the interactions between CO_2 gas with DAP and lignin had mixed effects on $\hat{y}_1$. First, a positive coefficient b_{12} denotes favorable interaction between the dehydration catalyst and activation time. This positive coefficient indicates that the samples containing DAP have a lower reactivity; therefore, CO_2 activation seems not to decrease the CF yield. Similar trends were observed by Breitenbach *et al.* [22] and Zeng and Pan [35]. For this thesis, it is possible that at the activation temperature (800°C), the carbonization process continues, and as a consequence, it may lead to carbon redeposition from the CO_2 atmosphere. This redeposition could occur after the recrystallization of the carbon structure and a CO_2 diffusion limitation due to residual DAP covering the CF surface, as Figure 13 illustrates. Since DAP promotes the formation of crystalline domains in the CF at ~800°C (reduced accessibility) [35], the oxidizing atmosphere may deposit carbon on the CF surface via the reversible process of the Boudouard reaction. The former statements may also explain why in Figure 14, when increasing the activation time and fixing the

DAP concentration to 40 mmol/L, the contour plot shows an extended area where the CO_2 activation does not drop the yield below 22%.

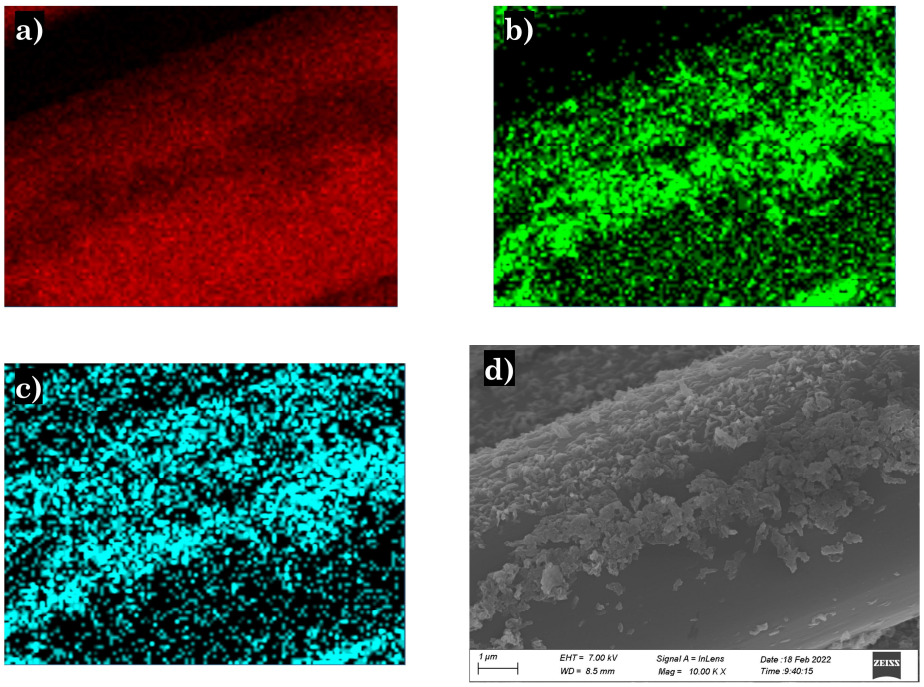

Figure 13 Energy-Dispersive Spectroscopy mapping of a) carbon, b) oxygen, and c) phosphorus in sample N10. The average composition of the d) scanned zone accounted for 89.7% C, 7.6% O_2, and 2.7% P.

The interaction between lignin and CO_2 activation time, given by b_{23}, shows that CO_2 molecules react with the carbon produced when lignin is added to the precursor fiber. Lignin should induce the formation of a turbostratic carbon structure as it modifies the long-range order of cellulose in the precursor fiber [38]. This modification on the precursor fiber could probably make the CF more accessible to CO_2 molecules. Hence the interaction coefficient b_{23} has a negative sign. However, the coefficient b_{23} is close to the standard error, and its effect should not be overanalyzed. After assessing the physical meaning of the coefficients, the contour plot in Figure 14 was created from the model response surface. Observing Figure 14, the highest $\hat{y}_1$ stemmed from mixing DAP and lignin in their maximum amounts. However, this yield is only ~2% higher than the predicted observed from the individual effects of adding either DAP or lignin at their highest levels. As mentioned before, the negative coefficient b_{13} implies that the combination of DAP and lignin does not own a significant contribution to increasing $\hat{y}_1$, as pointed out recently by Le *et al.* [61]. A better explanation of the interaction phenomena between lignin, DAP, and

cellulose would require elemental analysis of samples obtained at different carbonization stages. The former task surpasses the scope of this thesis.

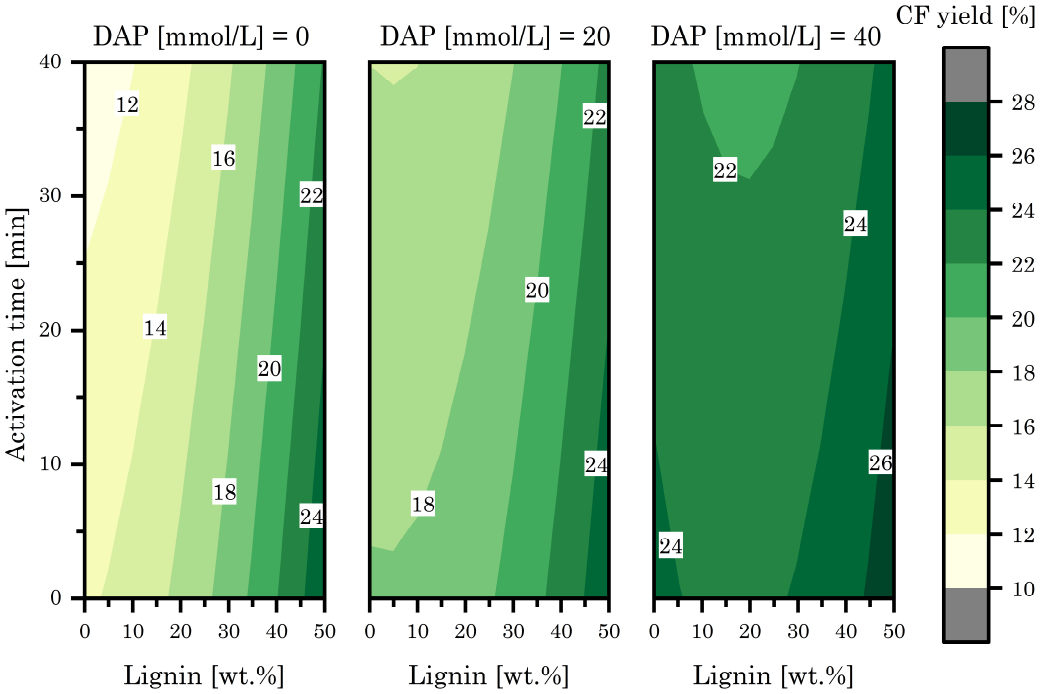

Figure 14 4-D contour plot of the predicted response surface interactions and cumulative effects of diammonium hydrogen phosphate, lignin, and CO_2 activation time on the carbon fiber yield. The plot results from a Multiple Linear Regression applied to the observed carbonization yields, $R^2 = 0.993$.

Figure 15 shows some selected thermogravimetric analysis results to understand the mass loss during carbonization better. Regarding the samples E100, E70, and E50, this thesis observed similar trends as reported by Trogen *et al.* [31]; blending cellulose with lignin increases the carbonization yield of the Ioncell fiber. Similarly, adding a dehydration catalyst to the Ioncell fibers had the same effect as the described above in the tube furnace. In other words, for sample E70/DAP, the carbonization yield is lower than the recorded for samples E100/DAP. This could imply the non-cooperative behavior of mixing lignin and DAP, at their respective concentrations, for increasing the carbonization yield. However, the yield increased when lignin and DAP were mixed at higher concentrations (E50/DAP). This effect was also observed in the tube furnace carbonizations. Finally, Figure 15 also depicts the mass loss behavior during CO_2 activation. The CO_2 activation segment demonstrated a slight mass loss (~1.5%) for all the DAP samples. These results reinforce the ideas discussed above; either the residual catalyst on the CF surface may hinder the

CO_2 gas diffusion for increasing the burn-off level, or the reactivity of these fibers is lower when the precursor fibers contain DAP.

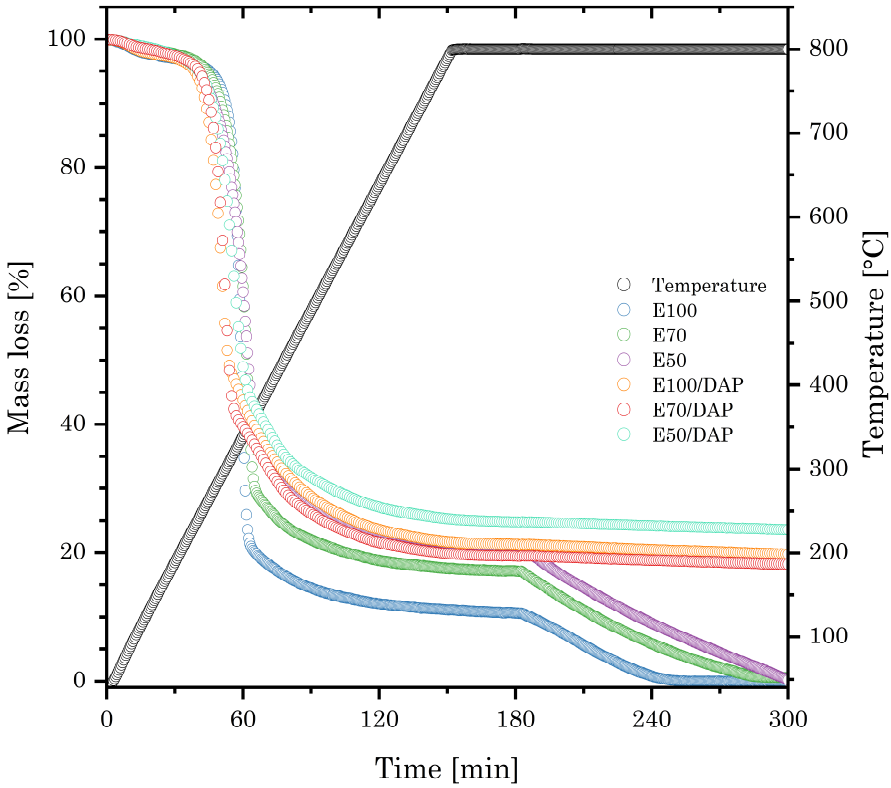

Figure 15 Thermogravimetric analysis of Ioncell fibers. The figure depicts the mass loss in percentage as a function of time and temperature by simulating the carbonization conditions in the tube furnace. That is, the samples were heated from 40 to 800°C (5°C/min) under flowing N_2 gas (60 ml/min) and then stabilized for 30 minutes at 800°C. After the stabilization time elapsed, CO_2 was injected to match the N_2 gas flow. The CO_2 activation segments can be observed in the graph after 180 min. Samples E100, E70, and E50 containing DAP shared the same impregnation as N2, N10, and N6, respectively.

4.2 Textural characterization

Determining the BET specific surface area (a_s) required measuring N_2 adsorption isotherms at -196°C. In past years, a_s as a parameter to assess the texture of activated carbons has raised divided opinions [46, 79]. However, more critical for this research is the ambiguous procedure to calculate a_s, a problem recently exposed by Osterrieth *et al.* [102]. Therefore, for analyzing the N_2 adsorption isotherms, this thesis took advantage of "pyGAPS", a Python-based framework for processing adsorption isotherms [101]. Iacomi and Llewellyn

[101] developed pyGAPS to standardize the mathematics involved in adsorption isotherms analysis. This thesis compared the results obtained from pyGAPS with those generated from "betsi-gui" [113]. Similar to pyGAPS, betsi-gui is a Python-based framework for calculating BET surface areas using the Rouquerol criteria. After processing the adsorption isotherms with both Python tools, this study concluded that pyGAPS and betsi-gui lead to the same a_s results. Thus, both tools have demonstrated an asset in standardization.

For the analyses, this thesis preferred using pyGAPS, since it offers various algorithms to calculate other textural properties, such as V_μ. Appendix C collects the graphs produced from pyGAPS; these plots illustrate the procedures to calculate a_s and V_μ. Table 3 summarizes the outcomes of processing the isotherms. As shown in Figure 16, CF samples without activation protocol display no measurable N_2 physisorption. Thus, Table 3 misses a_s and V_μ of these samples. In general, the isotherms (Figure 16) depicted high gas adsorption at low relative pressures ($p/p_0 < 0.1$) followed by a sharp knee, turning the gas adsorption asymptotic to a maximum. This adsorption behavior corresponds to the IUPAC classification type I(a), a characteristic of microporous materials [114]. The microporous nature of the studied CF explains the lack of adsorption data for the unactivated samples. The diffusion kinetics of N_2 molecules into the solid carbon, at the experimental temperature (-196°C), finds limitations due to the narrow pore size (< 2 nm) [115]. To overcome this diffusion constraint, multiple authors have suggested complementing the N_2 adsorption isotherms with CO_2 isotherms at room temperature [115-117].

From the isotherms in Figure 16, a_s and V_μ were calculated according to the BET theory and t-plot method, respectively. Then, assessing the influence of each experimental factor on the textural properties relied on calculating the regression parameters presented in Eq. 3 for a_s and V_μ. Intrinsically, the responses missing from the unactivated samples removed the coefficient b_{22} from the response surface analysis. Eliminating the coefficient b_{22} agrees with the CF yield response surface analysis, implying that the CO_2 activation time had only a linear effect on increasing the burn-off level and developing porosity. For the other regression coefficients, Table 5 and Table 6 summarize them. The models for a_s and V_μ showed similar trends. For example, from the linear coefficients, the CO_2 activation time (b_2), followed by the lignin content (b_3), had the most significant effect on increasing a_s and V_μ. The effect of b_2 can be attributed to an increment of the burn-off level after gasifying carbon from the CF [67], as Figure 7 depicted.

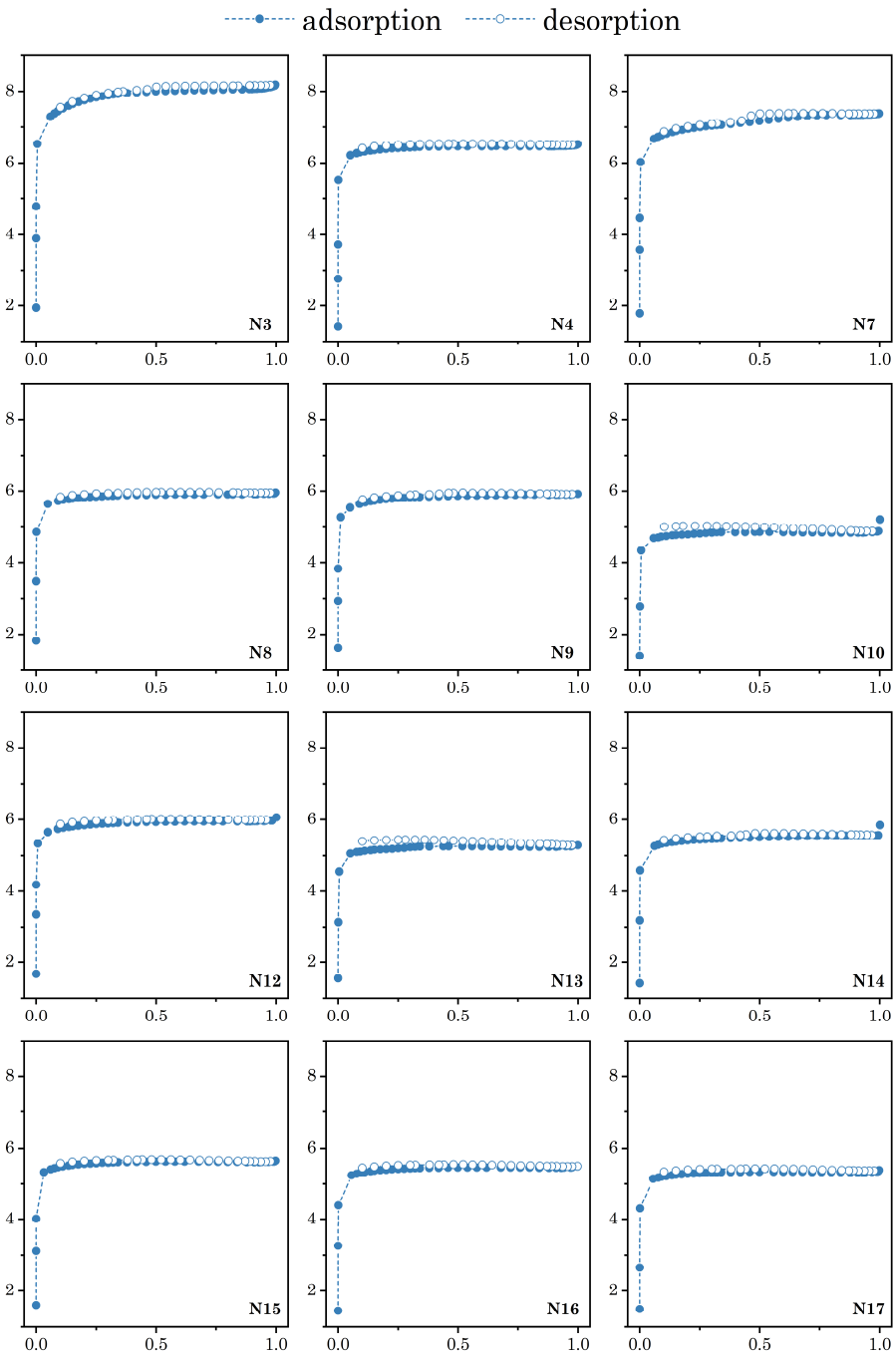

Figure 16 Nitrogen adsorption and desorption isotherms of the samples composing the Face-centered Central Composite Design. The abscissa in each plot represents the relative pressure (p/p_0) and the ordinate the N_2 load in mmol/g.

Table 5 Coefficient list of the Multiple Linear Regression applied to the calculated BET surface areas. The coefficients represent the interactions and effects of the factors on the carbon fiber textural property. $R^2 = 0.941$.

Model	Coeff. SC	Standard error	t-Value	Prob > |t|
b_0	472.24	12.26	131.17	5.81×10^{-5}
b_1	-40.8	19.20	-11.33	7.70×10^{-3}
b_2	92.58	18.35	25.72	1.51×10^{-3}
b_3	9.39	18.92	2.61	1.21×10^{-1}
b_{33}	22.71	18.96	6.31	2.42×10^{-2}
b_{12}	-5.20	23.44	-1.44	2.85×10^{-1}
b_{13}	1.50	13.44	0.42	7.17×10^{-1}
b_{23}	-38.58	23.11	-10.72	8.59×10^{-3}

Table 6 Coefficient list of the Multiple Linear Regression applied to the calculated microporosity volume. The coefficients represent the interactions and effects of the factors on the carbon fiber textural property. $R^2 = 0.944$.

Model	Coeff. SC	Standard error	t-Value	Prob > |t|
b_0	1.79×10^{-1}	4.62×10^{-3}	166.36	3.61×10^{-5}
b_1	-1.57×10^{-2}	7.23×10^{-3}	-14.62	4.64×10^{-3}
b_2	3.58×10^{-2}	6.91×10^{-3}	32.29	9.01×10^{-4}
b_3	4.42×10^{-3}	7.13×10^{-3}	4.11	5.44×10^{-2}
b_{33}	8.29×10^{-3}	7.14×10^{-3}	7.71	1.64×10^{-2}
b_{12}	-1.75×10^{-3}	8.83×10^{-3}	-1.63	2.45×10^{-1}
b_{13}	2.07×10^{-3}	5.06×10^{-3}	1.9	1.94×10^{-1}
b_{23}	-1.70×10^{-2}	8.70×10^{-3}	-15.87	3.95×10^{-3}

However, the coefficient b_0, representing the intercept of the model, is relatively high compared with the experimental results of a_s. This high value complicates interpreting the physical meaning of all the other parameters, as their influence on a_s is small and close to the standard error. Therefore, the following discussion is not definitive and only open space for explaining possibilities. Having stated that, the positive linear coefficient b_3 could mean that adding lignin to the precursor fiber enhances the surface area; this also would explain the positive coefficient for b_{33}. Alternatively, the DAP impregnation

seemed to influence the textural properties negatively. At this point, the residual content of DAP on the CF may have hindered the diffusion of N_2 molecules into the solid carbon, or simply the CF structure is less porous due to different pyrolysis pathways. To reduce the effects of overfitting, b_{11} was re-

a)

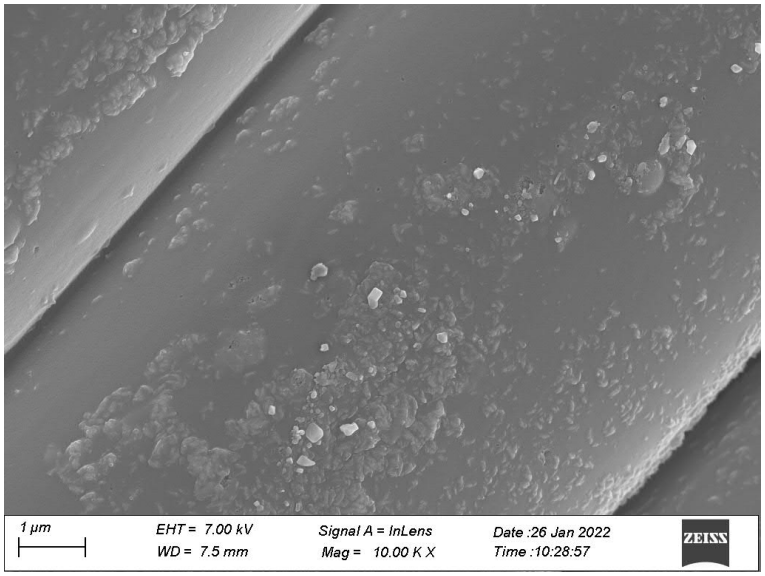

b)

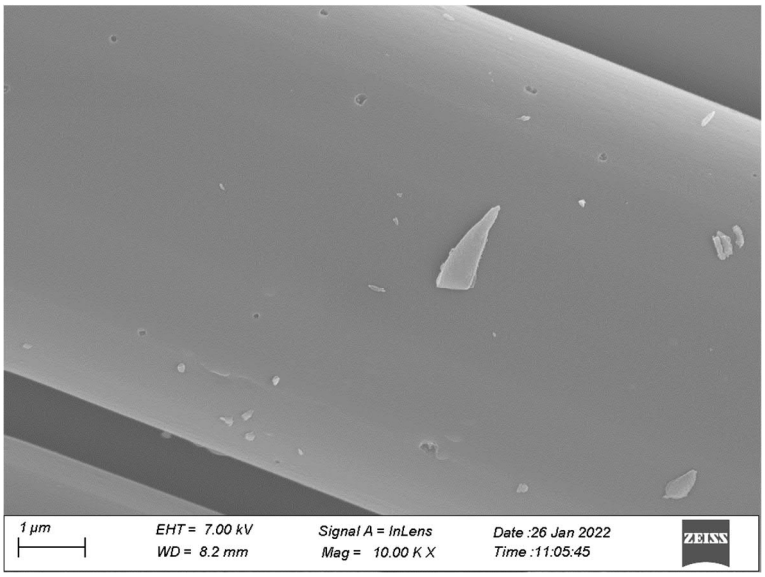

Figure 17 Scanning electron microscopy image of samples a) N8 and b) N9. Sample N8 was produced from E50 fibers impregnated with diammonium hydrogen phosphate. N9 was produced from E50 fibers. Both samples were activated for 40 minutes under a CO_2 atmosphere.

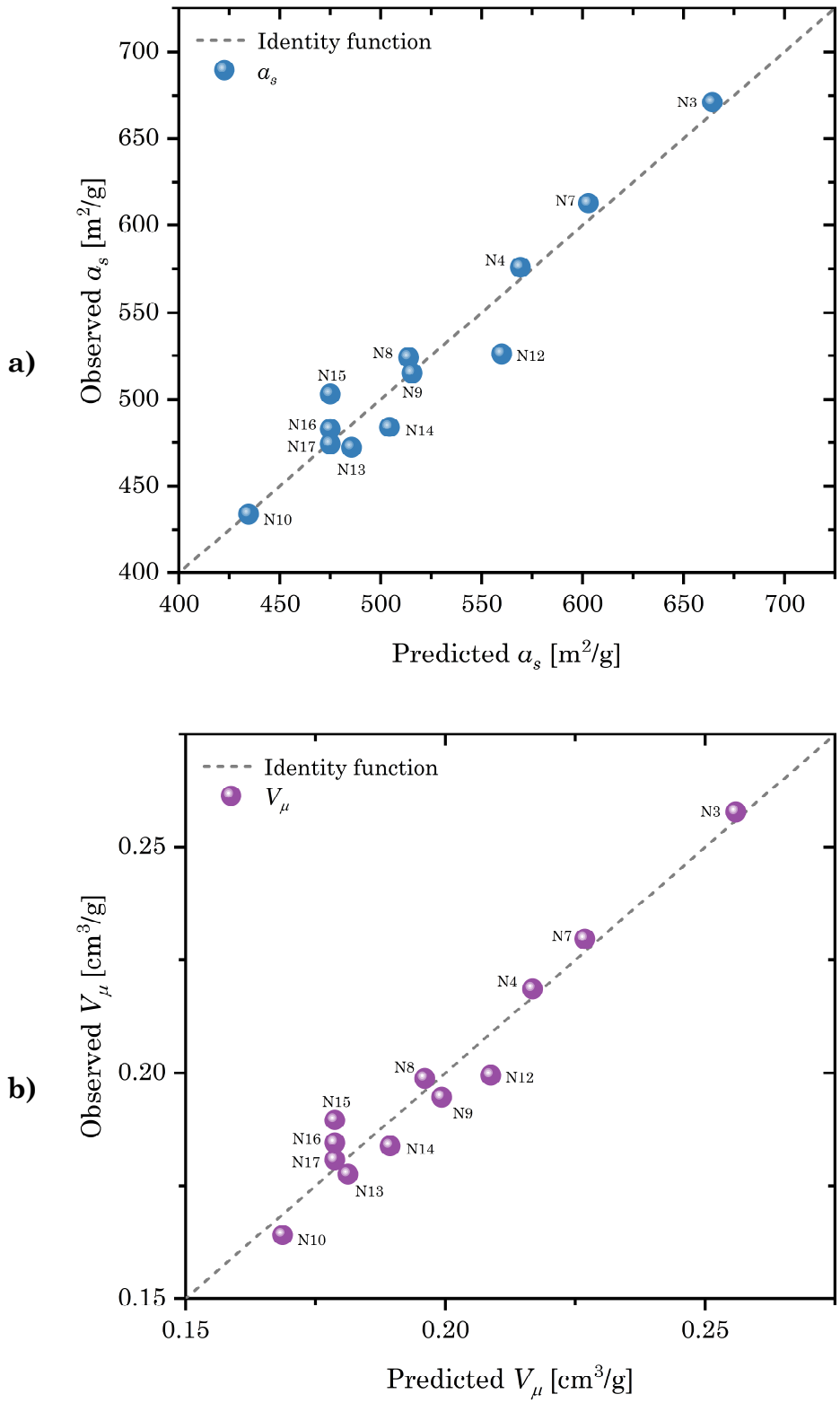

Figure 18 Observed a) BET surface area and b) volume of microporosity compared to their predictions. The predictions stem from a Multiple Linear Regression of the design matrix inputs. The dashed line depicts an identity function.

moved from the model. Zeng and Pan [35] reported that washing off the CF effectively removes the residual DAP content. Therefore, future research should assess the effects of adopting this practice on CF properties.

Regarding the interaction coefficients, DAP and CO_2 activation time did not show an increasing effect (b_{12}) on a_s, similar as observed for $\hat{y}_1$. The residual catalyst and possible crystallization of the CF induced by DAP at the carbonization temperature (800°C) may have blocked CO_2 diffusion and removal of solid carbon from the CF matrix [35]. In order to explain the physical meaning of the coefficient b_{13}, the discussion requires analyzing the SEM images of the CF samples containing DAP and lignin. Hence, to explain the possible interaction between lignin and DAP, Figure 17 a) shows a close-up of the surface of sample N8. The SEM image presents evidence of the phenomenon suspected in Section 4.1. The melt-phase pyrolysis of lignin and DAP seemed to create "eruptions" on the CF surface while leaving the residual DAP content underneath the surface. These rearrangements in the CF may leave some micropores to which N_2 molecules are accessible. The negative sign of b_{23}, lignin,

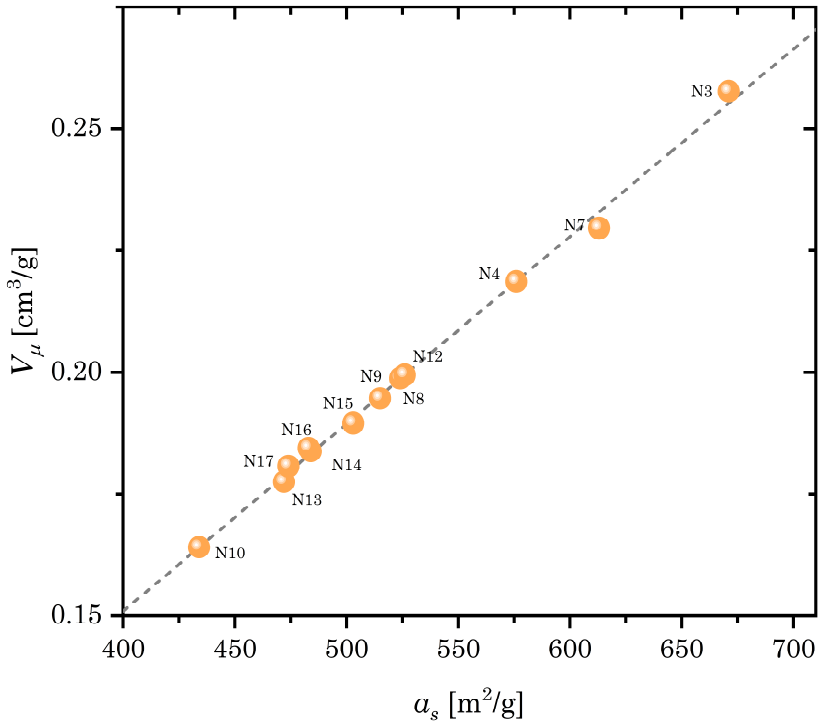

Figure 19 Correlation between BET surface area and volume of microporosity of the samples composing the Face-centered Central Composite Design. The dashed line denotes a linear fit with intercept and slope, ~0 cm^3/g and 3.85×10^{-4}, respectively.

and CO_2 activation time could create larger pores instead of micropores, as Figure 17 b) shows. Figure 18 compares the observed properties and the predicted ones. In both cases, the distribution of the scatter points tends to follow an identity function, which suggests a good fitting of the textural properties. However, as Table 5 and Table 6 show, several parameters are close to the standard error, implying that the conclusions made from a_s and V_μ models may not be absolute.

Finally, to assess the relationship between a_s and $V\mu$, Figure 19 depicts a correlation between these two textural properties. In Section 2.3, this thesis highlighted the importance of measuring the pore volume to assess the confidence of a_s as a property to characterize carbon samples. Figure 19 demonstrates that a_s of CF stems primarily from the formation of micropores, as the scatter points in Figure 19 align linearly [118]. Therefore, for the studied, microporous CF, a_s portrays itself as sensible property to characterize the material texture.

4.3 Raman spectroscopy

Carbonizing non-graphitizable precursors, such as cellulose and lignin, produces disordered (turbostratic) carbon structures constituted by graphene layers, missing local molecular orientation [106, 119]. In other words, these turbostratic carbons present several misorientation defects. According to Orbelin's [119] observations, cross-linking reactions, like those occurring in cellulose and lignin at low pyrolysis temperatures (< 600°C), hinder the formation of graphene stacks which translates into a modest average crystal size L_a [106]. Thus, the studied Ioncell CF should possess turbostratic structures because of their intrinsic non-graphitizable nature and the presence of DAP on the precursor fibers. DAP has been reported to induce cross-linked functionalities as a mechanism to impede the release of small volatile carbon compounds, as discussed in Section 4.1 [35]. Figure 20 illustrates the Raman spectra of all the studied CF samples. The maxima of the sp^2 C bonding excitation (G band) was at $\omega \approx$ 1590-1594 cm^{-1}. Alternatively, the D band connected to the formation of six-fold aromatic rings and point defects had their maxima at $\omega \approx$ 1337-1346 cm^{-1} [106, 110]. Based on Ferrari's and Robertson's [110] findings, the D band intensity (I_D) would be directly proportional to the probability of finding polyaromatic (six-fold rings) structures in the CF. Therefore I_D/I_G ratio is one of several standard procedures used to estimate the crystallite size L_a [106, 108-110].

To calculate the parameter L_a for every CF sample, this thesis opted for the methodology proposed by Mallet-Ladeira *et al.* [108, 109] and Mubari *et al.*

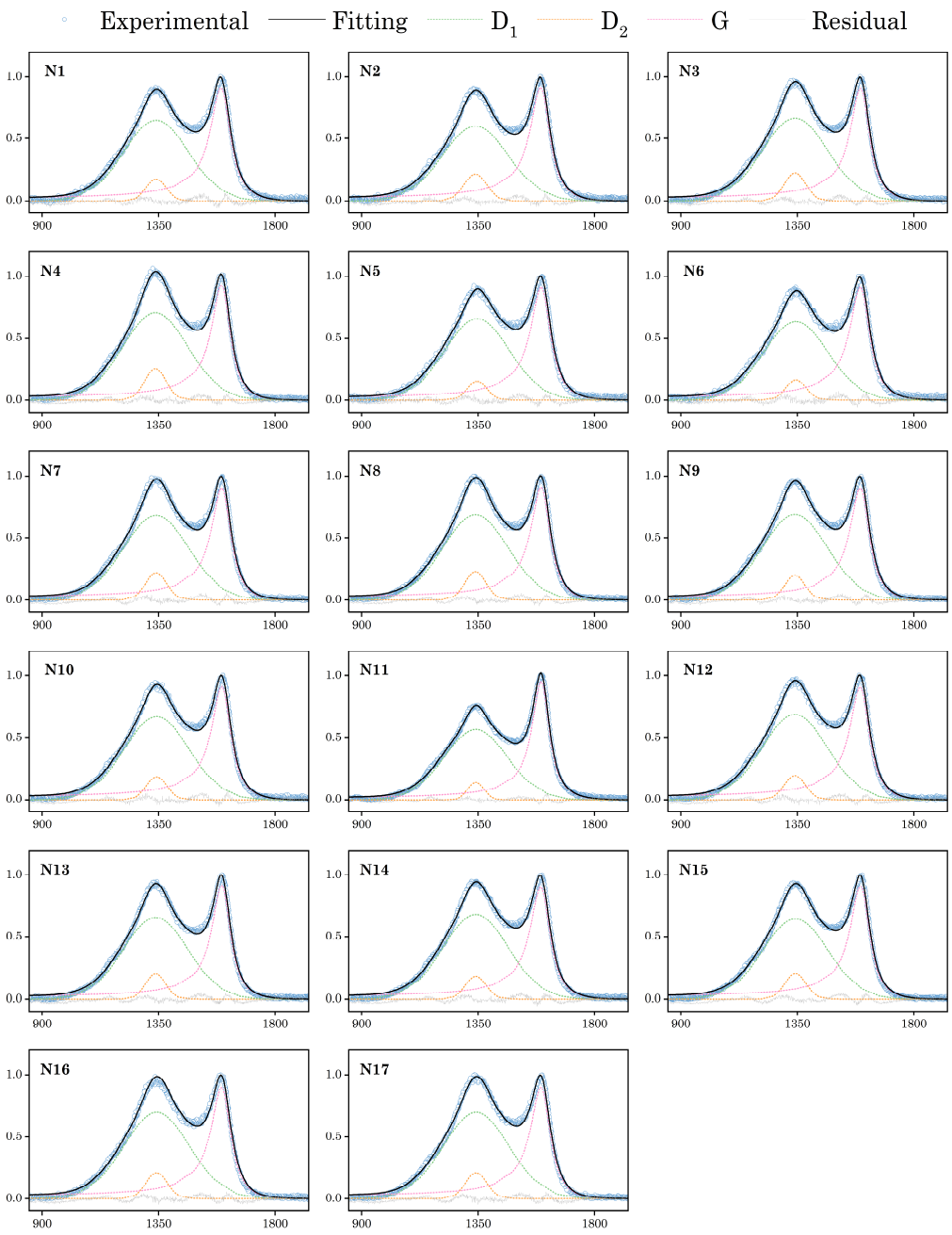

Figure 20 Raman spectra of the samples composing the Face-centered Central Composite Design. The abscissa in each plot represents the Raman shift wavenumber in cm^{-1}, and the ordinate is the G band normalized Raman intensity in arbitrary units. The solid line depicts the cumulative fit in each spectrum after decomposing the experimental spectrum in three bands: two Gaussian functions at the exact wavenumber for the D band and one Breit-Wigner-Fano function for the G band.

[106], which derives the I_D/I_G ratio from a three-peak deconvolution of the Raman spectra. The decomposition or deconvolution process consisted of fitting the D band using two Gaussian functions sharing the same spectral position, while the G band was fitted using a BWF function. Although Mallet-Laderia [108, 109] originally proposed using two Lorentzian functions to deconvolve the D band, in biobased carbons, the presence of a shoulder at 1100-1200 cm^{-1} turns the D band shape into a Gaussian-like one [120]. Furthermore, the low carbonization temperature of 800°C contributes to observing broad D and G bands, a phenomenon attributed in nanomaterials to a confinement effect [121]. Alternatively, the BWF function allows fitting the asymmetric G band typical of disordered carbons, whose shape moves away from a perfect Lorentzian because of the density of vibrational states [109, 110, 122]. Figure 20 shows the outcomes of the deconvolution process. The procedure offered an excellent fitting of the experimental data for all the spectra ($R^2 \approx 0.996$-0.997).

Table 7 Characteristics of the D and G bands fitted using a three-peaks deconvolution of the Raman spectra.

Sample	$FWHM_{D1}$	$FWHM_{D2}$	ω_D	$FWHM_G$	ω_G	I_D/I_G	L_a
N1	295	91.0	1340	97.8	1591	0.90	1.20
N2	301	103.5	1339	96.2	1592	0.89	1.19
N3	299	96.6	1341	93.5	1594	0.98	1.25
N4	299	98.2	1337	92.5	1593	1.04	1.29
N5	296	89.1	1346	99.0	1593	0.90	1.20
N6	294	92.6	1344	99.1	1593	0.88	1.19
N7	301	97.2	1340	95.0	1593	0.99	1.26
N8	301	97.0	1340	94.8	1593	1.00	1.26
N9	300	93.2	1340	95.5	1593	0.98	1.25
N10	296	92.4	1342	95.1	1594	0.94	1.22
N11	288	74.2	1341	83.5	1594	0.74	1.08
N12	299	95.7	1340	96.9	1592	0.97	1.24
N13	295	91.2	1338	90.0	1594	0.94	1.22
N14	298	94.1	1341	97.2	1592	0.96	1.24
N15	297	96.7	1342	94.5	1594	0.94	1.22
N16	300	95.9	1340	97.9	1590	0.97	1.25
N17	302	98.7	1342	97.5	1593	1.01	1.27

The crystallite sizes L_a and characteristics of the fitted bands are collected in Table 7. Ferrari's and Robertson's law (Eq. 5) was adequate for calculating L_a, since the crystal parameter was smaller than 2 nm in all the cases [110]. However, as observed in Table 7, the samples displayed similar L_a values (~1.2 nm) despite their initial composition. An explanation for this observation relies on the effect of the maximum carbonization temperature and heating rate, which remained fixed at 800°C and 5°C/min. Modifying the thermal carbonization parameters significantly affects the crystal size as the pyrolysis kinetics change. For example, Mubari *et al.* [106] and Breitenbach *et al.* [96] have reported the influence of the carbonization temperature and heating rate on the crystal size of biobased carbons, respectively. A higher carbonization temperature, as well as a slower heating rate, could increase L_a. The former would explain why the response surface analysis would not correlate L_a with the FCCD.

4.4 CO_2 adsorption performance

The CO_2 adsorption and desorption performance of the CF was measured via thermogravimetry. Appendix D shows the adsorption and desorption isotherms of all the CF samples. Overall, the isotherms depict almost negligible hysteresis, a characteristic typically observed in ultramicroporous materials [123-125]. At the experimental temperature (40°C), the lack of hysteresis is observed since there are no kinetic restrictions for the CO_2 molecules to move through the narrow micropores [125]. This feature may also indicate that the studied CF adsorb CO_2 molecules physically (physisorption). In order to assess the physisorption mechanism, this thesis attempted to correlate the CF textural properties with their CO_2 adsorption capacity. Thus, the adsorption isotherms were fitted using Freundlich's equation, the most simple adsorption model [126]. Freundlich's empirical equation describes the adsorption as a phenomenon following the Power-law behavior expressed in Eq. 6. In Eq. 6, X is the adsorbate mass normalized by the adsorbent mass while C and r are adsorption constants for the pair adsorbate-adsorbent at the experimental temperature. In this case, p_0 represents the atmospheric pressure.

$$X = C \cdot \left(\frac{p}{p_0}\right)^{1/r} \qquad \text{Eq. 6}$$

Jaroniec [127] demonstrated that C could be related to heterogeneities present in the adsorbent, which, in this case, could translate to the CF textural

properties. Hence, Figure 21 plots the calculated C values as a function of the BET surface areas (Section 4.2). Although Figure 21 shows that the parameter C tends to increase as a function a_s, any straightforward linear or exponential relationship is observed between the empirical parameter C and a_s. Therefore, it is only acceptable to conclude that the observed CO_2 adsorption capacity depends on the CF surface area but is not restricted to it. Especially in bi-obased activated carbons, Ashourirad *et al.* [128] underlined that the CO_2 adsorption capacity depends on the oxygen functionalities.

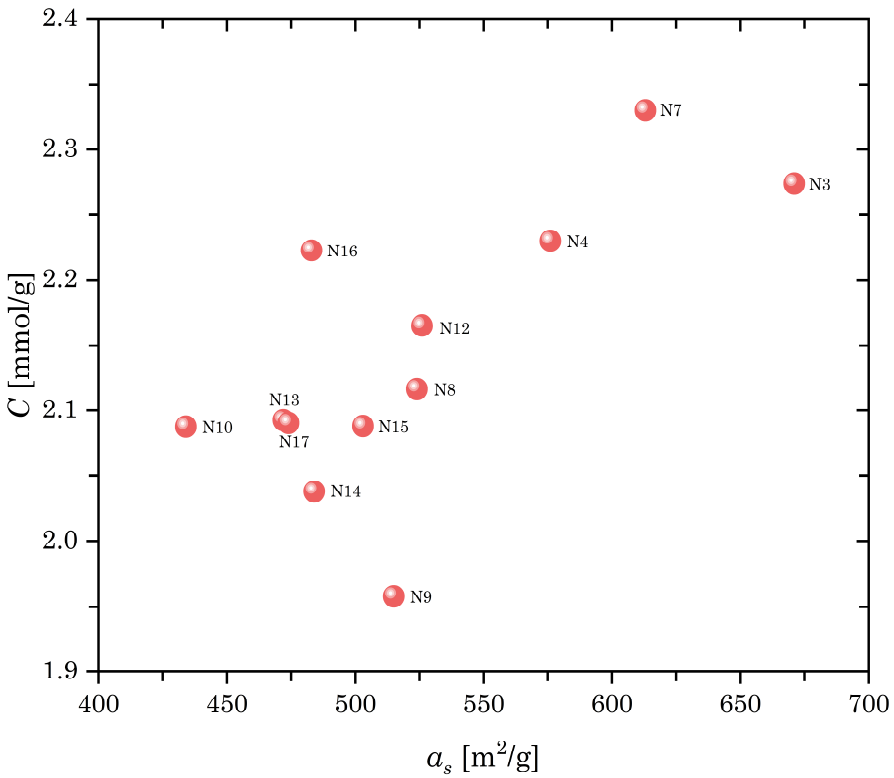

Figure 21 Freundlich's empirical parameter C plotted as a function of the calculated BET surface areas of the samples composing the Face-centered Central Composite Design.

Therefore, five CF samples (N4, N7, N8, N11, and N16) were analyzed using XPS to evaluate the influence of oxygen functional groups on the CO_2 adsorption performance. Appendix E show the XPS spectra, and Table 8 collects the relative concentrations of elements in the samples. All the samples showed the respective signals for C, N, O, and P; moreover, Ca traces were also detected. From the results in Table 8, it is possible to conclude that the content of oxygen-containing functionalities affects the adsorption performance; that is, the CO_2 adsorption increases as the oxygen concentration is higher in the

samples. The relationship between the oxygen functionalities and CO_2 adsorption is usually neglected; however, oxygen sites in the CF may increase the CO_2 uptake as they polarize and "trap" the CO_2 adsorbate molecules in the micropores via dipole-dipole and quadrupole van der Waals interactions [128-132]. Thus, the observed differences in the CF chemistry would explain why CF having a large surface area did not display the highest CO_2 uptake in some cases. For example, comparing samples N4 and N7, the first one exhibited the largest surface area, but it adsorbed less CO_2 than sample N7. By observing the precursor chemistry of these samples (Table 3), it can be noticed that N7 contained lignin. Pyrolyzed lignin may have led to generating more oxygen functionalities in the final CF. Accordingly, N7 had a higher CO_2 adsorption capacity than N4. Similarly, the oxygen content in sample N11 might explain its CO_2 adsorption performance despite not having exhibited a measurable surface area. All in all, the studied samples showed high CO_2 adsorption. This capacity could be used in the future to prepare gas separation membranes and CO_2 storage systems. Furthermore, it is clear that for modeling the CO_2 uptake, both the textural and chemical heterogeneities in the CF need to be considered.

Table 8 Quantitative relative surface chemistry estimated from X-ray photoelectron spectroscopy. The BET surface area (a_s) and CO_2 uptake are presented to illustrate the effect of both the texture and surface chemistry on the adsorption performance.

CF	C 1s (wt.%)	Ca 2p (wt.%)	N 1s (wt.%)	O 1s (wt.%)	P 2p (wt.%)	a_s (m^2/g)	CO_2 load* (mmol/g)
N4	94.44	0.42	0.11	4.48	0.56	576	1.80
N7	92.48	0.57	0.65	6.30	0.00	613	1.90
N8	93.10	0.64	0.55	4.97	0.74	524	1.72
N11	89.57	1.16	0.44	7.55	1.29	-	1.45
N16	89.11	0.84	0.56	8.55	0.94	483	1.79

* Load at $p/p_0 = 0.75$

N4: 40 mmol/L impregnation, 40 minutes activation time, and 0 lignin wt.%
N7: 0 mmol/L impregnation, 40 minutes activation time, and 50 lignin wt.%
N8: 40 mmol/L impregnation, 40 minutes activation time, and 50 lignin wt.%
N11: 20 mmol/L impregnation, 0 minutes activation time, and 30 lignin wt.%
N16: 20 mmol/L impregnation, 20 minutes activation time, and 30 lignin wt.%

5 Conclusions

This thesis demonstrated the potential use of Ioncell technology to fabricate CF, which could satisfy the global demand for synthetic carbons. The model created from the response surface successfully assessed the impact of the factors DAP impregnation, CO_2 activation time, and lignin content on the carbonization yield of Ioncell fibers. This thesis showed that both DAP and lignin could modify Ioncell pyrolysis positively in terms of carbonization yield. DAP increases the carbonization yield of Ioncell as it drops the dehydration temperature of cellulose and cross-links the carbon atoms, preventing their volatilization. Similarly, lignin reduces the dehydration temperature of the Ioncell fibers and shifts their major degradation to higher temperatures, as observed in the TGA results. Recalling the aim of the thesis, which was to increase and model the carbonization yield of Ioncell fibers, it is possible to conclude that the aim was achieved since the carbonization yield increased from ~13 to 27%.

Interpreting the regression coefficients of the carbonization yield model showed that combining DAP and lignin has no direct effect on increasing the yield. In fact, there is a range in which the synergy between DAP and lignin seems to affect the carbonization yield negatively. Since the SEM images showed residual catalyst trapped underneath the CF surface, this work introduced the possibility of melt-phase interactions occurring between DAP and lignin, which may have hindered the mechanisms enhancing Ioncell carbonization yield. Likely, the catalyst cannot enter the lignin domain, and it precipitates. Regarding the effect of CO_2 activation time, almost all the samples showed a low reactivity. This work attributed the low reactivity to mass diffusion constraints at the carbonization conditions and to cross-linked carbon atoms, which may arise in CF upon the addition of DAP to the precursor fibers. However, a more detailed study of the pyrolysis phases would be necessary to confirm the hypothesis.

This manuscript tried to answer many controversies found in the literature. First, the work explained why the carbon surface area should not be directly correlated with the material performance in specific applications. Herein was exemplified the case of BET surface area and CO_2 adsorption. The results showed that, especially in biochars, the precursor chemistry generates oxygen-containing functionalities, which may significantly contribute to the CO_2 uptake capacity of CF. Similar effects should be assessed when establishing property-performance relationships for carbon materials. Second, this thesis supported the use of methods developed by other authors. In the case of calculating the textural properties, the results obtained using pyGAPS should motivate researchers to employ similar tools for standardizing the mathematics

behind adsorption isotherms treatment. Concerning the Raman spectra decomposition, the methodology of using a three-peak deconvolution proved its applicability to fit the asymmetric G and D bands observed in biobased carbons.

The author of this thesis acknowledges that the regression model found limitations when extending it to analyze other responses, such as BET surface area, average crystallite diameter in the basal plane, and CO_2 adsorption. Therefore, this study concluded that it is necessary to include different factors to establish a more solid framework for describing the aforementioned responses. For example, to develop CF with different crystal structures, it is required to analyze this response under varying thermal heat treatment conditions. Therefore, future research should consider varying the maximum carbonization temperatures and heating rate. Furthermore, it would be essential to try a different activation method for the CF since the research showed that adding DAP to the precursor fibers reduced the CF reactivity with CO_2.

All in all, this thesis accomplished its aim as the experimental work achieved increasing the carbonization yield of Ioncell fibers, and it modeled the combined effects of DAP, CO_2 activation, and lignin. The present study contributed by generating knowledge about the nanostructure, texture, and surface chemistry of Ioncell CF. The discussed ideas will drive future research toward optimizing a response in particular. Furthermore, as the methodologies to study the CF are well described in this manuscript, future research should speed up the characterization and mathematical processes. Concerning this thesis, the study demonstrated that Ioncell fibers could adsorb relatively high amounts of carbon dioxide. Further tunning of the CF texture and surface chemistry may increase the CO_2 uptake even more. This thesis foresees gas separation membranes and CO_2 capture systems as future applications for the studied CF.

References

[1] P. Stegmann, M. Londo, and M. Junginger, "The circular bioeconomy: Its elements and role in European bioeconomy clusters," *Resources, Conservation & Recycling: X,* vol. 6, no. July 2019, pp. 100029-100029, 2020, doi: 10.1016/j.rcrx.2019.100029.

[2] J. Sherwood, "The significance of biomass in a circular economy," *Bioresource Technology,* vol. 300, no. November 2019, pp. 122755-122755, 2020, doi: 10.1016/j.biortech.2020.122755.

[3] D. D'Amato, S. Veijonaho, and A. Toppinen, "Towards sustainability? Forest-based circular bioeconomy business models in Finnish SMEs," *Forest Policy and Economics,* vol. 110, no. June 2018, pp. 101848-101848, 2020, doi: 10.1016/j.forpol.2018.12.004.

[4] G. Ceccherini *et al.*, "Abrupt increase in harvested forest area over Europe after 2015," *Nature,* vol. 583, no. 7814, pp. 72-77, 2020, doi: 10.1038/s41586-020-2438-y.

[5] E. Commission, "Innovating for a Sustainable Growth: A Bioeconomy for Europe," 2012, doi: 10.2777/6462.

[6] Directive (eu) 2019/904 of the european parliament and of the council of 5 june 2019 on the reduction of the impact of certain plastic products on the environment, 2019.

[7] T. Lohtander, R. Herrala, P. Laaksonen, S. Franssila, and M. Österberg, "Lightweight lignocellulosic foams for thermal insulation," *Cellulose,* 2022, doi: 10.1007/s10570-021-04385-6.

[8] R. Li *et al.*, "Ultra-lightweight cellulose foam material: preparation and properties," *Cellulose,* vol. 24, no. 3, pp. 1417-1426, 2017, doi: 10.1007/s10570-017-1196-y.

[9] M. Reichler *et al.*, "Scalable method for bio-based solid foams that mimic wood," *Scientific Reports,* vol. 11, no. 1, 2021, doi: 10.1038/s41598-021-03764-0.

[10] "Tencel." https://www.tencel.com/ (accessed 24 Jan 2022).

[11] J. Oelerich, M. Bijleveld, G. H. Bouwhuis, and G. J. Brinks, "The life cycle assessment of cellulose pulp from waste cotton via the SaXcell™ process," *IOP Conference Series: Materials Science and Engineering,* vol. 254, 2017, doi: 10.1088/1757-899x/254/19/192012.

[12] K. Moriam *et al.*, "Towards regenerated cellulose fibers with high toughness," *Cellulose,* vol. 28, no. 15, pp. 9547-9566, 2021, doi: 10.1007/s10570-021-04134-9.

[13] J. Trifol and R. Moriana, "Barrier packaging solutions from residual biomass: Synergetic properties of CNF and LCNF in films," *Industrial Crops and Products,* vol. 177, 2022, doi: 10.1016/j.indcrop.2021.114493.

[14] K. Huang and Y. Wang, "Recent applications of regenerated cellulose films and hydrogels in food packaging," *Current Opinion in Food Science,* vol. 43, pp. 7-17, 2022, doi: 10.1016/j.cofs.2021.09.003.

[15] A. N. M. A. Haque and M. Naebe, "Sustainable biodegradable denim waste composites for potential single-use packaging," *Science of The Total Environment,* vol. 809, 2022, doi: 10.1016/j.scitotenv.2021.152239.

[16] M. E. Reyes-Melo, I. Y. Miranda-Valdez, J. G. Puente-Córdova, C. A. Camarillo-Hernández, and B. López-Walle, "Fabrication and characterization of a biocompatible hybrid film based on silver nanoparticle/ethyl cellulose polymer," *Cellulose,* vol. 28, no. 14, pp. 9227-9240, 2021, doi: 10.1007/s10570-021-04066-4.

[17] C. Qin and A. Lu, "Flexible, anti-freezing self-charging power system composed of cellulose based supercapacitor and triboelectric nanogenerator," *Carbohydrate Polymers,* vol. 274, 2021, doi: 10.1016/j.carbpol.2021.118667.

[18] A. Liu *et al.*, "A renewable membrane with high ionic conductivity and thermal stability for Li-ion batteries," *Journal of Power Sources,* vol. 521, 2022, doi: 10.1016/j.jpowsour.2021.230947.

[19] (2020). *Critical Raw Materials Resilience: Charting a Path towards greater Security and Sustainability*. [Online] Available: https://eur-lex.europa.eu/legal-content/EN/TXT/?uri=CELEX:52020DC0474

[20] C. Ma *et al.*, " Preparation and one-step activation of nanoporous ultrafine carbon fibers derived from polyacrylonitrile / cellulose blend for used as supercapacitor electrode," *Journal of Materials Science,* vol. 53, no. 6, pp. 4527-4539, 2018, doi: 10.1007/s10853-017-1887-7.

[21] S. S. Choi, J. H. Lee, Y. M. Jin, and S. H. Lee, "Adsorption characteristics of volatile organic compounds onto lyocell-based activated carbon fibers," *Carbon Letters,* vol. 29, no. 6, pp. 633-642, 2019, doi: 10.1007/s42823-019-00063-7.

[22] S. Breitenbach *et al.*, "Supercapacitor electrodes from viscose-based activated carbon fibers: significant yield and performance improvement using diammonium hydrogen phosphate as impregnating agent," *C — Journal of Carbon Research,* vol. 6, no. 2, pp. 17-17, 2020, doi: 10.3390/c6020017.

[23] S. Haider, J. Lie, A. Lindbråthen, and M.-B. Hägg, "Pilot–scale production of carbon hollow fiber membranes from regenerated cellulose precursor-

Part I: Optimal conditions for precursor preparation," *Membranes,* vol. 8, no. 4, 2018, doi: 10.3390/membranes8040105.

[24] S. Haider, J. Lie, A. Lindbråthen, and M.-B. Hägg, "Pilot–scale production of carbon hollow fiber membranes from regenerated cellulose precursor-Part II: Carbonization procedure," *Membranes,* vol. 8, no. 4, 2018, doi: 10.3390/membranes8040097.

[25] Y. J. Heo and S. J. Park, "A role of steam activation on CO_2 capture and separation of narrow microporous carbons produced from cellulose fibers," *Energy,* vol. 91, pp. 142-150, 2015, doi: 10.1016/j.energy.2015.08.033.

[26] R. Fleming, T. O. Candido, N. P. Granado, and L. C. Pardini, "Melt spinning of poly(acrylonitrile)-co-styrene copolymer," *Polymer Degradation and Stability,* vol. 192, pp. 109702-109702, 2021, doi: 10.1016/j.polymdegradstab.2021.109702.

[27] N. Byrne, R. De Silva, Y. Ma, H. Sixta, and M. Hummel, "Enhanced stabilization of cellulose-lignin hybrid filaments for carbon fiber production," *Cellulose,* vol. 25, no. 1, pp. 723-733, 2018, doi: 10.1007/s10570-017-1579-0.

[28] E. Frank, L. M. Steudle, D. Ingildeev, J. M. Spörl, and M. R. Buchmeiser, "Carbon fibers: Precursor systems, processing, structure, and properties," *Angewandte Chemie International Edition,* vol. 53, no. 21, pp. 5262-5298, 2014, doi: 10.1002/anie.201306129.

[29] N. Byrne *et al.*, "Cellulose-derived carbon fibers produced via a continuous carbonization process: Investigating precursor choice and carbonization conditions," *Macromolecular Chemistry and Physics,* vol. 217, no. 22, pp. 2517-2524, 2016, doi: 10.1002/macp.201600236.

[30] I. Karacan and A. Gül, "Carbonization behavior of oxidized viscose rayon fibers in the presence of boric acid–phosphoric acid impregnation," *Journal of Materials Science,* vol. 49, no. 21, pp. 7462-7475, 2014, doi: 10.1007/s10853-014-8451-5.

[31] M. Trogen *et al.*, "Cellulose-lignin composite fibres as precursors for carbon fibres. Part 1 – Manufacturing and properties of precursor fibres," *Carbohydrate Polymers,* vol. 252, no. September 2020, pp. 117133-117133, 2021, doi: 10.1016/j.carbpol.2020.117133.

[32] P. H. Brunner and P. V. Roberts, "The significance of heating rate on char yield and char properties in the pyrolysis of cellulose," *Carbon,* vol. 18, no. 3, pp. 217-224, 1980, doi: 10.1016/0008-6223(80)90064-0.

[33] I. Karacan and T. Soy, "Enhancement of oxidative stabilization of viscose rayon fibers impregnated with ammonium sulfate prior to carbonization

and activation steps," *Journal of Applied Polymer Science,* vol. 128, no. 2, pp. 1239-1249, 2013, doi: 10.1002/app.38496.

[34] M. Tang and R. Bacon, "Carbonization of cellulose fibers—I. Low temperature pyrolysis," *Carbon,* vol. 2, no. 3, pp. 211-220, 1964, doi: 10.1016/0008-6223(64)90035-1.

[35] F. Zeng and D. Pan, "The structural transitions of rayon under the promotion of a phosphate in the preparation of ACF," *Cellulose,* vol. 15, no. 1, pp. 91-99, 2008, doi: 10.1007/s10570-007-9148-6.

[36] A. Oroumei, B. Fox, and M. Naebe, "Thermal and rheological characteristics of biobased carbon fiber precursor derived from low molecular weight organosolv lignin," *ACS Sustainable Chemistry and Engineering,* vol. 3, no. 4, pp. 758-769, 2015, doi: 10.1021/acssuschemeng.5b00097.

[37] X. Zhang *et al.*, "Influence of Lignin units on the properties of Lignin/PAN -derived carbon fibers," *Journal of Applied Polymer Science,* vol. 137, no. 42, 2020, doi: 10.1002/app.49274.

[38] N.-D. Le, M. Trogen, Y. Ma, R. J. Varley, M. Hummel, and N. Byrne, "Cellulose-lignin composite fibers as precursors for carbon fibers: Part 2 – The impact of precursor properties on carbon fibers," *Carbohydrate Polymers,* vol. 250, no. August, pp. 116918-116918, 2020, doi: 10.1016/j.carbpol.2020.116918.

[39] B. C. Bai, J. S. Im, and Y. S. Lee, "Lyocell-based activated carbon fibers improved the adsorption of harmful gas properties when produced via dual-simultaneous treatments," *Carbon Letters,* vol. 23, no. 3, pp. 69-73, 2017, doi: 10.5714/CL.2017.23.069.

[40] D. M. Mitrano and W. Wohlleben, "Microplastic regulation should be more precise to incentivize both innovation and environmental safety," *Nature Communications,* vol. 11, no. 1, pp. 5324-5324, 2020, doi: 10.1038/s41467-020-19069-1.

[41] Y. Ma, M. Hummel, I. Kontro, and H. Sixta, "High performance man-made cellulosic fibres from recycled newsprint," *Green Chemistry,* vol. 20, no. 1, pp. 160-169, 2018, doi: 10.1039/C7GC02896B.

[42] R. K. Pachauri and L. A. Meyer, "IPCC, 2014: Climate Change 2014: Synthesis Report. Contribution of Working Groups I, II and III to the Fifth Assessment Report of the Intergovernmental Panel on Climate Change," Geneva, Switzerland, 2014.

[43] Y. Yuan, H. You, and L. Ricardez-Sandoval, "Recent advances on first-principles modeling for the design of materials in CO_2 capture

technologies," *Chinese Journal of Chemical Engineering,* vol. 27, no. 7, pp. 1554-1565, 2019, doi: 10.1016/j.cjche.2018.10.017.

[44] Y. Zhang *et al.*, "Recent advances in lithium containing ceramic based sorbents for high-temperature CO_2 capture," *Journal of Materials Chemistry A,* vol. 7, no. 14, pp. 7962-8005, 2019, doi: 10.1039/c8ta08932a.

[45] J. E. Koresh and A. Sofer, "Molecular sieve carbon permselective membrane. Part I. Presentation of a new device for gas mixture separation," *Separation Science and Technology,* vol. 18, no. 8, pp. 723-734, 2006, doi: 10.1080/01496398308068576.

[46] H. Marsh and F. Rodríguez-Reinoso, *Activated Carbon*. Elsevier, 2006.

[47] I. S. Ismail, N. A. Rashidi, and S. Yusup, "Production and characterization of bamboo-based activated carbon through single-step H_3PO_4 activation for CO_2 capture," *Environmental Science and Pollution Research,* 2021, doi: 10.1007/s11356-021-15030-x.

[48] "Ioncell." https://ioncell.fi/ (accessed 10 October 2021).

[49] S. Asaadi, M. Hummel, P. Ahvenainen, M. Gubitosi, U. Olsson, and H. Sixta, "Structural analysis of Ioncell-F fibres from birch wood," *Carbohydrate Polymers,* vol. 181, no. September 2017, pp. 893-901, 2018, doi: 10.1016/j.carbpol.2017.11.062.

[50] Y. Ma *et al.*, "High-strength composite fibers from cellulose-lignin blends regenerated from ionic liquid solution," *ChemSusChem,* vol. 8, no. 23, pp. 4030-4039, 2015, doi: 10.1002/cssc.201501094.

[51] A. Michud *et al.*, "Ioncell-F: ionic liquid-based cellulosic textile fibers as an alternative to viscose and Lyocell," *Textile Research Journal,* vol. 86, no. 5, pp. 543-552, 2016, doi: 10.1177/0040517515591774.

[52] H. Sixta *et al.*, "Ioncell-F: A high-strength regenerated cellulose fibre," *Nordic Pulp and Paper Research Journal,* vol. 30, no. 1, pp. 43-57, 2015, doi: 10.3183/npprj-2015-30-01-p043-057.

[53] C. Felgueiras, N. G. Azoia, C. Gonçalves, M. Gama, and F. Dourado, "Trends on the cellulose-based textiles: Raw materials and technologies," *Frontiers in Bioengineering and Biotechnology,* vol. 9, no. March, pp. 1-20, 2021, doi: 10.3389/fbioe.2021.608826.

[54] S. Elsayed, M. Hummel, D. Sawada, C. Guizani, M. Rissanen, and H. Sixta, "Superbase-based protic ionic liquids for cellulose filament spinning," *Cellulose,* vol. 28, no. 1, pp. 533-547, 2021, doi: 10.1007/s10570-020-03505-y.

[55] R. Bacon and M. Tang, "Carbonization of cellulose fibers—II. Physical property study," *Carbon,* vol. 2, no. 3, pp. 221-225, 1964, doi: 10.1016/0008-6223(64)90036-3.

[56] A. G. W. Bradbury, Y. Sakai, and F. Shafizadeh, "A kinetic model for pyrolysis of cellulose," *Journal of Applied Polymer Science,* vol. 23, no. 11, pp. 3271-3280, 1979, doi: 10.1002/app.1979.070231112.

[57] S. Matsuoka, H. Kawamoto, and S. Saka, "What is active cellulose in pyrolysis? An approach based on reactivity of cellulose reducing end," *Journal of Analytical and Applied Pyrolysis,* vol. 106, pp. 138-146, 2014, doi: 10.1016/j.jaap.2014.01.011.

[58] A. Tomczyk, Z. Sokołowska, and P. Boguta, "Biochar physicochemical properties: pyrolysis temperature and feedstock kind effects," *Reviews in Environmental Science and Bio/Technology,* vol. 19, no. 1, pp. 191-215, 2020, doi: 10.1007/s11157-020-09523-3.

[59] R. Scholz *et al.*, "Improvements in the carbonisation of viscose fibres," *Reinforced Plastics,* vol. 63, no. 3, pp. 146-150, 2019, doi: 10.1016/j.repl.2018.10.002.

[60] P. I. Zolkin, E. G. Cheblakova, K. I. Aberyakhimov, and V. F. Tatarinov, "Development of biocompatible carbon fibers from hydrated cellulose for the treatment of glaucoma," *Solid Fuel Chemistry,* vol. 45, no. 5, pp. 359-362, 2011, doi: 10.3103/S0361521911050144.

[61] N.-D. Le, M. Trogen, R. J. Varley, M. Hummel, and N. Byrne, "Chemically accelerated stabilization of a cellulose–lignin precursor as a route to high yield carbon fiber production," *Biomacromolecules,* 2022, doi: 10.1021/acs.biomac.1c01226.

[62] B. C. Bai *et al.*, "Improved flame-retardant properties of lyocell fiber achieved by phosphorus compound," *Materials Letters,* vol. 135, pp. 226-228, 2014, doi: 10.1016/j.matlet.2014.07.131.

[63] I. Karacan and T. Soy, "Investigation of structural transformations taking place during oxidative stabilization of viscose rayon precursor fibers prior to carbonization and activation," *Journal of Molecular Structure,* vol. 1041, pp. 29-38, 2013, doi: 10.1016/j.molstruc.2013.02.040.

[64] W. Chen, F. He, S. Zhang, H. Xv, and Z. Xv, "Development of porosity and surface chemistry of textile waste jute-based activated carbon by physical activation," *Environmental Science and Pollution Research,* vol. 25, no. 10, pp. 9840-9848, 2018, doi: 10.1007/s11356-018-1335-5.

[65] I. Karacan and T. Soy, "Structure and properties of oxidatively stabilized viscose rayon fibers impregnated with boric acid and phosphoric acid prior

to carbonization and activation steps," *Journal of Materials Science,* vol. 48, no. 5, pp. 2009-2021, 2013, doi: 10.1007/s10853-012-6970-5.

[66] J. A. Okolie, S. Nanda, A. K. Dalai, and J. A. Kozinski, "Chemistry and specialty industrial applications of lignocellulosic biomass," *Waste and Biomass Valorization,* vol. 12, no. 5, pp. 2145-2169, 2021, doi: 10.1007/s12649-020-01123-0.

[67] K. Babel, "Porous structure evolution of cellulose carbon fibres during oxidation in carbon dioxide," *Adsorption Science and Technology,* vol. 21, no. 4, pp. 363-371, 2003, doi: 10.1260/026361703322405079.

[68] C. Moreno-Castilla, M. V. López-Ramón, and F. Carrasco-Marín, "Changes in surface chemistry of activated carbons by wet oxidation," *Carbon,* vol. 38, no. 14, pp. 1995-2001, 2000, doi: 10.1016/S0008-6223(00)00048-8.

[69] X. f. Tan *et al.*, "Biochar as potential sustainable precursors for activated carbon production: Multiple applications in environmental protection and energy storage," *Bioresource Technology,* vol. 227, pp. 359-372, 2017, doi: 10.1016/j.biortech.2016.12.083.

[70] P. Lahijani, Z. A. Zainal, M. Mohammadi, and A. R. Mohamed, "Conversion of the greenhouse gas CO_2 to the fuel gas CO via the Boudouard reaction: A review," *Renewable and Sustainable Energy Reviews,* vol. 41, pp. 615-632, 2015, doi: 10.1016/j.rser.2014.08.034.

[71] J. Huang *et al.*, "Enhanced conversion of CO_2 into O_2-free fuel gas via the Boudouard reaction with biochar in an atmospheric plasmatron," *Journal of CO_2 Utilization,* vol. 45, no. December 2020, 2021, doi: 10.1016/j.jcou.2020.101429.

[72] K. Babel and K. Jurewicz, "Electrical capacitance of fibrous carbon composites in supercapacitors," *Fuel Processing Technology,* vol. 77-78, pp. 181-189, 2002, doi: 10.1016/S0378-3820(02)00070-X.

[73] S. Bhati, J. S. Mahur, S. Dixit, and O. N. Choubey, "Surface and adsorption properties of activated carbon fabric prepared from cellulosic polymer: Mixed activation method," *Bulletin of the Korean Chemical Society,* vol. 34, no. 2, pp. 569-573, 2013, doi: 10.5012/bkcs.2013.34.2.645.

[74] J. P. Castro *et al.*, "Activated carbons prepared by physical activation from different pretreatments of amazon piassava fibers," *Journal of Natural Fibers,* vol. 16, no. 7, pp. 961-976, 2019, doi: 10.1080/15440478.2018.1442280.

[75] J. Zheng, Q. Zhao, and Z. Ye, "Preparation and characterization of activated carbon fiber (ACF) from cotton woven waste," *Applied Surface Science,* vol. 299, pp. 86-91, 2014, doi: 10.1016/j.apsusc.2014.01.190.

[76] R. Farma, A. Putri, E. Taer, A. Awitdrus, and A. Apriwandi, "Synthesis of highly porous activated carbon nanofibers derived from bamboo waste materials for application in supercapacitor," *Journal of Materials Science: Materials in Electronics,* vol. 32, no. 6, pp. 7681-7691, 2021, doi: 10.1007/s10854-021-05486-5.

[77] M. Fujishige, I. Yoshida, Y. Toya, Y. Banba, and K.-i. Oshida, "Journal of Environmental Chemical Engineering Preparation of activated carbon from bamboo-cellulose fi ber and its use for EDLC electrode material," *Biochemical Pharmacology,* vol. 5, no. 2, pp. 1801-1808, 2017, doi: 10.1016/j.jece.2017.03.011.

[78] C. Wei, J. Yu, X. Yang, and G. Zhang, "Activated Carbon Fibers with Hierarchical Nanostructure Derived from Waste Cotton Gloves as High-Performance Electrodes for Supercapacitors," 2017, doi: 10.1186/s11671-017-2151-4.

[79] H. Shi, "Activated carbons and double layer capacitance," *Electrochimica Acta,* vol. 41, no. 10, pp. 1633-1639, 1996, doi: 10.1016/0013-4686(95)00416-5.

[80] R. Ahmadi, M. Ardjmand, A. Rashidi, and M. Rafizadeh, "High performance novel nanoadsorbents derived - natural cellulose fibers for superior CO_2 adsorption and CO_2 / CH_4 separation," *Energy Sources, Part A: Recovery, Utilization and Environmental Effects,* vol. 00, no. 00, pp. 1-19, 2020, doi: 10.1080/15567036.2020.1845878.

[81] B. C. Bai, E. A. Kim, C. W. Lee, Y.-S. Lee, and J. S. Im, "Effects of surface chemical properties of activated carbon fibers modified by liquid oxidation for CO_2 adsorption," *Applied Surface Science,* vol. 353, pp. 158-164, 2015, doi: 10.1016/j.apsusc.2015.06.046.

[82] T. Y. Han, S. K. Park, and J. S. Lee, "Ammonia activation of carbonized polysaccharides and their application for the carbon capture," *Bulletin of the Korean Chemical Society,* vol. 37, no. 5, pp. 689-694, 2016, doi: 10.1002/bkcs.10755.

[83] A. Houshmand *et al.*, "Exploring potential methods for anchoring amine groups on the surface of activated carbon for CO_2 adsorption," vol. 6395, no. May, 2011, doi: 10.1080/01496395.2010.546383.

[84] B. C. Bai, Y.-S. Lee, and J. S. Im, "Activated carbon fibers for toxic gas removal based on electrical investigation: Mechanistic study of p-type/n-type junction structures," *Scientific Reports,* vol. 9, no. 1, pp. 14458-14458, 2019, doi: 10.1038/s41598-019-50707-x.

[85] E. Taer, F. Febriyanti, W. S. Mustika, R. Taslim, A. Agustino, and A. Apriwandi, "Enhancing the performance of supercapacitor electrode from

chemical activation of carbon nanofibers derived Areca catechu husk via one-stage integrated pyrolysis," *Carbon Letters,* vol. 31, no. 4, pp. 601-612, 2020, doi: 10.1007/s42823-020-00191-5.

[86] S. Brunauer, P. H. Emmett, and E. Teller, "Adsorption of gases in multimolecular layers," *Journal of the American Chemical Society,* vol. 60, no. 2, pp. 309-319, 1938, doi: 10.1021/ja01269a023.

[87] R. Z. Lazic, *Design of Experiments in Chemical Engineering*. Weinheim: WILEY-VCH Verlag GmbH & Co, 2004.

[88] R. A. Fisher, *The Design of Experiments*, 2nd ed. Hafner Press, 1935.

[89] S. Greenhill, S. Rana, S. Gupta, P. Vellanki, and S. Venkatesh, "Bayesian optimization for adaptive experimental design: A review," *IEEE Access,* vol. 8, pp. 13937-13948, 2020, doi: 10.1109/access.2020.2966228.

[90] R. G. Brereton, *Chemometrics: data driven extraction for science*, 2nd ed. John Wiley & Sons, 2018.

[91] T. Ueno, T. D. Rhone, Z. Hou, T. Mizoguchi, and K. Tsuda, "COMBO: An efficient Bayesian optimization library for materials science," *Materials Discovery,* vol. 4, pp. 18-21, 2016, doi: 10.1016/j.md.2016.04.001.

[92] Y. Zhang, D. W. Apley, and W. Chen, "Bayesian optimization for materials design with mixed quantitative and qualitative variables," *Scientific Reports,* vol. 10, no. 1, 2020, doi: 10.1038/s41598-020-60652-9.

[93] W. Wang, Y. Cheng, and G. Tan, "Design optimization of SBS-modified asphalt mixture reinforced with eco-friendly basalt fiber based on response surface methodology," *Materials,* vol. 11, no. 8, 2018, doi: 10.3390/ma11081311.

[94] M. Balachandran, S. Devanathan, R. Muraleekrishnan, and S. S. Bhagawan, "Optimizing properties of nanoclay–nitrile rubber (NBR) composites using Face Centred Central Composite Design," *Materials & Design,* vol. 35, pp. 854-862, 2012, doi: 10.1016/j.matdes.2011.03.077.

[95] R. Eslami-Farsani, "Modeling and optimization of carbon fiber processing: A RSM-FCCC experimental design approach," *Journal of Macromolecular Science, Part A,* vol. 52, no. 1, pp. 69-75, 2014, doi: 10.1080/10601325.2014.976756.

[96] S. Breitenbach *et al.*, "Viscose-based porous carbon fibers: improving yield and porosity through optimization of the carbonization process by design of experiment," *Journal of Porous Materials,* vol. 28, no. 3, pp. 727-739, 2021, doi: 10.1007/s10934-020-01026-4.

[97] N. Doufene, T. Berrama, D. Tahtat, S. Benredouane, and C. Nekaa, "Combination of two experimental designs to optimize the dimethylphthalate elimination on activated carbon elaborated from arundo donax," *Arabian Journal for Science and Engineering,* vol. 44, no. 6, pp. 5275-5287, 2018, doi: 10.1007/s13369-018-3531-5.

[98] K. Dunn, *Process Improvement Using Data*. 2018.

[99] L. Pitkänen and H. Sixta, "Size-exclusion chromatography of cellulose: observations on the low-molar-mass fraction," *Cellulose,* vol. 27, no. 16, pp. 9217-9225, 2020, doi: 10.1007/s10570-020-03419-9.

[100] K. Hina, H. Zou, W. Qian, D. Zuo, and C. Yi, "Preparation and performance comparison of cellulose-based activated carbon fibres," *Cellulose,* vol. 25, no. 1, pp. 607-617, 2017, doi: 10.1007/s10570-017-1560-y.

[101] P. Iacomi and P. L. Llewellyn, "pyGAPS: a Python-based framework for adsorption isotherm processing and material characterisation," *Adsorption,* vol. 25, no. 8, pp. 1533-1542, 2019, doi: 10.1007/s10450-019-00168-5.

[102] J. Osterrieth *et al.*, *How reproducible are surface areas calculated from the BET equation?,* 2021, doi: 10.26434/chemrxiv.14291644.v2.

[103] J. Rouquerol *et al.*, "Recommendations for the characterization of porous solids (Technical Report)," *Pure and Applied Chemistry,* vol. 66, no. 8, pp. 1739-1758, 1994, doi: 10.1351/pac199466081739.

[104] O. Beyssac, B. Goffé, J.-P. Petitet, E. Froigneux, M. Moreau, and J.-N. Rouzaud, "On the characterization of disordered and heterogeneous carbonaceous materials by Raman spectroscopy," *Spectrochimica Acta Part A: Molecular and Biomolecular Spectroscopy,* vol. 59, no. 10, pp. 2267-2276, 2003, doi: 10.1016/s1386-1425(03)00070-2.

[105] A. Sadezky, H. Muckenhuber, H. Grothe, R. Niessner, and U. Pöschl, "Raman microspectroscopy of soot and related carbonaceous materials: Spectral analysis and structural information," *Carbon,* vol. 43, no. 8, pp. 1731-1742, 2005, doi: 10.1016/j.carbon.2005.02.018.

[106] P. K. Mubari, T. Beguerie, M. Monthioux, E. Weiss-Hortala, A. Nzihou, and P. Puech, "The X-ray, Raman and TEM signatures of cellulose-derived carbons explained," *C,* vol. 8, no. 1, 2022, doi: 10.3390/c8010004.

[107] E. Crespo, F. J. Luque, J. F. Barrenechea, and M. Rodas, "Influence of grinding on graphite crystallinity from experimental and natural data: implications for graphite thermometry and sample preparation," *Mineralogical Magazine,* vol. 70, no. 6, pp. 697-707, 2018, doi: 10.1180/0026461067060358.

[108] P. Mallet-Ladeira *et al.*, "A Raman study to obtain crystallite size of carbon materials: A better alternative to the Tuinstra–Koenig law," *Carbon,* vol. 80, pp. 629-639, 2014, doi: 10.1016/j.carbon.2014.09.006.

[109] P. Mallet-Ladeira, P. Puech, P. Weisbecker, G. L. Vignoles, and M. Monthioux, "Behavior of Raman D band for pyrocarbons with crystallite size in the 2–5 nm range," *Applied Physics A,* vol. 114, no. 3, pp. 759-763, 2013, doi: 10.1007/s00339-013-7671-x.

[110] A. C. Ferrari and J. Robertson, "Interpretation of Raman spectra of disordered and amorphous carbon," *Physical Review B,* vol. 61, no. 20, pp. 14095-14107, 2000, doi: 10.1103/PhysRevB.61.14095.

[111] L. G. Cançado, A. Jorio, and M. A. Pimenta, "Measuring the absolute Raman cross section of nanographites as a function of laser energy and crystallite size," *Physical Review B,* vol. 76, no. 6, 2007, doi: 10.1103/PhysRevB.76.064304.

[112] D. O. Ojwang, J. Grins, and G. Svensson, "The adsorption kinetics of CO_2 on copper hexacyanoferrate studied by thermogravimetric analysis," *Microporous and Mesoporous Materials,* vol. 272, pp. 70-78, 2018, doi: 10.1016/j.micromeso.2018.06.019.

[113] J. Rampersad, J. Osterrieth, and N. Rampal. "BET surface identification - a program that fully implements the Rouquerol criteria." 30 Jan. https://github.com/nakulrampal/betsi-gui (accessed 2022).

[114] M. Thommes *et al.*, "Physisorption of gases, with special reference to the evaluation of surface area and pore size distribution (IUPAC Technical Report)," *Pure and Applied Chemistry,* vol. 87, no. 9-10, pp. 1051-1069, 2015, doi: 10.1515/pac-2014-1117.

[115] J. Garrido, A. Linares-Solano, J. M. Martin-Martinez, M. Molina-Sabio, F. Rodriguez-Reinoso, and R. Torregrosa, "Use of nitrogen vs. carbon dioxide in the characterization of activated carbons," *Langmuir,* vol. 3, no. 1, pp. 76-81, 2002, doi: 10.1021/la00073a013.

[116] A. Aleghafouri, M. Mohsen-Nia, A. Mohajeri, M. Mahdyarfar, and M. Asghari, "Micropore size analysis of activated carbons using nitrogen, carbon dioxide and methane adsorption isotherms: Experimental and theoretical studies," *Adsorption Science & Technology,* vol. 30, no. 4, pp. 307-316, 2012, doi: 10.1260/0263-6174.30.4.307.

[117] M. M. Almoneef, H. Jedli, and M. Mbarek, "Experimental study of CO_2 adsorption using activated carbon," *Materials Research Express,* vol. 8, no. 6, 2021, doi: 10.1088/2053-1591/ac05fe.

[118] K. Weber and P. Quicker, "Properties of biochar," *Fuel,* vol. 217, pp. 240-261, 2018, doi: 10.1016/j.fuel.2017.12.054.

[119] A. Oberlin, "Carbonization and graphitization," *Carbon,* vol. 22, no. 6, pp. 521-541, 1984, doi: 10.1016/0008-6223(84)90086-1.

[120] M. W. Smith *et al.*, "Structural analysis of char by Raman spectroscopy: Improving band assignments through computational calculations from first principles," *Carbon,* vol. 100, pp. 678-692, 2016, doi: 10.1016/j.carbon.2016.01.031.

[121] H. Wu, R. Gakhar, A. Chen, S. Lam, C. P. Marshall, and R. O. Scarlat, "Comparative analysis of microstructure and reactive sites for nuclear graphite IG-110 and graphite matrix A3," *Journal of Nuclear Materials,* vol. 528, 2020, doi: 10.1016/j.jnucmat.2019.151802.

[122] D. G. McCulloch, S. Prawer, and A. Hoffman, "Structural investigation of xenon-ion-beam-irradiated glassy carbon," *Physical Review B,* vol. 50, no. 9, pp. 5905-5917, 1994, doi: 10.1103/PhysRevB.50.5905.

[123] K. A. Cychosz and M. Thommes, "Progress in the Physisorption Characterization of Nanoporous Gas Storage Materials," *Engineering,* vol. 4, no. 4, pp. 559-566, 2018, doi: 10.1016/j.eng.2018.06.001.

[124] M. Sevilla, P. Valle-Vigón, and A. B. Fuertes, "N-doped polypyrrole-based porous carbons for CO_2 capture," *Advanced Functional Materials,* vol. 21, no. 14, pp. 2781-2787, 2011, doi: 10.1002/adfm.201100291.

[125] H. Wu, C. G. Thibault, H. Wang, K. A. Cychosz, M. Thommes, and J. Li, "Effect of temperature on hydrogen and carbon dioxide adsorption hysteresis in an ultramicroporous MOF," *Microporous and Mesoporous Materials,* vol. 219, pp. 186-189, 2016, doi: 10.1016/j.micromeso.2015.08.005.

[126] H. Freundlich, "Über die Adsorption in Lösungen," *Zeitschrift fur Physikalische Chemie,* vol. 57, pp. 385-470, 1906.

[127] M. Jaroniec, "Adsorption on heterogeneous surfaces: The exponential equation for the overall adsorption isotherm," *Surface Science,* vol. 50, no. 2, pp. 553-564, 1975, doi: 10.1016/0039-6028(75)90044-8.

[128] B. Ashourirad, P. Arab, T. Islamoglu, K. A. Cychosz, M. Thommes, and H. M. El-Kaderi, "A cost-effective synthesis of heteroatom-doped porous carbons as efficient CO_2 sorbents," *Journal of Materials Chemistry A,* vol. 4, no. 38, pp. 14693-14702, 2016, doi: 10.1039/c6ta06251b.

[129] A. Torrisi, C. Mellot-Draznieks, and R. G. Bell, "Impact of ligands on CO_2 adsorption in metal-organic frameworks: First principles study of the interaction of CO_2 with functionalized benzenes. II. Effect of polar and acidic substituents," *The Journal of Chemical Physics,* vol. 132, no. 4, 2010, doi: 10.1063/1.3276105.

[130] H. Li *et al.*, "Carbohydrate based hyper-crosslinked organic polymers with –OH functional groups for CO_2 separation," *Journal of Materials Chemistry A,* vol. 3, no. 42, pp. 20913-20918, 2015, doi: 10.1039/c5ta03213j.

[131] S.-H. Jia, X. Ding, H.-T. Yu, and B.-H. Han, "Multi-hydroxyl-containing porous organic polymers based on phenol formaldehyde resin chemistry with high carbon dioxide capture capacity," *RSC Advances,* vol. 5, no. 87, pp. 71095-71101, 2015, doi: 10.1039/c5ra13405f.

[132] Y. Liu and J. Wilcox, "Effects of Surface Heterogeneity on the Adsorption of CO_2 in Microporous Carbons," *Environmental Science & Technology,* vol. 46, no. 3, pp. 1940-1947, 2012, doi: 10.1021/es204071g.

A. Size Exclusion Chromatography of Ioncell

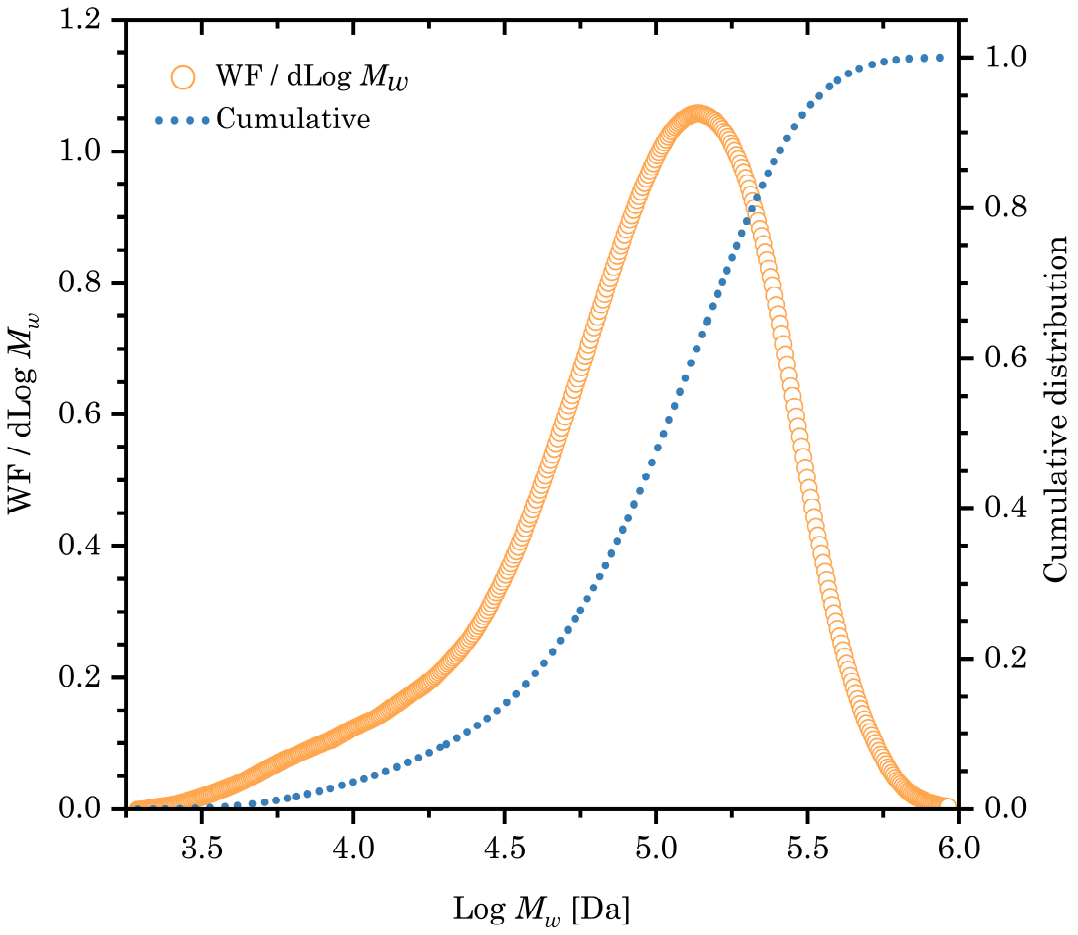

Appendix A Size exclusion chromatography of Ioncell fiber E100. For the analysis, cellulose was dissolved and analyzed following the same procedure described by Pitkänen and Sixta [99], but using 9.0% LiCl in DMAc instead of 0.9%.

B. Scanning Electron Microscopy

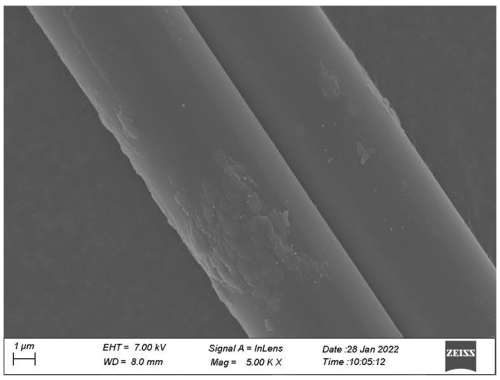

N1

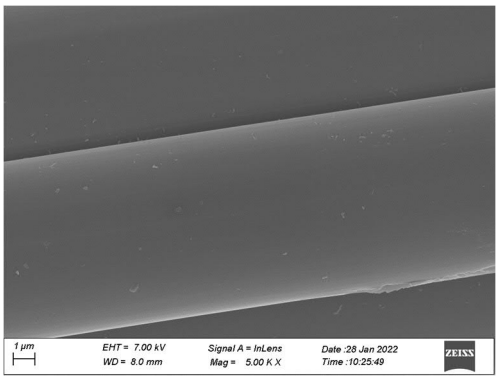

N2

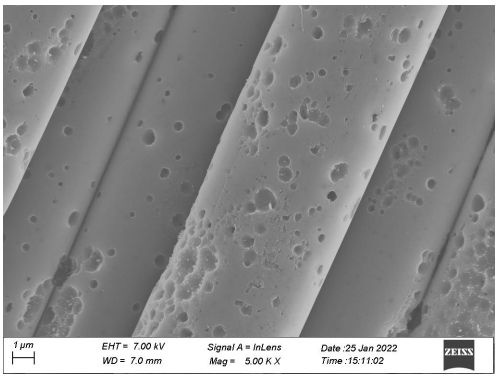

N3

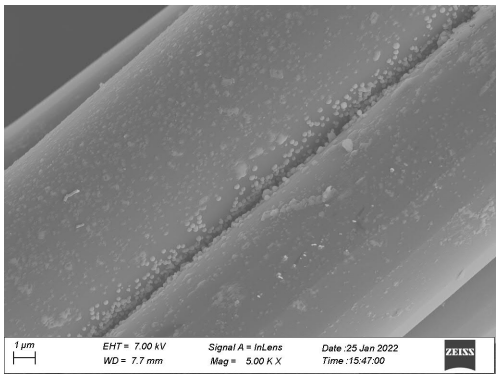

N4

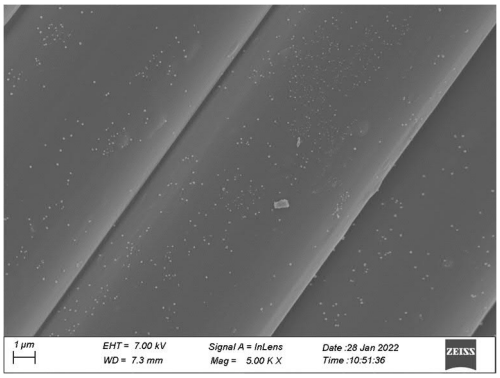

N5

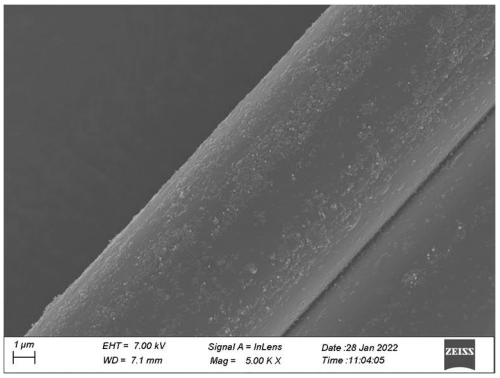

N6

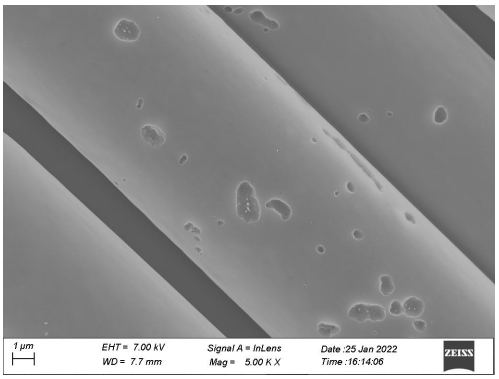

N7

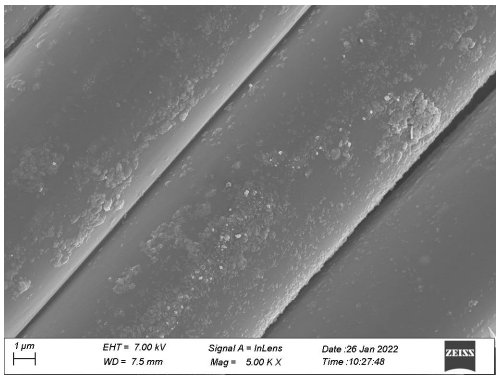

N8

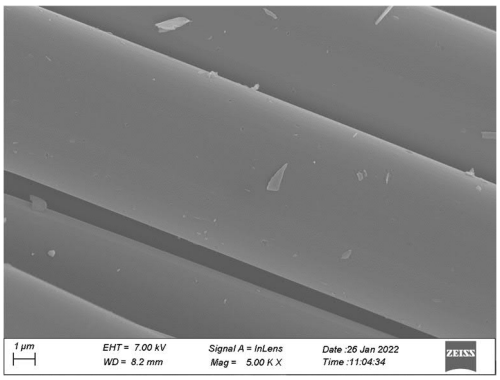

N9

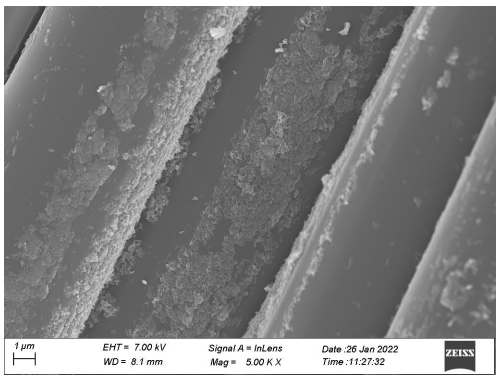

N10

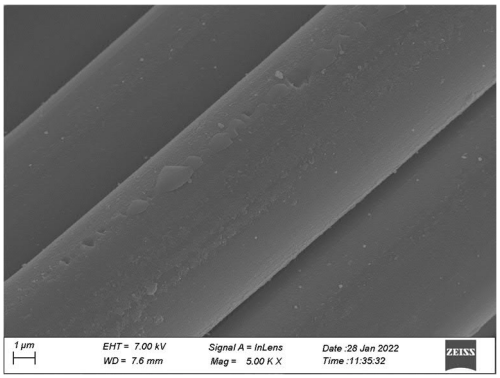

N11

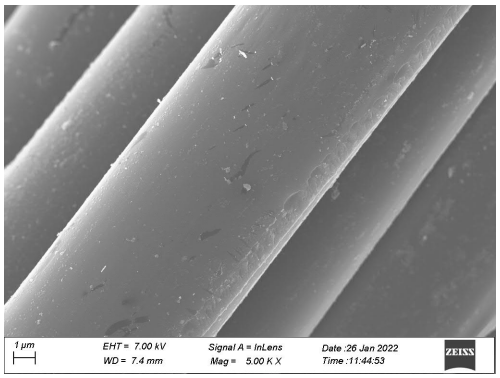

N12

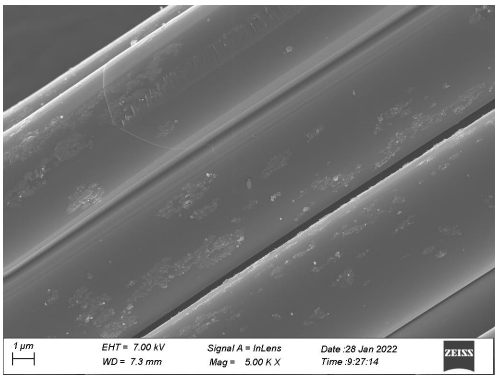

N13

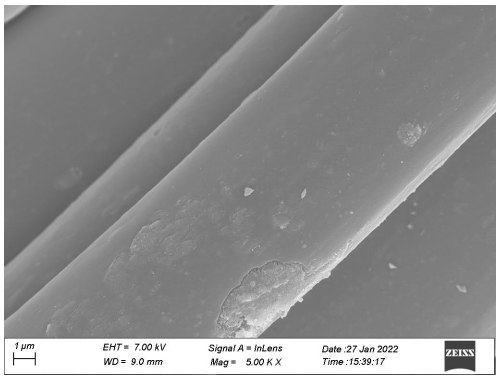

N14

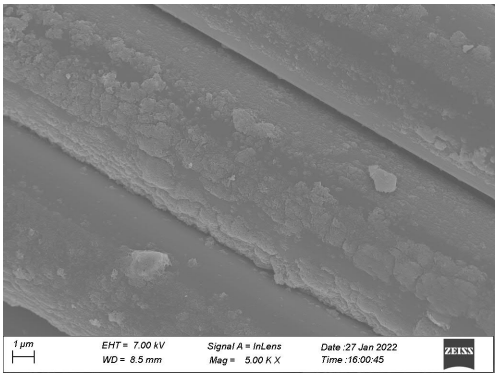

N15

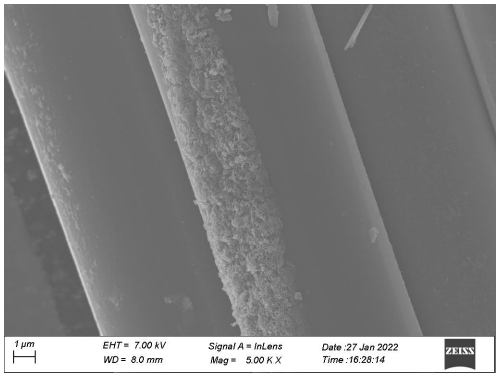

N16

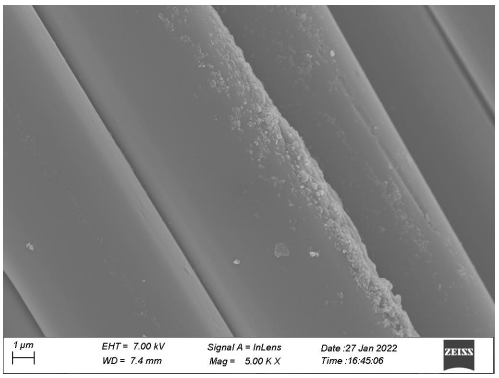

N17

Appendix B Scanning Electron Microscope images obtained from the samples composing the Face-centered Central composite Design.

C. BET plots, Rouquerol criteria, and t- plots

N3

a)

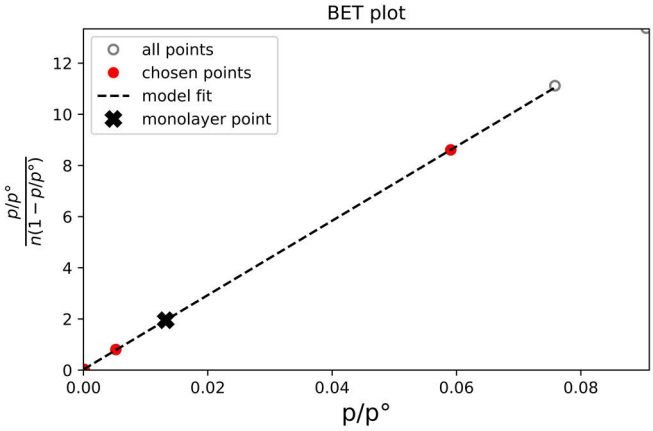

b)

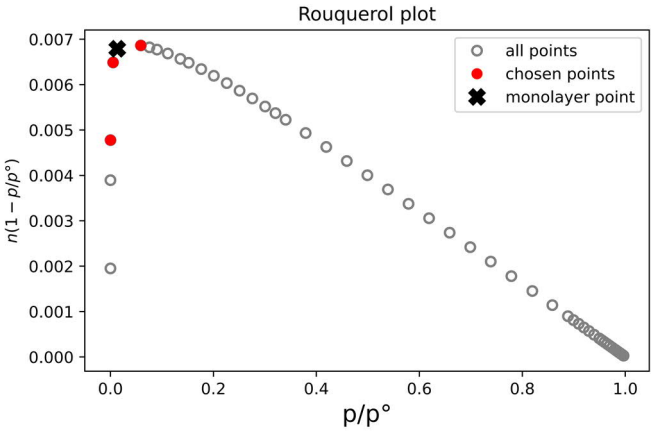

c)

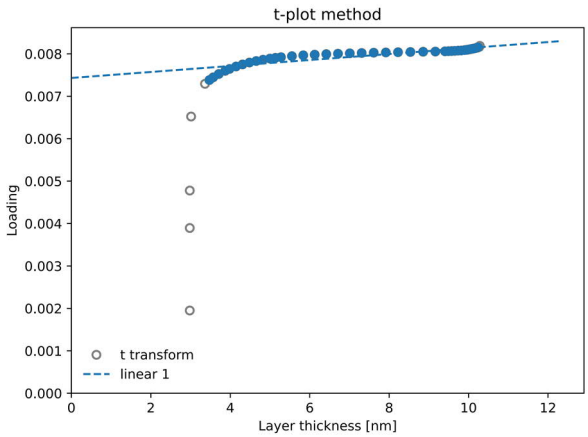

N4

a)

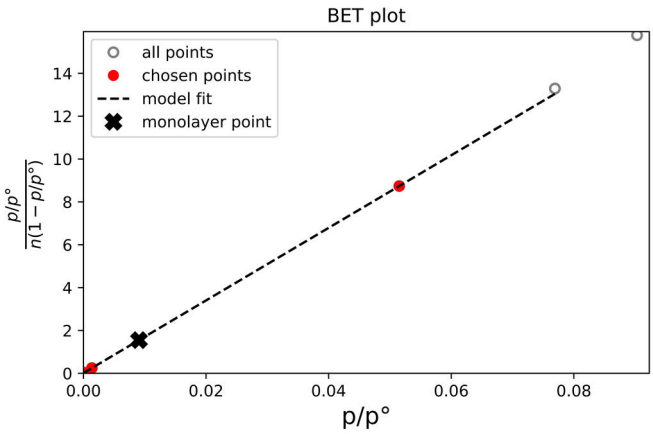
BET plot
all points
chosen points
model fit
monolayer point
$\frac{p/p°}{n(1-p/p°)}$
p/p°

b)

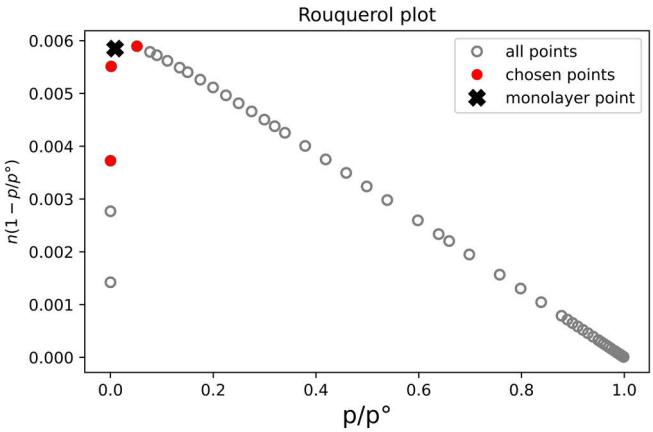
Rouquerol plot
all points
chosen points
monolayer point
$n(1-p/p°)$
p/p°

c)

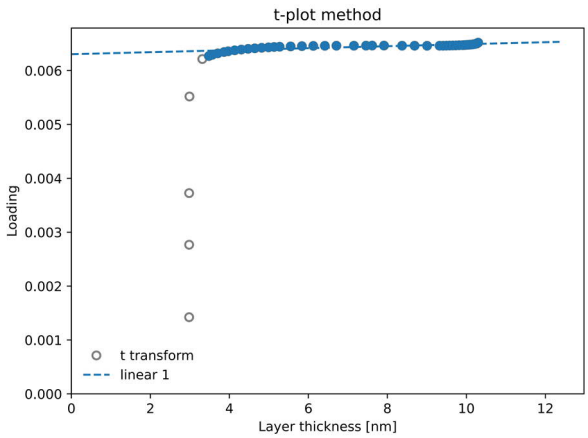
t-plot method
Loading
t transform
linear 1
Layer thickness [nm]

N7

a)

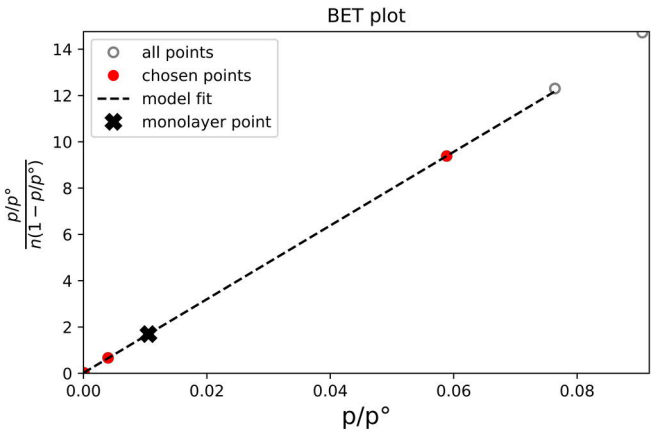
BET plot
all points
chosen points
model fit
monolayer point
$\frac{p/p°}{n(1-p/p°)}$
p/p°

b)

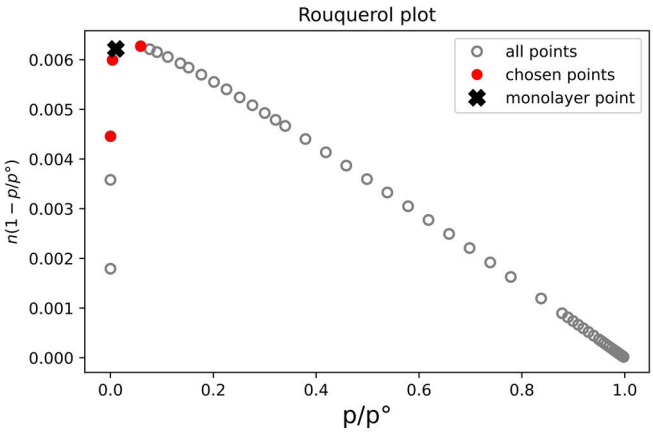
Rouquerol plot
all points
chosen points
monolayer point
$n(1-p/p°)$
p/p°

c)

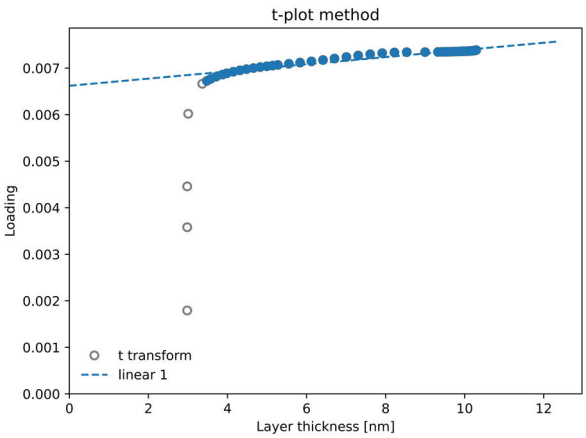
t-plot method
Loading
t transform
linear 1
Layer thickness [nm]

a)

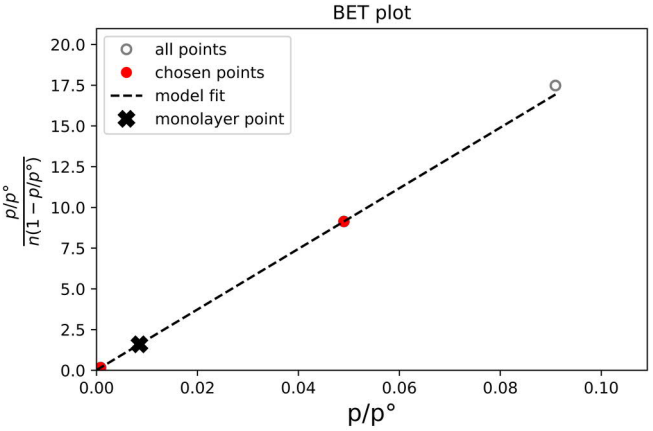
BET plot
all points
chosen points
model fit
monolayer point
$\frac{p/p°}{n(1-p/p°)}$
p/p°

b)

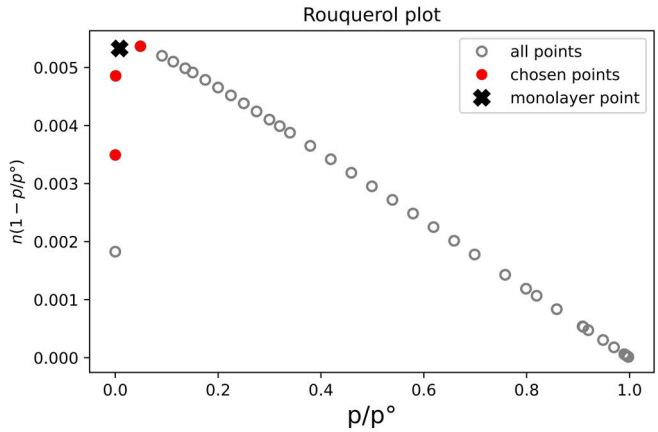
Rouquerol plot
all points
chosen points
monolayer point
$n(1-p/p°)$
p/p°

9

c)

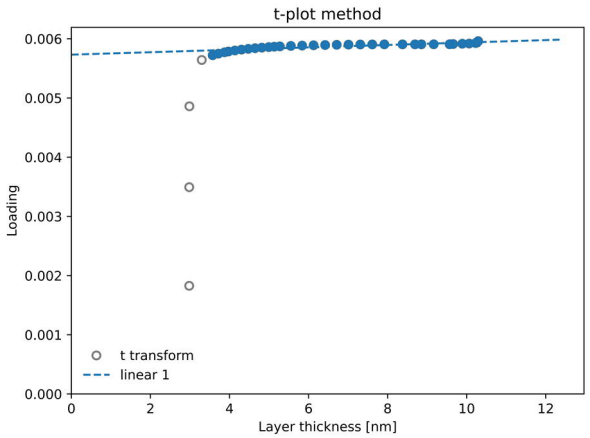
t-plot method
t transform
linear 1
Loading
Layer thickness [nm]

N9

a)

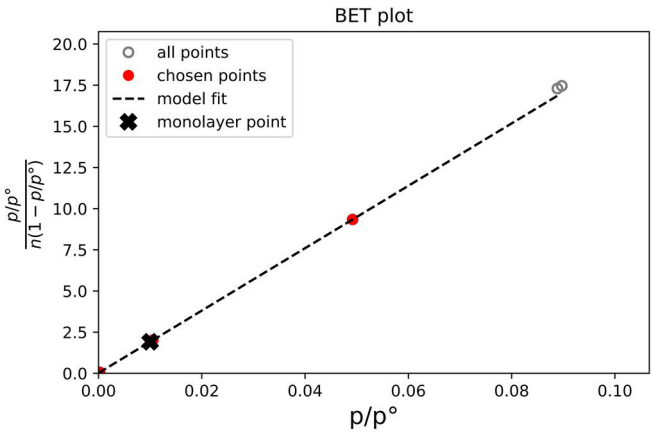
BET plot
all points
chosen points
model fit
monolayer point
$\frac{p/p°}{n(1-p/p°)}$
p/p°

b)

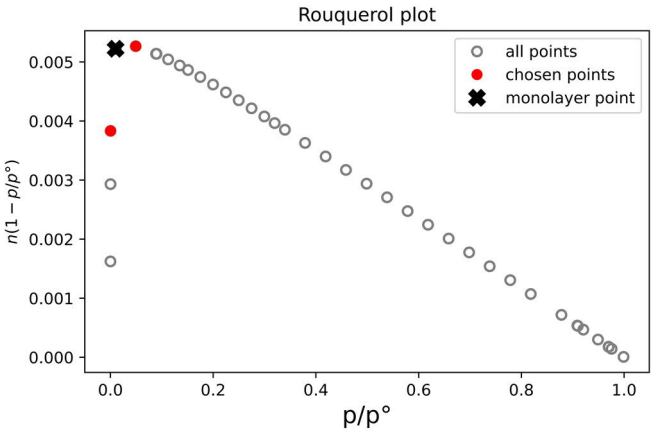
Rouquerol plot
all points
chosen points
monolayer point
$n(1-p/p°)$
p/p°

c)

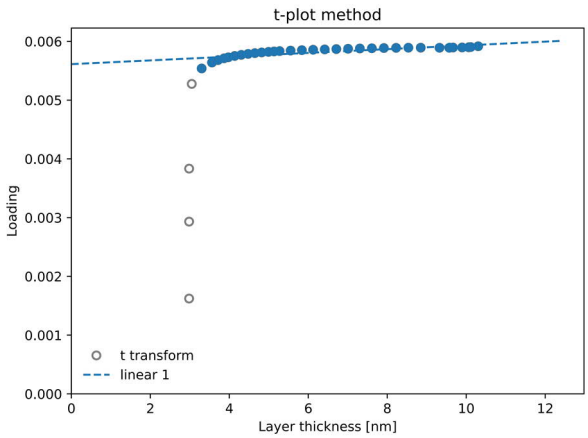
t-plot method
Loading
t transform
linear 1
Layer thickness [nm]

N10

a)

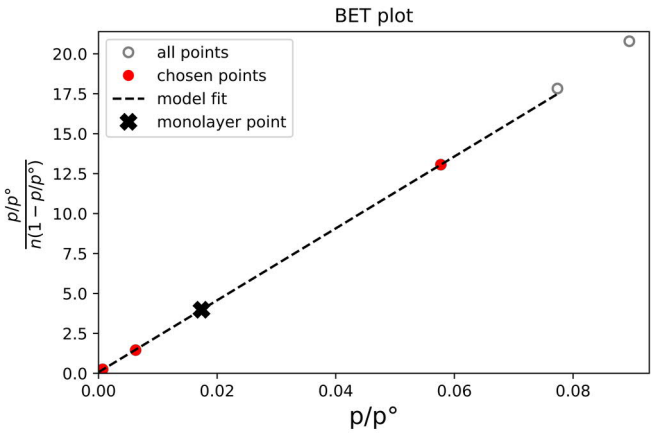
BET plot
all points
chosen points
model fit
monolayer point
$\frac{p/p°}{n(1-p/p°)}$
p/p°

b)

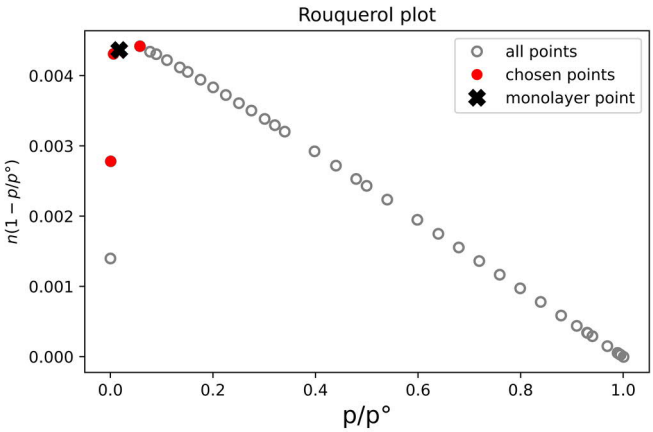
Rouquerol plot
all points
chosen points
monolayer point
$n(1-p/p°)$
p/p°

c)

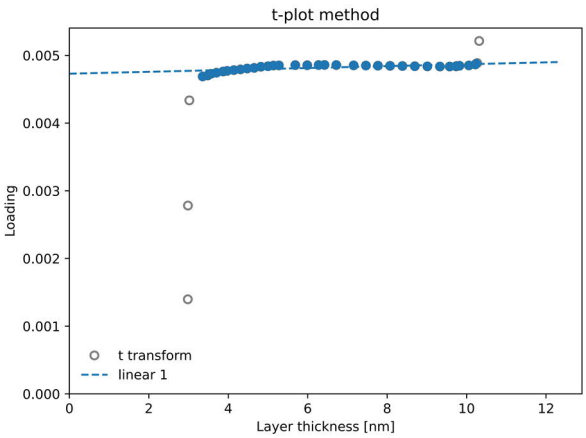
t-plot method
Loading
t transform
linear 1
Layer thickness [nm]

N12

a)

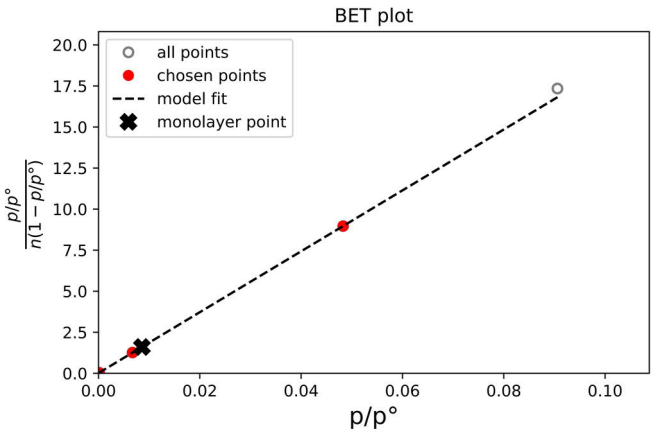
BET plot
all points
chosen points
model fit
monolayer point
$\frac{p/p°}{n(1-p/p°)}$
p/p°

b)

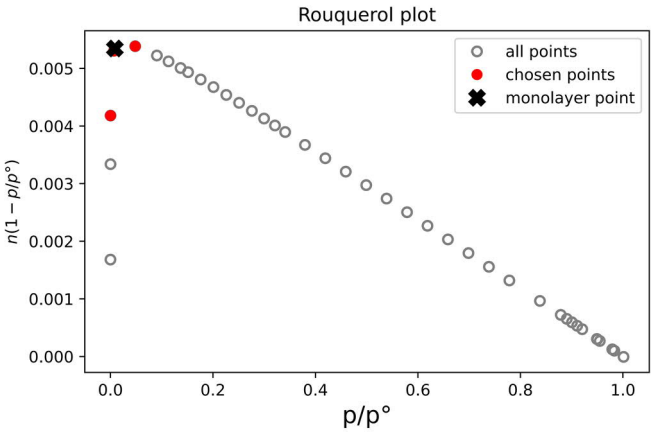
Rouquerol plot
all points
chosen points
monolayer point
$n(1-p/p°)$
p/p°

c)

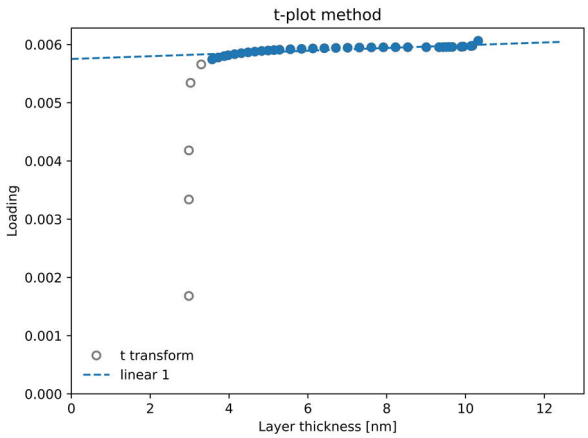
t-plot method
Loading
t transform
linear 1
Layer thickness [nm]

N13

a)

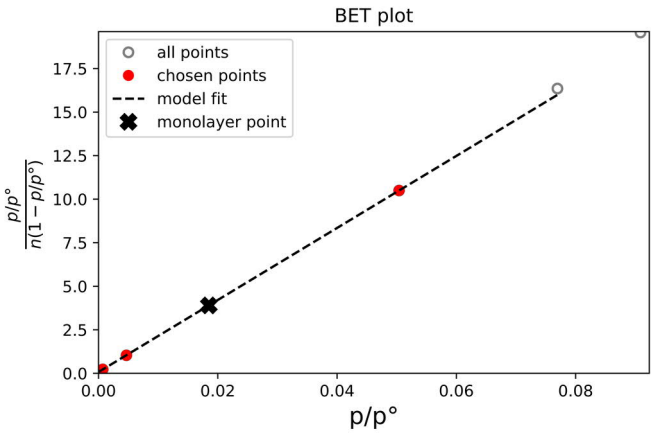
BET plot
all points
chosen points
model fit
monolayer point
$\frac{p/p°}{n(1-p/p°)}$
p/p°

b)

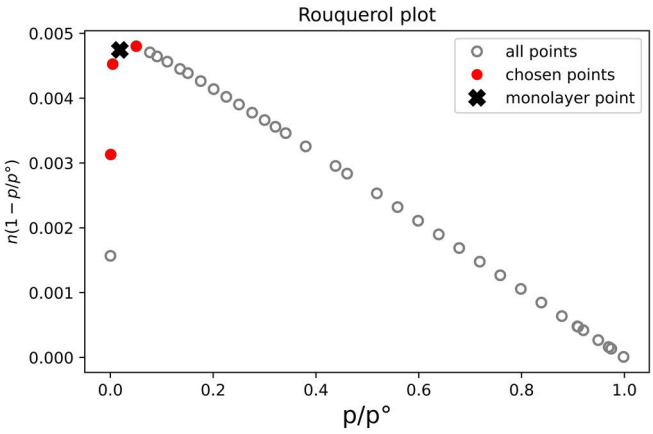
Rouquerol plot
all points
chosen points
monolayer point
$n(1-p/p°)$
p/p°

c)

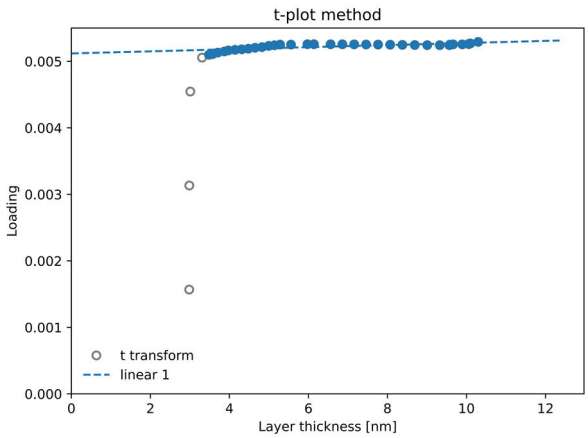
t-plot method
t transform
linear 1
Loading
Layer thickness [nm]

N14

a)

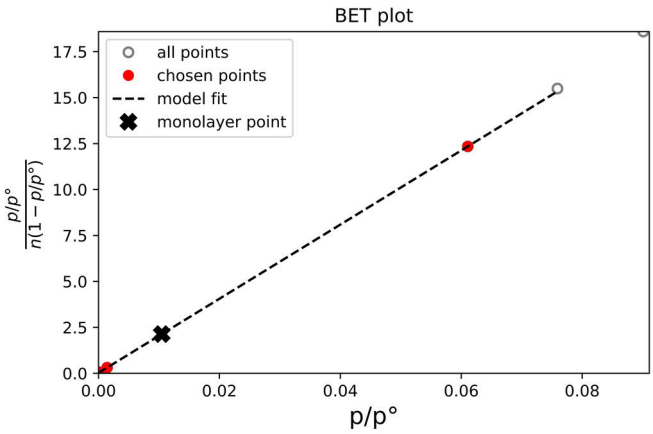
BET plot
all points
chosen points
model fit
monolayer point
$\frac{p/p°}{n(1-p/p°)}$
p/p°

b)

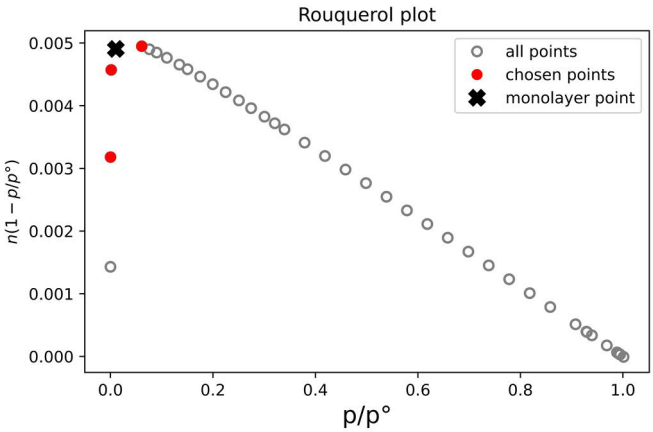
Rouquerol plot
all points
chosen points
monolayer point
$n(1-p/p°)$
p/p°

c)

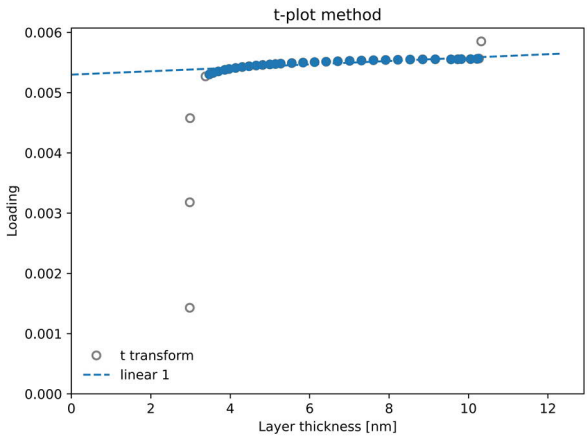
t-plot method
Loading
t transform
linear 1
Layer thickness [nm]

N15

a)

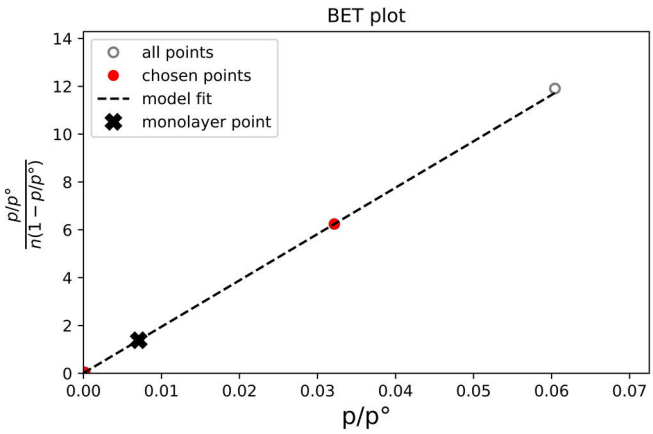
BET plot
all points
chosen points
model fit
monolayer point
$\frac{p/p°}{n(1-p/p°)}$
p/p°

b)

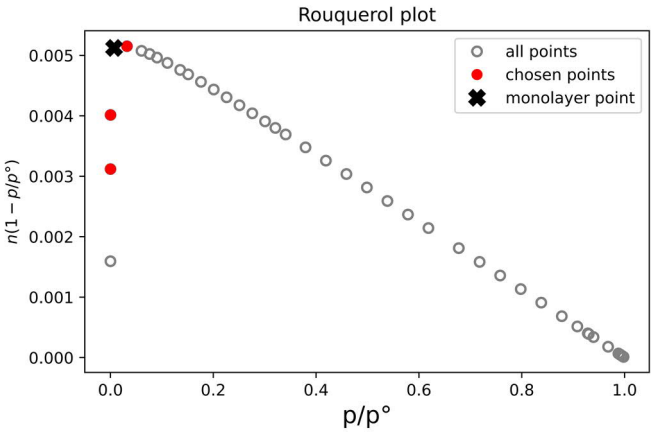
Rouquerol plot
all points
chosen points
monolayer point
$n(1-p/p°)$
p/p°

c)

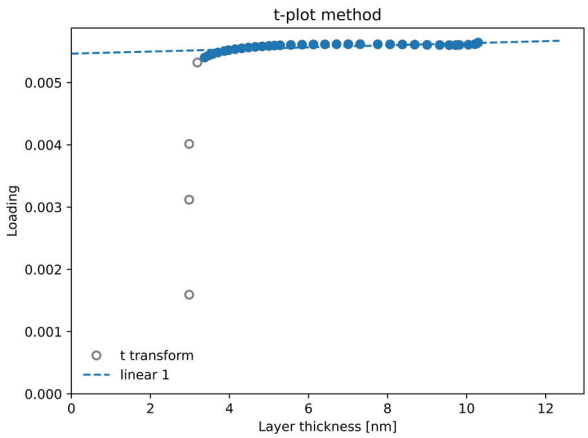
t-plot method
t transform
linear 1
Loading
Layer thickness [nm]

N16

a)

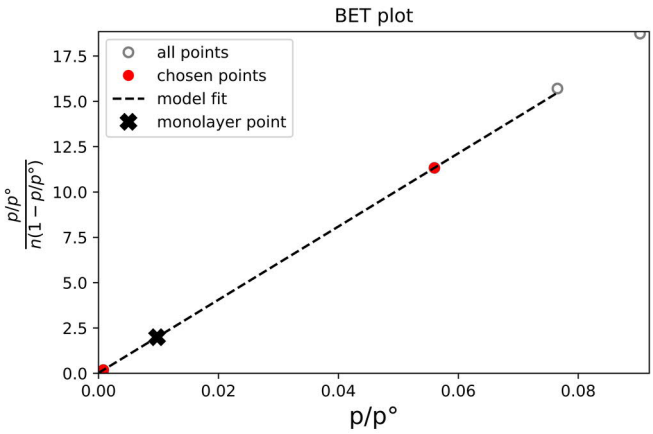
BET plot
all points
chosen points
model fit
monolayer point
$\frac{p/p°}{n(1-p/p°)}$
p/p°

b)

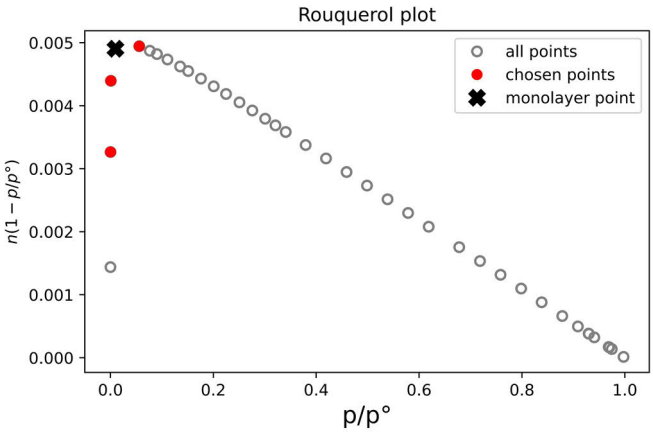
Rouquerol plot
all points
chosen points
monolayer point
$n(1-p/p°)$
p/p°

c)

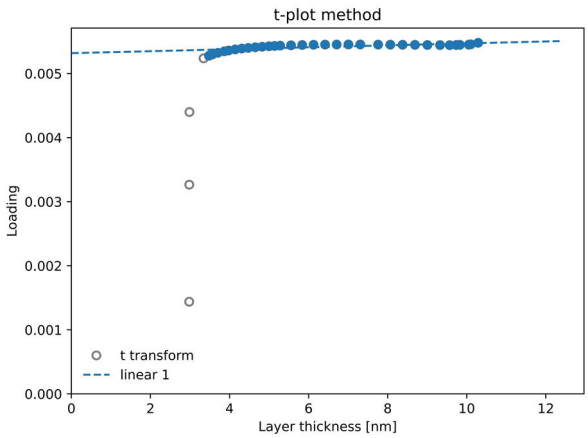
t-plot method
t transform
linear 1
Loading
Layer thickness [nm]

a)

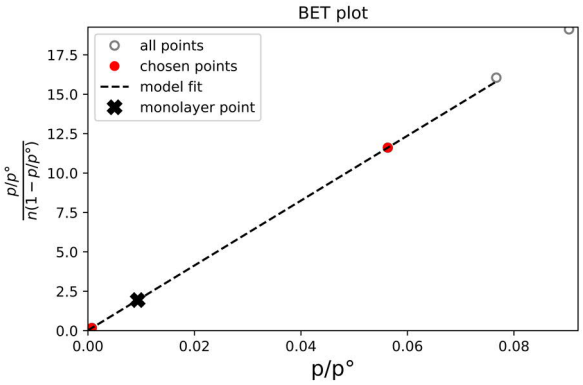

b)

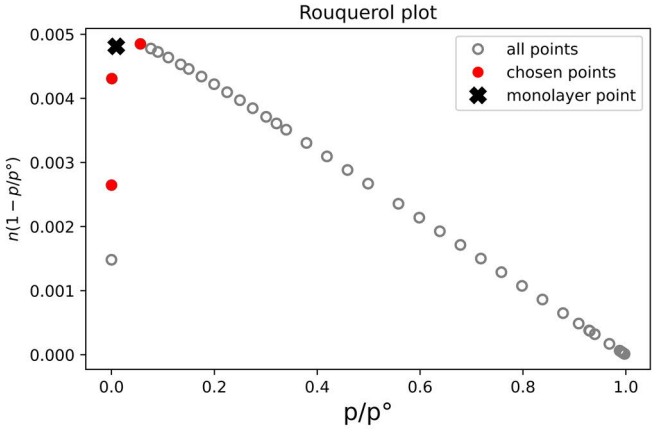

c)

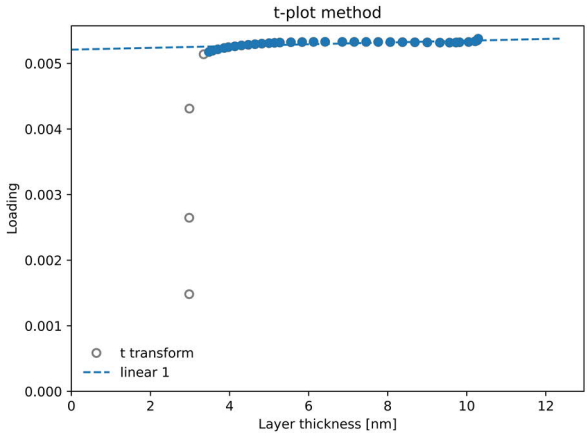

Appendix C a) BET, b) Rouquerol, and Dubinin-Radushkevich plots obtained from the processing of the N_2 isotherms in pyGAPS.

D. Carbon dioxide adsorption and desorption

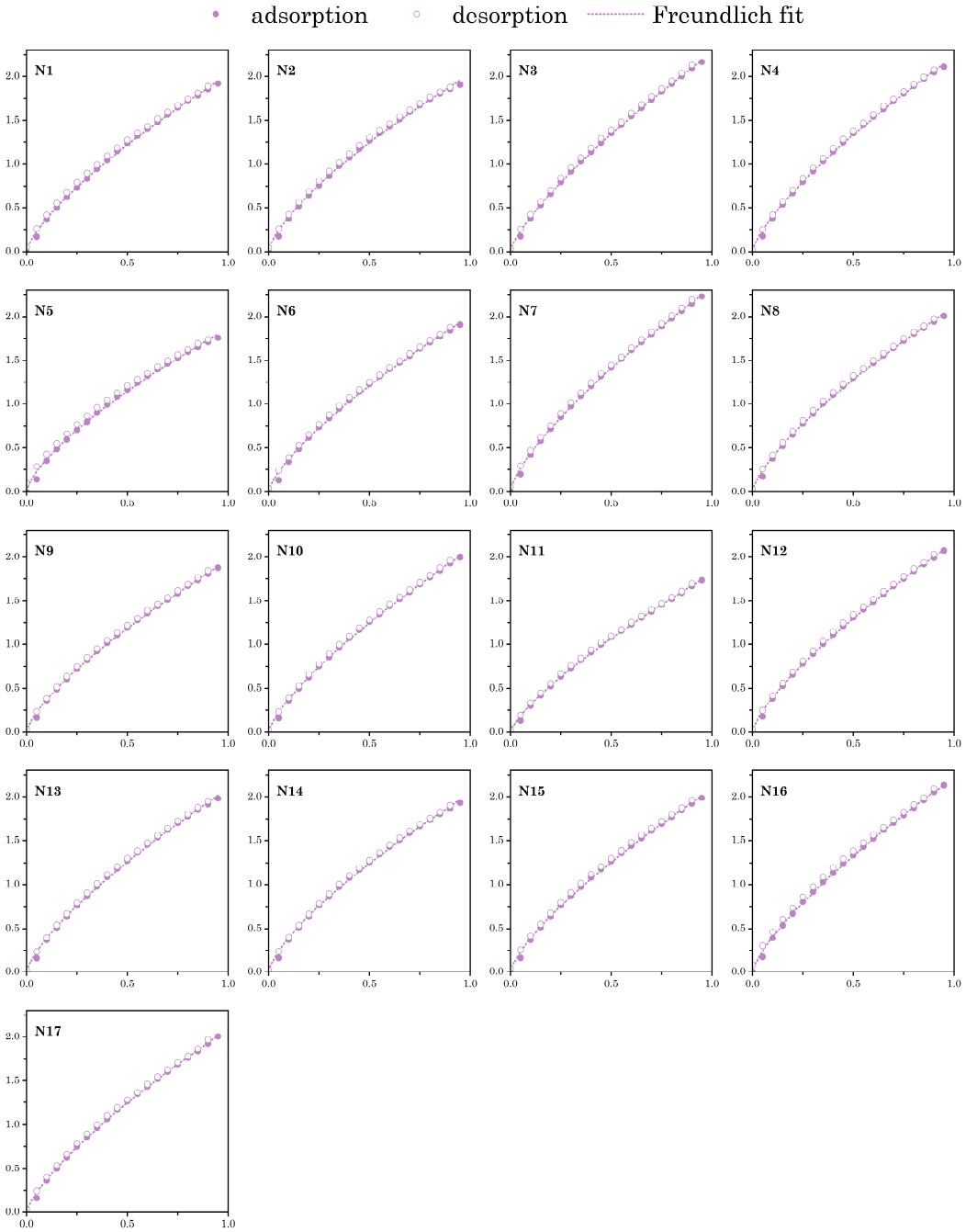

Appendix D Thermogravimetric CO_2 adsorption and desorption isotherms (40°C) of the samples composing the Face-centered Central Composite Design. The abscissa in each plot represents the relative pressure (p/p_0) and the ordinate the CO_2 load in mmol/g. The dotted line depicts a fitting of the adsorption data using Freundlich's empirical equation for gas adsorption.

E. XPS spectra and their deconvolutions

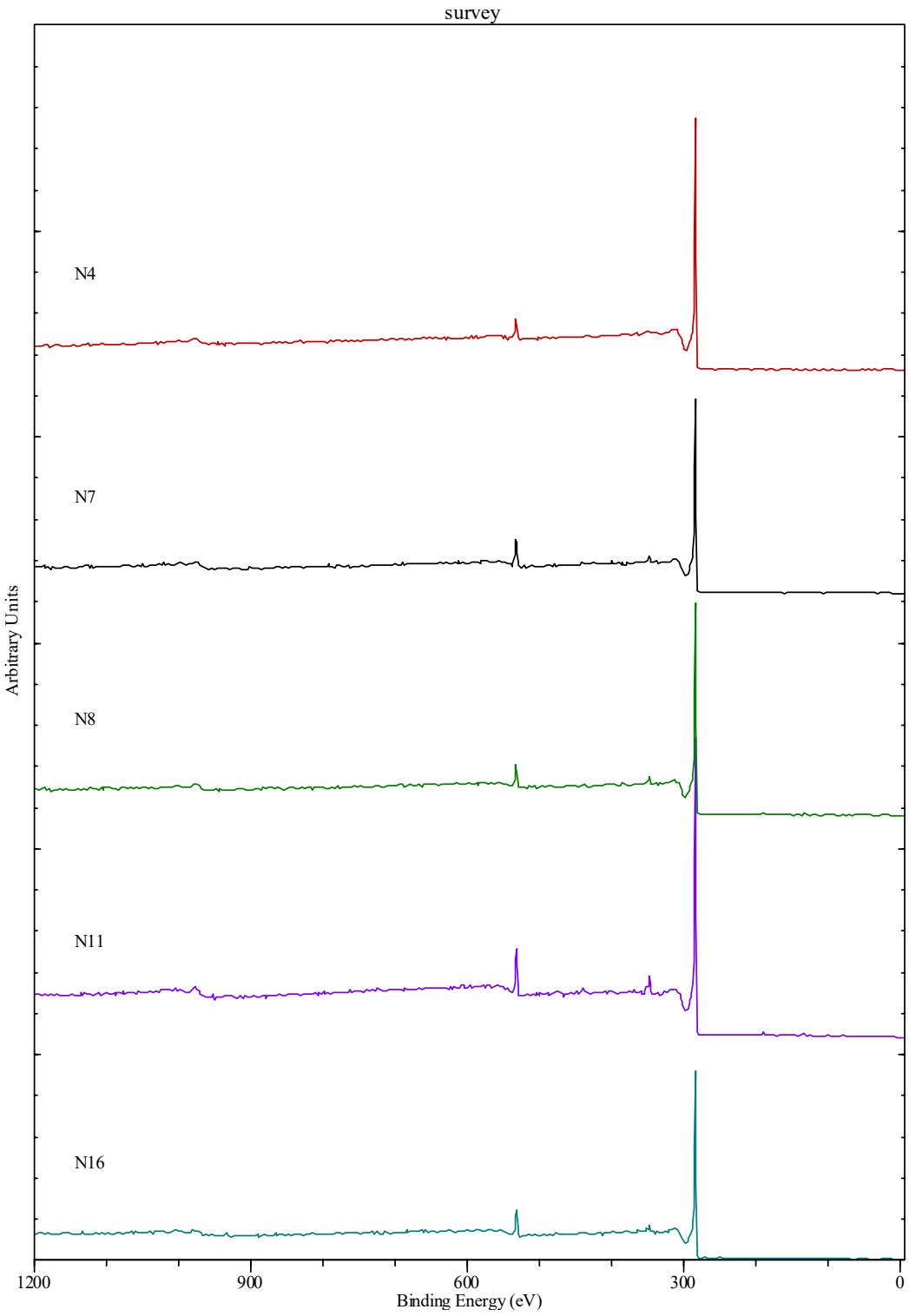

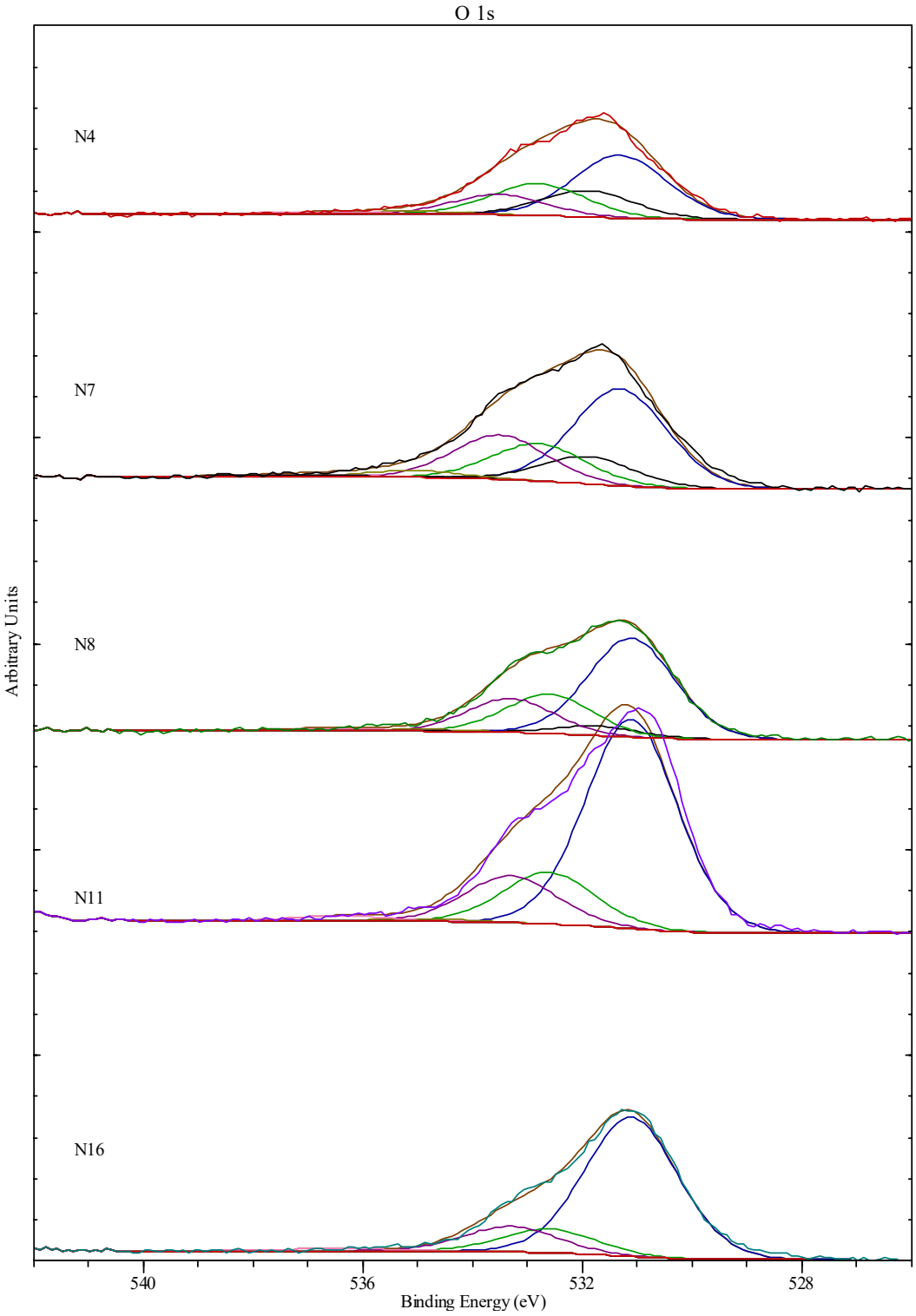
O 1s
N4
N7
N8
N11
N16
Arbitrary Units
540
536
532
528
Binding Energy (eV)

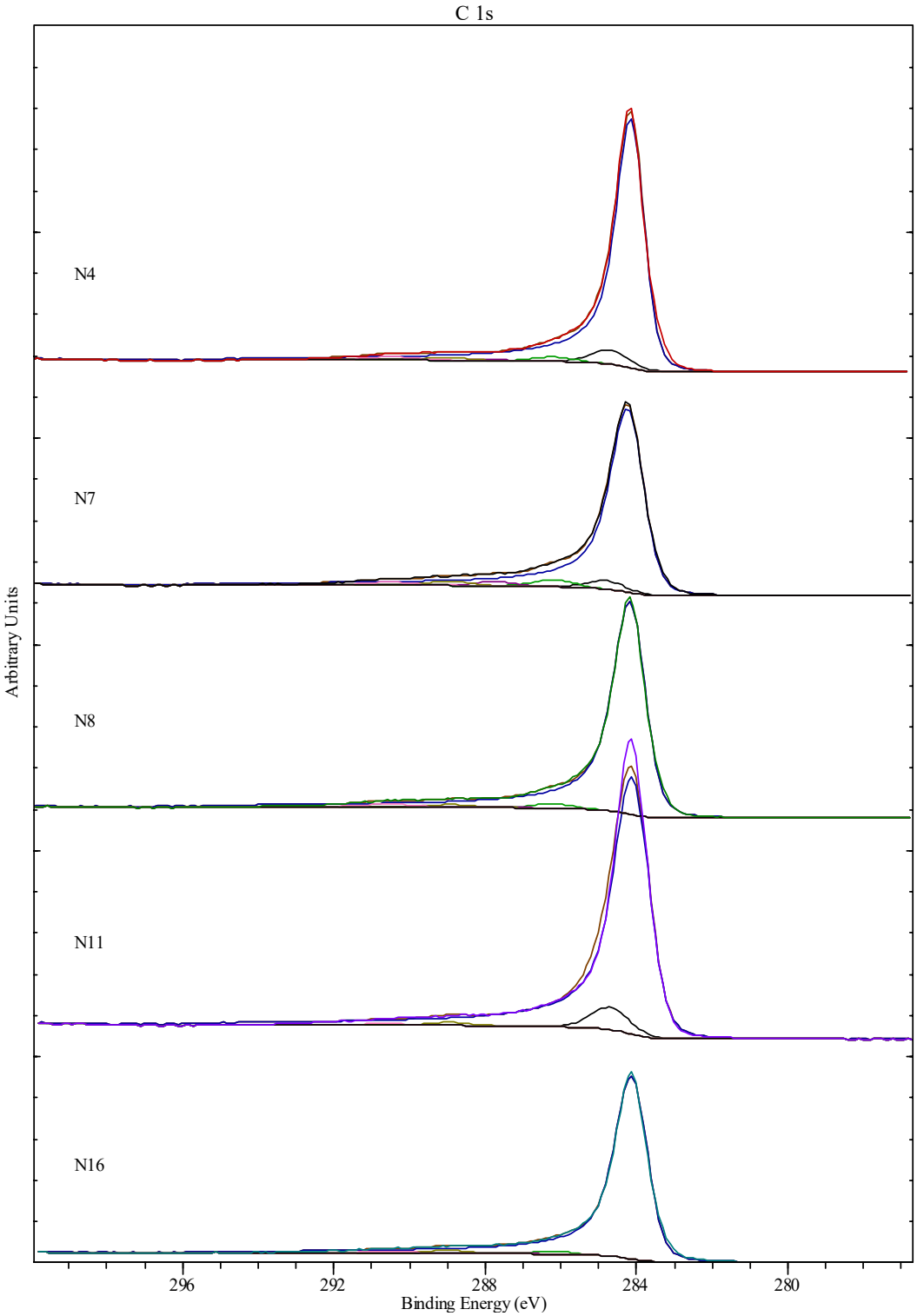
C 1s
N4
N7
N8
N11
N16
Arbitrary Units
296
292
288
284
280
Binding Energy (eV)

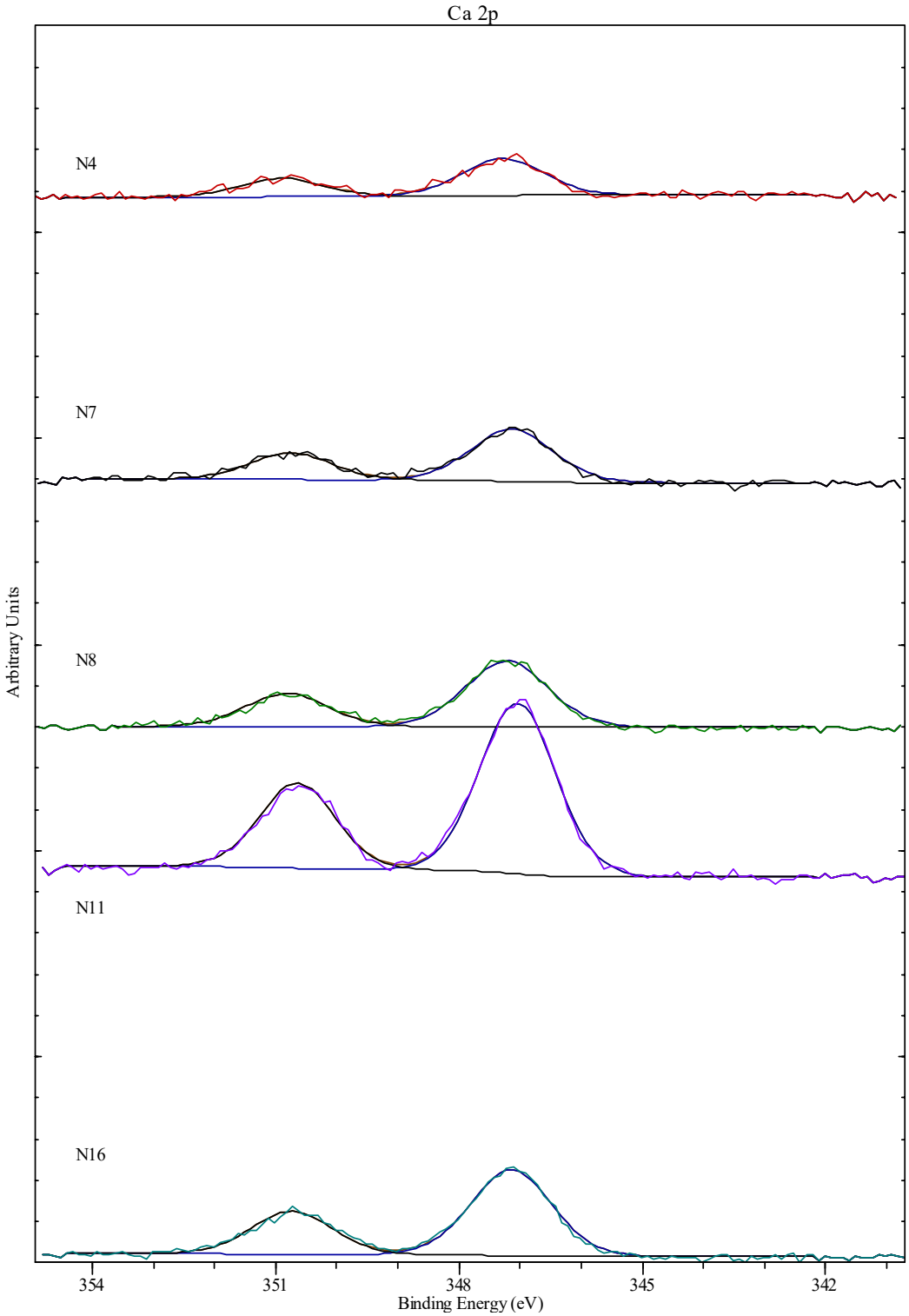
Ca 2p
N4
N7
N8
N11
N16
Arbitrary Units
354
351
348
345
342
Binding Energy (eV)

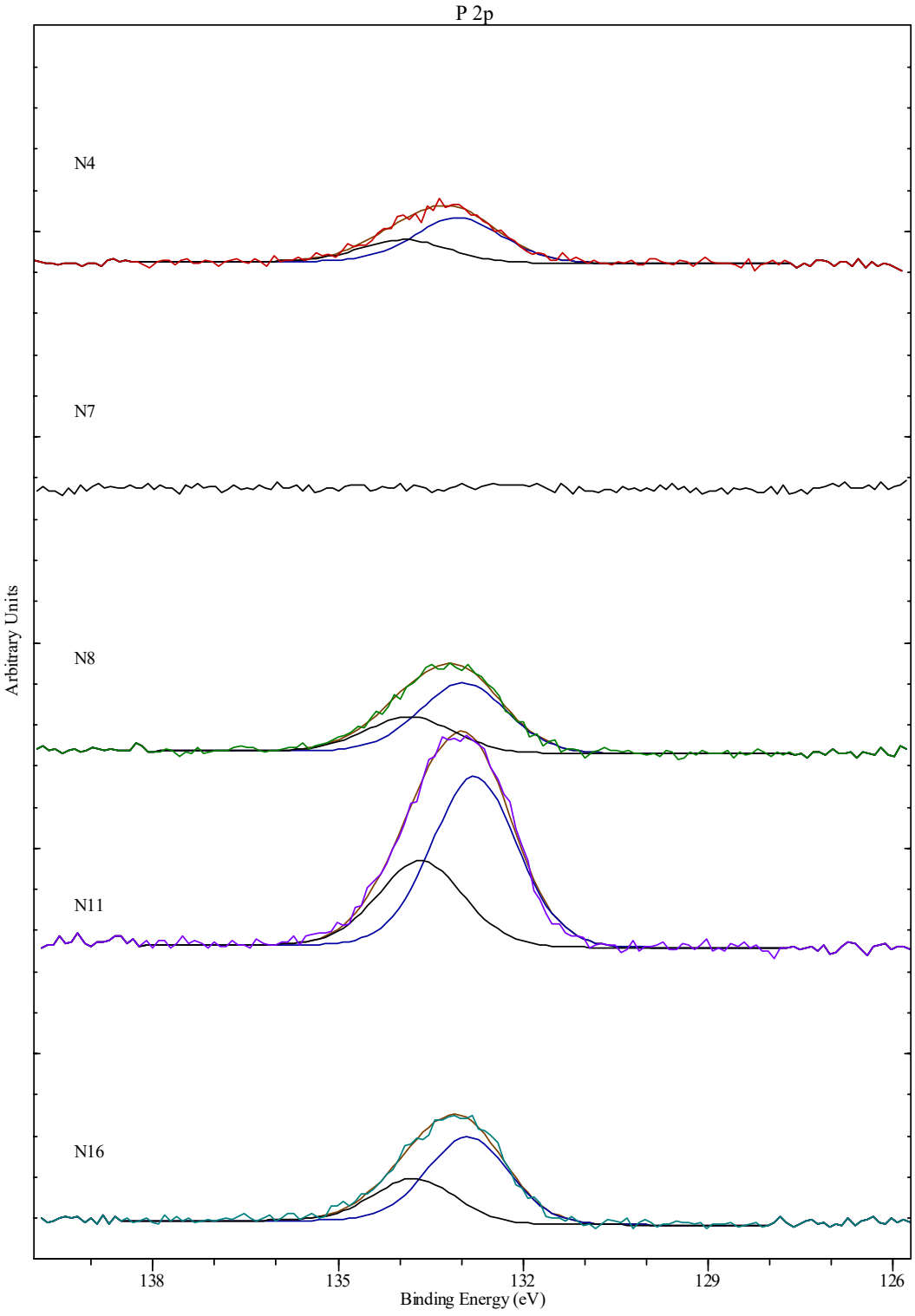

Appendix E XPS spectra and their signals deconvolutions.